Investigation on Electrodeposited Bismuth and Bismuth Antimony Thin Films and Nanowires

Dissertation

zur Erlangung des Doktorgrades
des Department Physik
der Universität Hamburg

vorgelegt von

Dipl.-Phys. Sonja Heiderich
aus Heinsberg

Hamburg
2013

Gutachter der Dissertation	Prof. Dr. K. Nielsch Prof. Dr. A. Fontcuberta i Morral
Gutachter der Disputation	Prof. Dr. K. Nielsch Prof. Dr. U. Merkt
Datum der Disputation	31. Mai 2013
Vorsitzende/r des Prüfungsausschusses	(Prof. Dr. H.P. Oepen)
Vorsitzende/r des Promotionsausschusses	(Prof. Dr. P. Hauschildt)
Dekan(in) der Fakultät für Mathematik, Informatik und Naturwissenschaften	(Prof. Dr. H. Graener)

Abstract

A comprehensive study on electrodeposited nanostructures is presented in this work. Beside the structural and thermoelectrical characterization of bismuth (Bi) and bismuth antimony (BiSb) thin films, the focus of this work is the characterization of single bismuth and bismuth antimony nanowires. The wires have been deposited using alumina oxide membranes as templates. Resolving of the membranes afterwards allows for the investigation of single nanowires. Transmission electron microscopy analysis of single wires demonstrate that the pulsed electrodeposited nanowires are crystalline. Furthermore, the development of suitable processes for contacting single nanowires exhibit the possibility of numerous transport measurements. The temperature dependent resistance and magnetoresistance of pure bismuth and bismuth antimony nanowires is measured. Additionally the Seebeck coefficient of single wires is determined and the influence of an annealing process on the transport properties is investigated. It turns out that the transport properties of annealed BiSb wires become predictable after an annealing process. For single wires with an antimony content of 8 at % thermoelectric power factors of 200 – 400 $\mu WK^{-2}m^{-1}$ are reached.

Kurzdarstellung

In dieser Arbeiten werden umfangreiche Untersuchungen an elektrochemisch abgeschiedenen Nanostrukturen vorgestellt. Neben der strukturellen und thermoelektrischen Charakterisierung von Bismut- und Bismut-Antimon-Dünnfilmen liegt der Fokus der Arbeit auf der Charakterisierung von in Aluminiumoxid Membranen als Templat elektrochemisch abgeschiedenen Nanodrähten. Strukturelle Untersuchung am Transmissionelektronenmikroskop verifizieren, dass die Elektrodeposition ein geeignetes Mittel ist um kristalline Nanodrähte herzustellen. Des Weiteren konnten durch die Entwicklung von Kontaktierungsprozessen umfangreiche elektrische Messungen an Einzelstäben vorgenommen werden. Die temperaturabhängigen Transporteigenschaften von Bismut und Bismut-Antimon Einzeldrähten, mit und ohne Magnetfeld wurden untersucht und der Seebeck -Koeffizient von Einzelstäben wurde bestimmt. Darüber hinaus ist der Einfluss eines Temper-Schrittes auf die elektrischen Eigenschaften der Nanodrähte untersucht worden. Es hat sich gezeigt, dass dieser Schritt die Eigenschaften von Einzeldrähten stabilisiert. Es konnten für die Bismut-Antimon Nanostäbe mit einem Antimongehalt von 8 at % thermoelektrische Powerfaktoren von 200 – 400 $\mu WK^{-2}m^{-1}$ bei Raumtemperatur erreicht werden.

“ Il semble que la perfection soit atteinte
non quand il n’y a plus rien à ajouter,
mais quand il n’y a plus rien à retrancher. ”

Antoine de Saint-Exupéry, ’Terre des Hommes’

Contents

List of Figures

List of Tables

Acronyms and Symbols

Here an over sight on the used acronyms, natural constants and symbols is given.

Acronyms

AAO anodic aluminum oxide. 31, 40, 68
AC alternating current. 57
ALD atomic layer deposition. 4, 38, 40

CCD charge-coupled device. 20
CV cyclic voltammogram. 8, 13, 79

DMSO dimethyl sulfoxide. 12

EDX energy dispersive X-ray spectroscopy. 18, 21, 41, 47, 71, 79, 80
ETO electrical transport option. 55, 71

FIB focused ion beam. 50
FWHM full width half maximum. 25

HR-TEM high resolution transmission electron microscopy. 45

ICP-OES inductively coupled plasma-optical emission spectrometry. 18, 19

LLL lowest LANDAU level (ground state). 75
LMR longitudinal magnetoresistance. 56

MBE molecular beam epitaxy. 4, 65
MOCVD metal organic vapor deposition. 4
MR magnetoresistance. 55, 62, 71, 72, 74, 80

NW nanowire. 77

OCP open circuit potential. 9
OMR ordinary magnetoresistance. 55

PSM potential SEEBECK microprobe. 20

RIE reactive ion etching. 51
RT room temperature. 23
RTG radioisotope generator. 2

SAED selective area diffraction pattern. 44
SEM scanning electron microscopy. 18, 40, 75, 76

TCR temperature coefficient of resistance. 60, 61, 69
TE thermoelectric. 5, 6
TEG thermoelectric generator. 2
TEM transmission electron microscopy. 31, 42, 43, 71, 79
TMR transverse magnetoresistance. 56, 62

XRD X-ray diffraction. 18, 19, 79

Symbols

e electron charge ($1.6021765 \cdot 10^{-19}$ C). 74, 77
F Faraday constant (96485.3365 Cmol). 8
$\hbar$ Planck ´s constant ($1.054571 \cdot 10^{-34}$ Js = $6.582119 \cdot 10^{-16}$ eVs).75, 77
K Scherrer factor (0.62-2.08). 19
k_B Boltzmann constant ($1.38065(4) \cdot 10^{-23}$ J/K = $8.6173324 \cdot 10^{-5}$eVK^{-1}). 70, 77
L Lorenz number (2.1-2.9 V^{2}K^{-2}).3
m_e electron mass ($9.109382 \cdot 10^{-31}$ kg).5, 77
R universal gas constant (8.314461 Jmol^{-1}K^{-1}).8
A galvanomagnetic coefficient. 63, 72, 80
a_i chemical activity. 8

B magnetic field. 74

c_i chemical concentration. 8

D grain size. 19
d diameter. 58, 74
d_{hkl} lattice plane distance. 19
D_{int} inter-pore distance. 36

ΔE thermal band gap. 66, 69, 70
E_g band gap. 70, 71
E^0 standard electrode potential. 8
η efficiency. 3
η_{Carnot} Carnot efficiency. 3

I	electrical current. 2
κ	thermal conductivity. 3
λ	wave length. 19
L_H	magnetic length. 74
m^*	effective mass. 5, 56, 62, 74, 77
μ	mobility. 60, 65
n	carrier concentration. 60, 64, 77
ω_c	cyclotron frequency. 56
Π	PELTIER coefficient. 2
pf	power factor. 3, 66, 76
Q	heat quantity. 2
R	resistance. 56, 57, 76
r_c	cyclotron radius. 74
ρ	resistivity. 49, 58, 68, 69
S	SEEBECK coefficient. 1, 27, 29, 49, 57, 65, 76, 79
σ	electrical conductivity. 3, 49
t	time. 2
τ	life time. 56, 62, 72
ΔT	temperature difference. 1, 58, 75
U	potential. 20, 36
U_{thermo}	thermovoltage. 57, 75
v_F	fermi velocity. 74
ZT	thermoelectric figure of merit. 3

1 Motivation

1.1 Why Thermoelectrics?

During the last two decades, regenerative energy sources like wind, water and solar energy has gotten in the focus of interest in science and economy due to the urgent need for alternatives to conventional fossil energy sources. Also the research on thermoelectric has experienced an increase of interest, as a possibility to make processes more efficient or to conserve energy, to recycle energy or for energy harvesting. Since in conventional combustion process more than ⅔ of the energy is lost as waste heat, thermoelectric generators are supposed to return the heat into useable electrical energy.

The two important thermoelectric effects are known as the Seebeck effect and its reversal, the Peltier effect. Both have been discovered independently by Thomas Johann Seebeck and Jean Peltier respectively at the beginning of the 19th century. Seebeck found out that a potential arises in a material that is part of a closed conductor loop if the contacts have different temperatures T_1 and T_2 (compare fig. 1.1 (a)). This phenomenon has been verified via a compass needle that detected the magentic field caused by the current flux. Due to their higher kinetic energy the carriers from the hot side drift to the cold side. Thus, a carrier overplus is generated at the cold side which causes the potential difference or Seebeck potential between the contacts. The so-called Seebeck coefficient $S\,[\mu VK^{-1}]$ describes the magnitude of the resulting potential depending on the temperature difference:

$$S = \frac{\Delta U}{\Delta T}. \tag{1.1}$$

The magnitude of the Seebeck potential does not only depend on the temperature difference ΔT between the contacts but also on the properties of the different materials in the system. The Seebeck coefficient can reach values between a few μVK^{-1} and several hundred μVK^{-1}. Its sign can be either positive or negative dependent on the main charge carriers in the materials, holes or electrons.

The reverse effect is the Peltier effect. A heating and cooling of the contacts between two

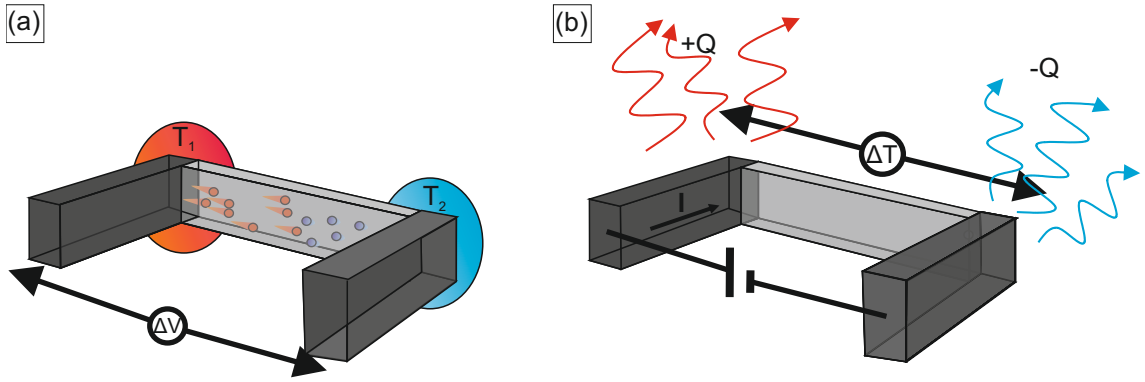

Figure 1.1: (a) SEEBECK effect; two different materials with different temperatures T_1 and T_2 at the contacts. Due to higher mobility more carriers drift from the hot side to the cold side than the other way round, causing a potential difference ΔV between the contacts. (b) PELTIER effect; an electrical current I along a conductor of two different materials cause a heating, respectively cooling of the two contacts between the different material. The heat quantities $\pm Q$ are emitted, respectively absorbed.

different materials can be observed while a current flow is driven through the conductor:

$$\Pi = \frac{\Delta Q}{I \cdot t}. \tag{1.2}$$

The magnitude of the PELTIER effect Π can be described by the heat quantity $\pm Q$ that is emitted or absorbed at the contacts depending on the electrical current I and the time t (compare fig. 1.1 (b)).

Thermoelectric generators (TEGs) are well known and used in different aerospace missions since the 1950ies. They have been developed as an energy source in space where photovoltaic cells become inefficient. Radioisotope generators (RTGs) have been used for example for the Apollo mission or the Voyager missions. The high temperature difference (several 100 K) between the hot side of the module and the cold side, the space, is used to generate power. As heat source fissile material is used. Thus it is independent from the solar energy. Until today both Voyager space probes send their signals back to earth, demonstrating the stability of these systems. One very new and popular example for the usage of RTGs in space travel is the Mars rover Curiosity.

On earth the use of thermoelectric generators for energy harvesting is an upcoming field of interest. Only small temperature differences of 0.5 – 10 K are supposed to give enough power for transmitters to send control data to a basis station. Until today a bottle neck of thermoelectric generators and the reason why they have not been used for the down-market is the low efficiency and high preparation cost compared to other methods. The performance

of a thermoelectric material is directly linked to the dimensionless thermoelectric figure of merit ZT which is composed of the SEEBECK coefficient S, the electrical conductivity σ and the thermal conductivity κ:

$$ZT = \frac{S^2\sigma}{\kappa}T. \tag{1.3}$$

Whereas the product $S^2 \cdot \sigma$ is referred to as power factor pf. For having a good thermoelectric material a high SEEBECK coefficient together with a high electrical conductivity but a low thermal conductivity is required [Row94]. This is a challenge for material engineering because no natural element combines all these properties. The highest values of the SEEBECK coefficients and the lowest thermal conductivities are found in insulators which on the other hand have a very low electrical conductivity. However, metals show the opposite behavior. Thus, the most promising candidates can be found in the semiconducting and semimetallic region. Another difficulty is that the maximum efficiency η is determined by the CARNOT efficiency $\eta_{Carnot} = 1 - \frac{T_c}{T_h}$ with T_c being the cold side and T_h being the hot side:

$$\eta = \frac{\sqrt{1+ZT}-1}{\sqrt{1+ZT}+\frac{T_c}{T_h}} \cdot \eta_{Carnot}. \tag{1.4}$$

The value of $\eta = \eta_{Carnot}$ can only be reached for the limit of $ZT = \infty$. Today good thermoelectric materials reach a $ZT = 1$, which correspond with a ratio of $\frac{T_c}{T_h} = 0.5$ and efficiency of 10 %. Increasing the figure of merit to $ZT = 3$ would increase the efficiency up to 20 % which might cause tenfold application [NBKB11].

1.2 Why Nanostructuring?

Theoretical calculations from the 1990ies by Mildred DRESSELHAUS have predicted a significant increase of ZT by nanostructuring [SYMC+ 2]. One has to tune the quantity of $S^2 \cdot \sigma$ - the numerator of the figure of merit and to minimize the thermal conductivity -the denominator. The chances of success depend on the material and on suitable nanostructuring.
In common metals the thermal conductivity is coupled with the electrical conductivity via the WIEDEMANN-FRANZ law $LT = \frac{\kappa}{\sigma}$, with L being the LORENZ number. This ratio is always constant, thus the figure of merit of metallic elements can not be improved by reducing the thermal conductivity. Due to the very low electrical conductivity insulators are also no promising candidates for thermoelectric applications. In semiconductors the thermal conductivity has contributions from electrons κ_{electron} and phonons κ_{phonon}. In general both parts

are coupled but by skillful nanostructuring this coupling can be abrogated. The part of the thermal conductivity that is caused by phonons (lattice vibration) can be suppressed without effecting the current transport by electrons due to the different wave numbers of electrons and phonons.
The successful enhancement of the figure of merit by nanostructuring has been shown by Venkatasubramania [VSCO01]. He reported an extraordinary room temperature value of $ZT \sim 2.4$ for a sample of p-type Bi_2Te_3/Sb_2Te_3 superlattices. Since these values could never be reproduced this publication is highly controversial. However, also Harman *et al.* [HTWL02] obtained a $ZT > 1.5$ for quantum dot superlattices.
Nanostructured material poses new challenges concerning sample preparation and measuring technique. A manifold of structures can be achieved by high vacuum processes like molecular beam epitaxy (MBE) [RHL+12, iMCA+08, CDVK+98], metal organic vapor deposition (MOCVD) [WKBL99, GBA+99] or atomic layer deposition (ALD) [ZGB+13, SHFM02]. The growth of thin films, superlattices and nanowires has been realized by these techniques.
However, the electrodeposition of nanostructures presents a low cost alternative to these methods [LW11]. The advantage of the electrodeposition compared to other techniques is that in principle the process can run at room temperature and under atmospheric pressure. Thus no high-cost equipment is needed. By optimization of the process parameters and the used electrolytes sample qualities are achieved which can compete with samples grown by a high-vacuum process.

1.3 Why Bismuth and Bismuth Antimony?

Bismuth and bismuth antimony compounds provide unique properties and are promising candidates for thermoelectric applications; a short introduction to these far out materials is given in the next section.

The element bismuth with the atomic number 83 belongs to the 5th main group of the table of contents. It crystalizes in a rhombohedrical structure and has a highly anisotropic Fermi surface with three electron pockets in a plane normal to the trigonal axis and with an angle to the bisectrix axis of 6°. The electron pockets have an angle of 120° with the other two and they are symmetric to the L-point of the Brillouin zone. The electron hole is along the trigonal axis at the T-point of the valence band. A scheme of the Fermi surface can be found in [VSS+00]. At room temperature the bandstructure of bulk bismuth displays a small energy overlap between the L-point of the conductance band and the T-point of the valence band. Due to this small indirect band overlap, as a bulk material bismuth is a semimetal with

an equal number of electron and holes and its properties strongly determined by its dimension [LCY+00]. The band gap vanishes by lowering the dimension of bismuth structures and a transition from semimetalilc to semiconductive behavior occurs as it is illustrated in fig. 1.2 (b).

Furthermore, bismuth has the lowest effective mass m^* of all metals ($m^* = 0.001 m_e$) and an

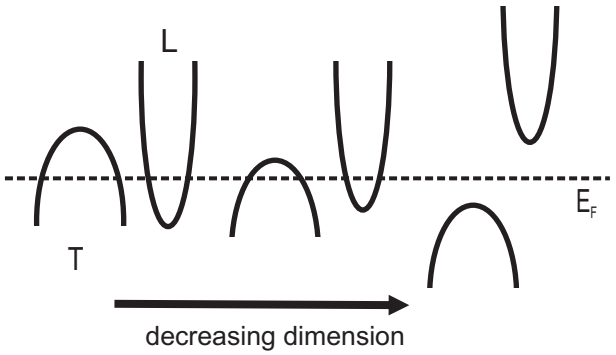

Figure 1.2: Schematic change of the band gap of bismuth nanowires with decreasing diameter.

extremely long mean free path that can reach up to several hundred µm at low temperatures. Altogether bismuth is extremely attractive for electronic and thermoelectric devices as well as fundamental research because of the tunable electronic properties.

The semimetal to semiconductor transition is well known for bismuth and has already been observed for thin films [HMB+93] as well as for bismuth nanowires [LRC+02a]. BiSb alloys show this transition already as bulk material, depending on the antimony concentration. The band structure of $Bi_{1-x}Sb_x$, at 77 K, depending on the antimony content x is given in ref. [LCM+96]. Alloys of $Bi_{1-x}Sb_x$ with $0.07 < x < 0.22$ are semiconductive with a transition from indirect to direct semiconductor in this range [KOSH78, KNK+04].

A size and antimony content dependent phase diagram is given in ref. [RLD01]. Pure bismuth nanowires change their behavior from semimetallic to indirect semiconductive at a diameter of about 50 nm. Also the admixture of antimony causes transitions between semimetallic and direct or indirect semiconductive behavior depending on the chemical composition and the diameter of the wires [LRC+02a].

Theoretical calculation for bismuth nanowires have predicted $ZT > 1$ for wires with diameters below 20 nm [SYMC+ 2, LSD00]. However, BiSb nanowire show good thermoelectric (TE) performances already at diameter of ~ 40 nm [RLD01].

And even at higher dimension like bulk material or thin films $Bi_{1-x}Sb_x$ have shown for long

time their potential for TE applications. Ibrahim and Thompson reviewed that BiSb alloys with Sb < 20 at % are thermoelectric materials due to their remarkable performances already as bulk materials and thin films [IT85]. Also Smith and Wolfe denominate BiSb alloys as promising candidates for TE applications. They found for $Bi_{1-x}Sb_x$ with $0.05 < x < 0.16$ values of the figure of merit between $4 - 6 \cdot 10^{-3}\,K^{-1}$ from 50 – 100 K [SW62].

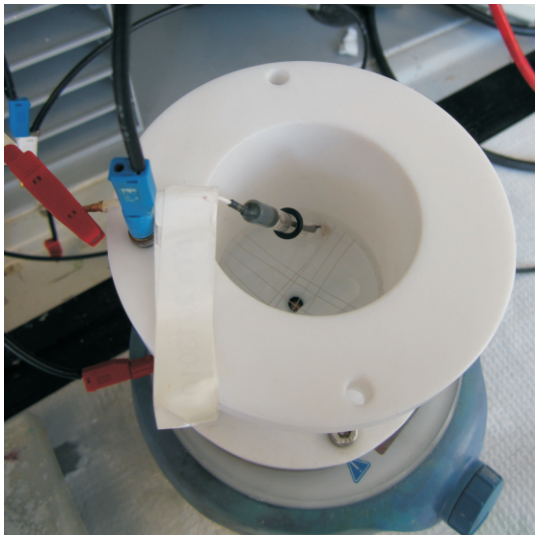

2 Electrodeposition of Nanostructures

The electrodeposition of semiconducting or metallic materials is a rather inexpensive and simple method to deposit material onto a conductive surface of choice. No high vacuum chambers are required and it can be used for commercial applications like plating or coating of mechanical components. In addition it is used in research programs for the fabrication of nanostructures [PBBMD08, PM06].
The basis for the electrodeposition is an electrolyte bath containing the materials in form of ions which are supposed to be deposited. By varying the metallic ion concentration of the electrolyte and the deposition conditions different composites of the deposit are possible. During this work electrodeposited bismuth and bismuth antimony thin films and nanowires have been investigated.

2.1 Principles of Electrodeposition

At this juncture only a brief introduction into the used electrochemical preparation and analysis methods shall be given. The field of electrochemistry is widely described and explained in relevant literature [CHH03, Zos07]. The principles of electrodeposition are based on an electrochemical cell, as it is sketched in figure 2.1 (a). By applying a potential between two electrodes in an electrolyte bath with cations (C^+) and anions (A^-). The positive ions are forced to the cathode and the negative ions are forced to the anode. If the applied potential is higher than the reduction potential of the cations, they are reduced, thus deposited at the cathode.
Since the potential can only be measured between two electrodes one defines a standard electrode potential E^0 all other potentials are measured against. The potential of a half-cell then is given by the Nernst equation:

$$E = E^0 + \frac{RT}{z_e F} \cdot \ln\left(\frac{a_{\mathrm{Ox}}}{a_{\mathrm{Red}}}\right) \tag{2.1}$$

Here R is the universal gas constant, T is the absolute temperature in Kelvin, z_e is the charge of the ions, F being the Faraday constant, a_i the activities of the oxidation and reduction phase respectively. This equation simplifies at room temperature and by the conversion of the natural logarithm to the expression:

$$E \approx E^0 + \frac{0.059}{z_e} \cdot \log\left(\frac{c_{\mathrm{Ox}}}{c_{\mathrm{Red}}}\right) \tag{2.2}$$

where the concentrations c_i can be used to calculate the potential of a half-cell.
An alternative to determine the reduction and oxidation potentials of different electrolytes is cyclic voltammetry as it is described in the following. During this work a three electrode setup is used. The potential is adjusted against an Ag/AgCl reference electrode (*BASi Analytical Instruments*) in a saturated KCl solution and a platinum mesh as a counter electrode (anode). A cross section of the deposition setup is shown in figure 2.1 (b). The sample which is electrical contacted to a Cu plate is the working electrode, thus the cathode. The deposition beaker with a circular cut-out at the bottom is placed on top of the sample and to prevent leakage an O-ring is placed between the notch and the sample. The platinum mesh is placed above the sample and the reference electrode is arranged aside (compare figure 2.1 (b)). The experiments have been performed with a *VSP Multichannel Potentiostat (Bio Logic Science Instruments)*. The captive software *EC-Lab®* allows to configure various deposition techniques and to create tailor-made deposition routines as well as cyclic voltammetry.
Before starting an electrodeposition process a cyclic voltammogram (CV) of the electrolyte

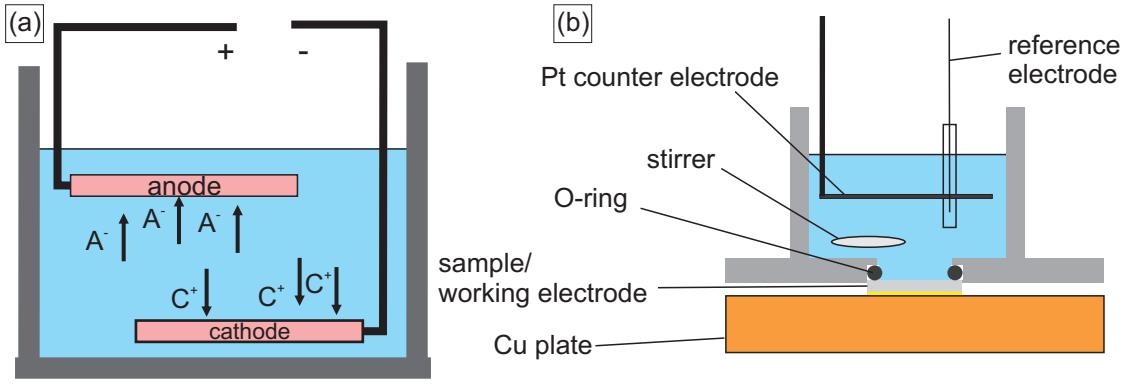

Figure 2.1: (a) Sketch of an electrochemical cell. (b) Three-electrode deposition setup for thin films and nanowires.

is taken to determine the reduction-, oxidation- and open circuit potential (OCP). The current flow in the electrolyte is measured between two electrodes against the Ag/AgCl standard electrode. Simultaneously the potential is swept through a voltage range, typically between ±1 V, and the current depending on the applied potential is recorded. In general different peaks are observable. The reduction potential indicates the voltage where the deposition of material at the cathode starts. At more positive potentials oxidation may dissolve the material deposited before. No current flow is observable in the system at the open circuit potential. Hence the system is stable at this point because neither reduction nor oxidation occurs.

2.1.1 Electrodeposition Conditions

There are different options to drive a deposition: to control the applied voltage or to control the current that flows between the electrodes. These methods are referred to as potentiostatic and galvanostatic respectively.
In case of galvanostatic deposition conditions a distinguished current is set to the system and internal software adjusts the potential at a time to keep the current constant throughout the entire deposition time. Furthermore one has to distinguish between potentiostatic and potentiodynamic methods. Keeping the potential between the electrodes constant is known as potentiostatic deposition (compare fig. 2.2 (a)). During the potentiodynamic method the potential is varied with time. Using alternating steps of different potentials to improve the features of electrodeposited material has been described by Penner *et al.* [Pen02, WMF+02] in the year 2002. During this work a rectangular pulse form, as it is illustrated in fig. 2.2 (b), is applied. The potential during the on-time (t_{on}) is chosen according to the cyclic voltammogramm of the electrolyte such that the deposition of the material takes place (compare

fig. 2.3). The off-time (t_{off}) potential is chosen to be the open circuit potential. Due to the absence of reduction or oxidation the system has time to crystallize during the off-time of the pulse and the electrolyte solution can regenerate close to the surface. The graph (c) of figure 2.2 shows the time-dependent periodically modulated voltage and the corresponding current flow recorded during a pulsed deposition of a bismuth nanostructure. Previous studies of our group have shown that the $\frac{t_{on}}{t_{off}}$ ratio as well as the absolute lengths of the pulses influence the growth rate and the quality of the deposited materials. A ration of 1:5 with absolute values of $t_{on} = 10\,\text{ms}$ and $t_{off} = 50\,\text{ms}$ has been found to show the best results [PLT+12, LSS+08, Sch12].

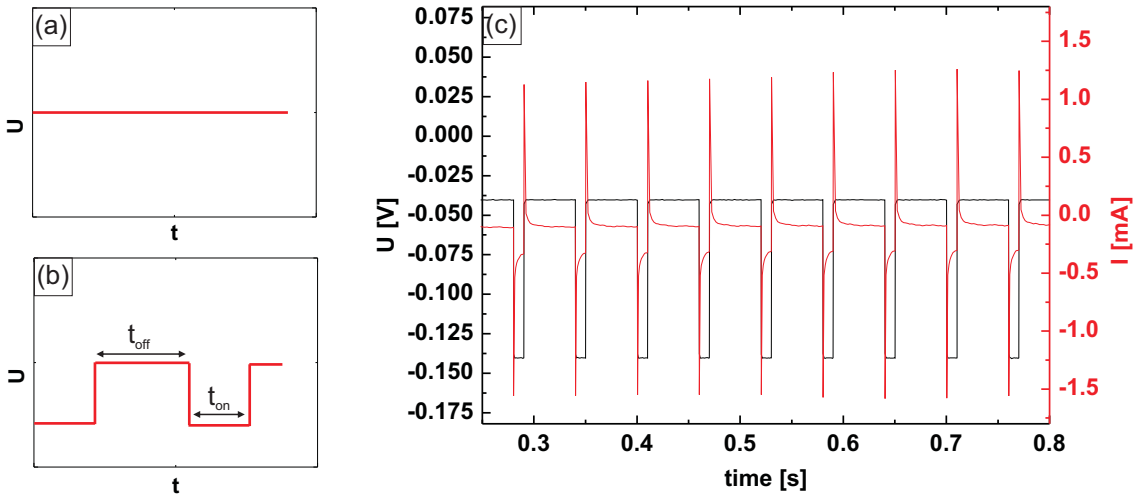

Figure 2.2: (a) Time dependent potential behavior during an unpulsed electrodeposition. (b) Time dependent potential behavior during a pulsed electrodeposition with a rectangular pulse form. (c) Deposition potential and current of a Bi deposition into an anodic alumina membrane with $\frac{t_{on}}{t_{off}} = \frac{10\,\text{ms}}{50\,\text{ms}}$.

2.2 Characterization of Electrolyte Baths

In order to characterize the different solutions used in this work, cyclic voltammetry is performed to determine the characteristic potentials for each metal. An electrolyte containing more than one kind of metallic cations, here bismuth and antimony, shows separated peaks which indicate the different reduction and oxidation potentials for each metal. All analyses take place against a Ag/AgCl reference electrode and are carried out at room temperature with a scan rate of $20\,\text{mVs}^{-1}$.

Pure bismuth as well as bismuth antimony electrolytes are prepared and analyzed. For the

BiSb solutions nitric acid as well as hydrochloric acid is used as solvent. The following part will introduce the electrolytes the depositions are performed with.

2.2.1 Bi Electrolytes

For the electrodeposition of bismuth nanowires (see sec. 4.2), various electrolytes are presented and described in the literature, partly with additives like glycerol, tartaric acid and citric acid. These additives are used as wetting agents that are needed especially by the use of membranes with very small pore diameter (< 30 nm) [Zos07]. The intention here is to

$Bi(NO_3)_3$+5H_2O	**HNO_3**	**additives**	**Ref.**
75 gL^{-1}	to ph 0.9	—	[WZS+01]
75 gL^{-1}	to ph 0.9	65 gL^{-1} potassium hydroxide 125 gL^{-1} glycerol 50 gL^{-1} tartaric acid	[WZJZ+01]
100 gL^{-1}	to ph 2	40 gL^{-1} KNO_3 120 gL^{-1} glycerol 50 gL^{-1} tartaric acid	[JJL+03]
2.43 g	—	6.2 g H_3BO_3 13 mL glycerol 15 g tartaric acid 6 g gelatine 5.84 g NaCl 8.7 K_2SO_4 all for 300 mL DI-water	[TWK+06]
48.5 gL^{-1}	1 M	—	[SWB+07]
19.4 gL^{-1}	0.7M	—	present work

Table 2.1: Overview of Bi electrolytes described in the literature.

work with an electrolyte which components are reduced to the essential to avoid the deposition of foreign atoms. At the beginning, an electrolyte based on the recipe of Wang *et al.* [WZS+01] with 75 gL^{-1} (0.155 M) bismuth(III) nitrate pentahydrate is used. It is found that the nitric acid concentration (> 2 M) needed to dissolve this amount of bismuth ions causes major damages of the membranes if the deposition time exceeds five hours. Therefore the composition of the electrolyte is changed to a lower concentration of bismuth ions following Fukutani and Den [FD08]. A concentration of 0.7 M nitric acid is sufficient to dissolve the bismuth(III) nitrate pentahydrate (for more details compare app. A.1.1) and will not have an impact on the membranes. The cyclic voltammogram in figure 2.3 shows that the reduction of bismuth, thus the deposition of bismuth, starts at a potential more negative

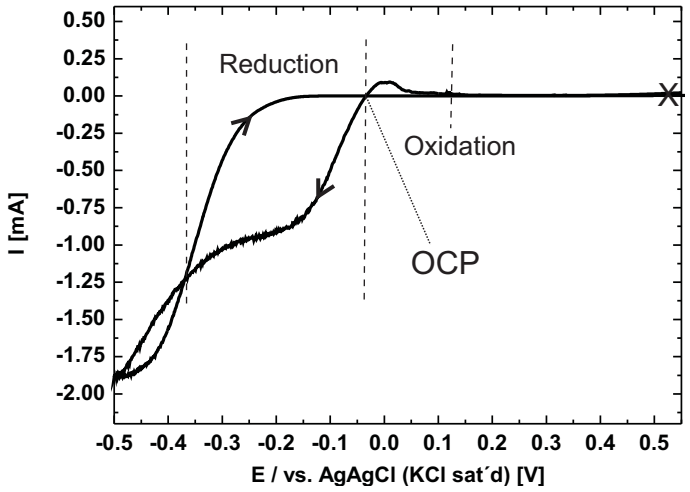

Figure 2.3: Cyclic voltammogram of a bismuth electrolyte containing 0.04 M of $Bi(NO_3)_3$+5 H_2O and 0.7 M of HNO_3.

than −50 mV with a plateau at around −150 mV. At a potential more negative than −350 mV the evolution of hydrogen starts.

2.2.2 BiSb Electrolytes

During the deposition from a solution containing more than one species of metallic cations with different reduction potentials co-deposition of both metals occurs. At the more positive voltage mostly the metal with the lower reduction potential, here bismuth, is deposited. Deposition potentials that are negative enough to reduce both metallic ions cause bismuth and antimony co-deposition. To achieve a nearly pure antimony phase during the deposition, the concentration of Sb(III) salts would have to be higher compared to the concentration of bismuth ions. The solubility of Sb(III) salts is very poor in aqueous solution which is the limiting factor for the concentration of cations in the electrolyte [SRA+12]. To avoid this situation some groups use nonaqueous solutions on dimethyl sulfoxide (DMSO) basis [PMGK+03, MGPK+03]. This has the advantage of higher solubility of Sb(III) salts but on the other hand it requires water free conditions, thus deposition in a glove box and deposition temperatures between 100 – 200 °C. During the preparation of the electrolytes, based on HNO_3 and on HCl the different compounds have to be admixed separately with their solvent to ensure complete dissolution. Especially the pre-dissolving of tartaric acid powder in DI-water before adding the Sb_2O_3 is important, for details compare app. A.1.2.

BiSb Electrolyte on HNO_3 Basis

Two BiSb electrolytes based on nitric acid are presented. For both cases bismuth(III) nitrate pentahydrate and nitric acid as its solvent is used. As source for the Sb^+ ions, antimony oxide with tartaric acid as the corresponding solvent or rather complexing agent is chosen. All investigated electrolytes contain 1 M nitric acid and the amount of antimony(III) salt is kept constant. The bismuth content is slightly varied to check the influence not only of the deposition potential (see sec. 3.5.2) but also of the Bi:Sb ratio on the composition of the deposited material. Table 2.2 gives an overview of the electrolytes described in the literature using $Bi(NO_3)_3{+}5H_2O$ and Sb_2O_3 and nitric acid as solvent. This combination is mainly used for the deposition of BiSbTe compounds but can be modified for BiSb thin films by elide the Te-compound. The compositions of the electrolytes presented here are mainly oriented on the work of Gonzáles *et al.* [MGPG+03].

$Bi(NO_3)_3{+}5H_2O$	Sb_2O_3	HNO_3	$C_4H_6O_6$	additives	Ref.
0.0019 M	0.0056 M	1 M	0.84 M	0.01 M TeO_2	[MGPG+03]
0.0015 M	0.0072 M	1 M	0.65 M	0.0124 M H_2TeO_3	[HWJZ06]
0.0001 M	0.0016 M	1 M	0.033 M	0.0007 M $HTeO_2^+$	[YXB+07]
0.005 M 0.0075 M	0.0056 M	1 M	0.83 M	—	present work

Table 2.2: Overview of BiSb electrolytes on HNO_3 basis described in the literature.

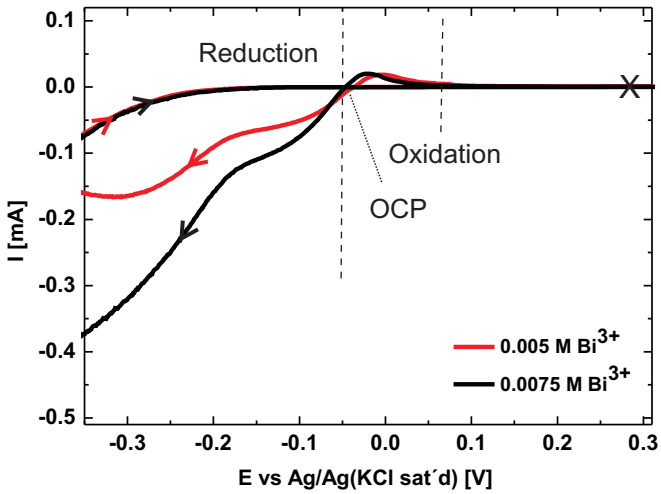

Figure 2.4: Cyclic voltammograms of bismuth antimony electrolytes containing 0.005 M of $Bi(NO_3)_3{+}5H_2O$, (red line) and 0.0075 M of $Bi(NO_3)_3{+}5H_2O$ (black line), each other concentration is kept constant at 1 M of HNO_3, 0.0056 M of Sb_2O_3 and 0.84 M of $C_4H_6O_6$.

In figure 2.4 the CVs of the two electrolytes are presented. It can be observed that for both solutions the reduction of bismuth starts at voltages lower than −50 mV vs Ag/AgCl. Antimony deposition starts at a more negative potential around −200 mV hence co-deposition of bismuth occurs. Thus potentials in the range of −80 – −250 mV are suitable for deposition of BiSb nanostructures (compare sec. 3.5.2 and sec. 4.2.2). The difference in the amount of current is caused by the different concentration of ions [1].

BiSb Electrolytes on HCl Basis

$BiCl_3$	$SbCl_3$	HCl	$C_4H_6O_6$	additives	Ref.
0.05 M	0.02 M	1 M	50 gL^{-1}	100 gL^{-1} glycerol 70 gL^{-1} NaCl aqueos ammonia to ph 1	[DZH+06]
0.04 M	0.08 M	1 M	0.27 M	0.24 M citric acid 0.1 M glycerol 1.2 M NaCl aqueos ammonia to ph 0.82	[DLL+09]
0.01 M	0.08 M	to ph 2	0.01 M	0.2 M H_3BO_3 0.1 g $CH_3(CH_2)_{11}SO_3Na$	[XFW+05]
0.05 M 0.075 M	0.02 M Sb_2O_3	0.5 M	50 gL^{-1}	100 gL^{-1} glycerol	present work

Table 2.3: Overview of BiSb electrolytes on HCl basis described in the literature.

Using bismuth(III) chloride as source for the bismuth ions and the change from nitric acid to hydrochloric as solvent are the basis for the electrolytes presented in the following. Taking the common recipes for electrolytes containing bismuth(III) chloride [LLZ+04] into account, the amount of $BiCl_3$ is chosen and varied in the same order of magnitude. Table 2.3 gives an overview of BiSb electrolytes using $BiCl_3$. Note that in the present work Sb_2O_3 is used as antimony source instead of $SbCl_3$. The amount of antimony is kept constant at 0.02 M as well as the amount of HCl and glycerol are kept constant and the concentration of $BiCl_3$ is varied between 0.05 – 0.075 M.
The cyclic voltammogram presented in figure 2.5 indicates that the reduction starts at a potential more negative than −200 mV vs Ag/AgCl. Hydrogen evolutions starts at potentials

[1] The amount of current for the black line has been normalized to the red line, huge differences were caused due to different working electrode areas used during the voltammetries.

more negative than −700 mV and the differences in the amount of current can be traced to the different concentrations of metallic ions in the electrolytes. Based on the cyclic voltam-

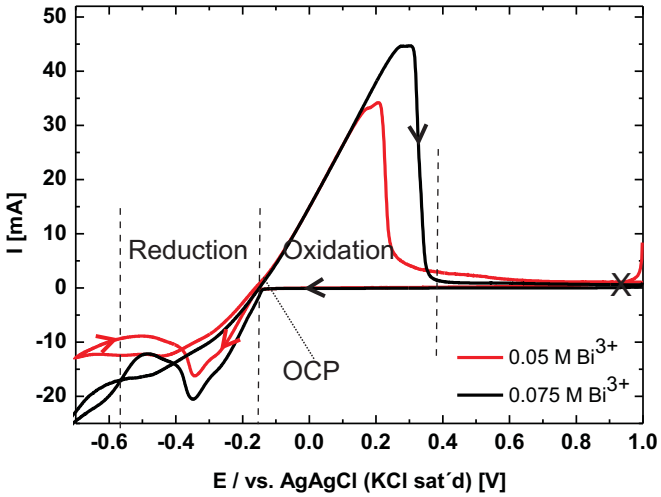

Figure 2.5: Cyclic voltammograms of bismuth antimony electrolytes containing 0.05 M of $BiCl_3$ (red line) and 0.075 M of $BiCl_3$ (black line), each other concentration is kept constant at 0.5 M of HCl, 0.02 M of Sb_2O_3 and 50 gL^{-1} of $C_4H_6O_6$.

mogram the deposition potential for the nanostructure are chosen between −220 – −370 mV (compare sec. 3.5.3 and sec. 4.2.4).

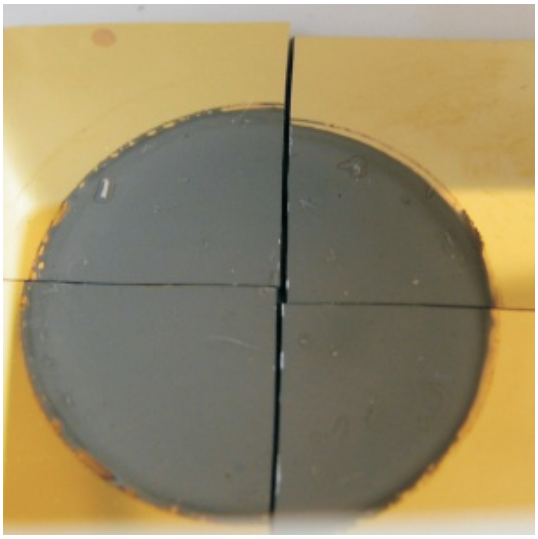

3 Bismuth and Bismuth Antimony Thin Films

Leading to the work on electrodeposited nanowires (see sec. 5), thin films are prepared and characterized in order to make first predictions on the properties of nanowires. The chemical composition of the thin films is sensitive to several conditions, like the concentration of the ions in the electrolyte, temperature and applied voltage during the deposition. More detailed information on the deposition parameters is given in section 3.1. Series of bismuth-antimony thin films are prepared to determine the conditions for the deposition of $Bi_{1-x}Sb_x$ thin films with various antimony content x. Furthermore the dependency of the SEEBECK coefficient on the antimony content is analyzed. Moreover the effect of annealing of a bismuth thin film is investigated. Due to negligible changes of the structural properties after annealing and a slightly decreasing SEEBECK coefficient, no annealing treatment are performed on the presented BiSb thin films.

3.1 Electrodeposition of Thin Films

All thin films presented in this work are deposited on standard low resistance (100) Si substrates ($\rho = 0.01 \cdot 10^{-4}\,\Omega\mathrm{m}^{-1}$). Prior to the electrodeposition, a chromium adhesion layer and 25 nm of platinum are sputtered onto the Si substrate, using a *Cressington 308R* sputter machine. More details of the sputtering parameters are given in the appendix A.2. The depositions are carried out in potentiostatic mode under normal atmosphere at room temperature for one hour. Chemical, structural and thermoelectric characterization is performed on the films as introduced below.

3.2 Characterization Methods

Different methods are used to realize a comprehensive investigation of the thermoelectric materials. For chemical and structural analysis inductively coupled plasma-optical emission spectrometry (ICP-OES), scanning electron microscopy (SEM), energy dispersive X-ray spectroscopy (EDX) and X-ray diffraction (XRD) measurements are performed. The different methods are briefly introduced here and in the sections 3.4 and 3.5 the results of the thin films are presented.

3.2.1 Composition Analysis with SEM-EDX

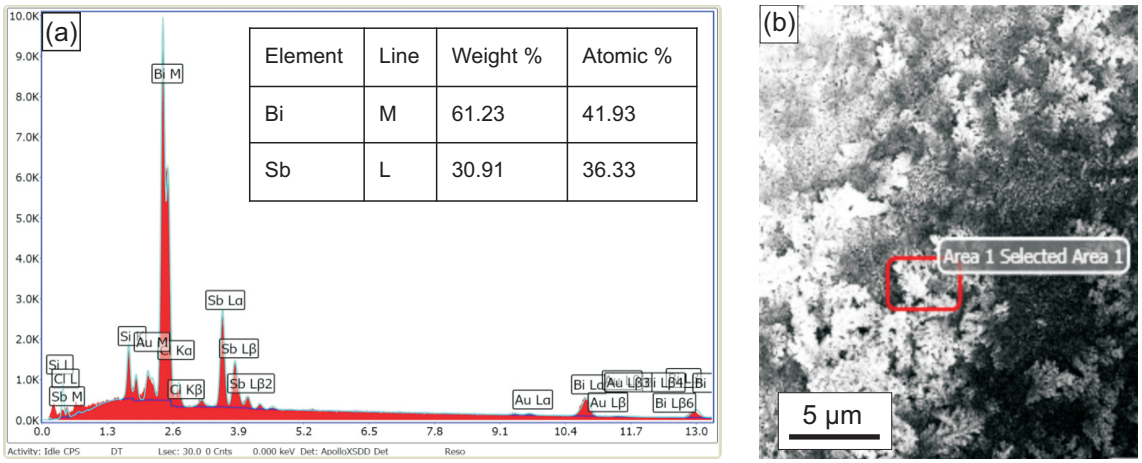

Figure 3.1: (a) Exemplary EDX graph of intensities of a BiSb thin film. (b) Scanning electron micrograph of the surface of this thin film.

To determine the composition of the thin films a scanning electron microscope from *Zeiss Sigma* equipped with an energy dispersive X-ray spectroscopy detector is used. The

scans are performed with an accelerating voltage of 20 kV. Exemplary for all results, figure 3.1 (a) shows the intensity distribution for a BiSb thin film. The deposition is carried out with a potential of −280 mV from electrolyte Cl-a-BiSb (compare appendix A.1.3)[1]. The corresponding scanning electron micrograph is given in figure 3.1 (b) with a red box marking the analyzed area. For each film several areas are scanned to obtain a mean composition. Due to the overlapping of the bismuth and antimony lines with peaks from other elements like Si, Cl and Au an accuracy of this method of roughly 10 % is estimated for the determination of the composition.

3.2.2 Structural Analysis with XRD

High resolution X-ray diffraction XRD is used for structural analysis. The in-situ XRD (see sec. 3.4) measurements have carried out by Dr. C. Schumacher and Dipl.-Phys. S. Zastrow at the University Ghent, Belgium, Department of Solid State Sciences, with a *Bruker D8 Discover XRD spectra*. Powder diffraction of the BiSb thin films has been performed by Dipl.-Phys. B. Landgraf at the University of Hamburg, Institute of Applied Physics using a *Panalytical X'Pert pro* system.
Based on Bragg 's law $n\lambda = 2d_{\mathrm{hkl}} \sin\theta$ the material specific diffraction pattern contains information on the lattice parameter, crystal structure and grain size. The lattice plane distance is d_{hkl}, the angle of the incident beam is θ, the wavelength of the beam is λ and n is the degree of the analyzed maximum. In the year 1918 Scherrer published his famous equation:

$$B(2\theta)\,[\mathrm{rad}] = \frac{K \cdot \lambda}{D \cdot \cos\theta} \tag{3.1}$$

where B is the peak width and D is the extent of the grain lateral to the lattice plane. The Scherrer factor K depends on the shape and the size distribution of the grains and takes values from $K = 0.62 - 2.08$ [LW78]. Most common is the assumption of $K \approx 1$ for spherical nanoparticals.

3.2.3 Chemical Analysis with ICP-OES

The samples have been analyzed in the Department of Analytical Chemistry (University of Hamburg) by Dipl.-Chem. K. Reinsberg by using inductively coupled plasma-optical emission spectrometry ICP-OES within the system *Spectro CirosCCD©* (*Spectro Analytical Instrument*) to determine the atomic content of bismuth and antimony. For the analysis the

[1] The table in the inset only shows the values for Bi and Sb, there are also some counts for foreign atoms like Au and Si from the substrate and Cl from the electrolyte.

whole deposited film is dissolved in hydrochloric and nitric acid. Subsequently the dilution is atomized in the inductively coupled plasma. Element-specific emission lines from the digest are detected by multiple charge-coupled device (CCD) detectors and are analyzed. More details can be found in [Sch12, RSNCB11]. The advantage of the method compared to EDX is the accuracy of 0.5 – 1 % in the determination of the composition. On the other hand the sample is destroyed after the analysis and no prediction concerning the homogeneity of the composition over the whole film is possible.

3.3 Thermoelectric Characterization

The Seebeck coefficient of the electrodeposited and pre-characterized thin films is investigated using a potential Seebeck microprobe (PSM) setup. The function of the (PSM) is described in more detail below. The measurement is a link between structural and thermoelectric characterization because the fluctuation of the Seebeck coefficient (compare fig. 3.3 (a)) can be ascribed to surface roughnesses of the thin film as well as to local composition variations of the deposit.

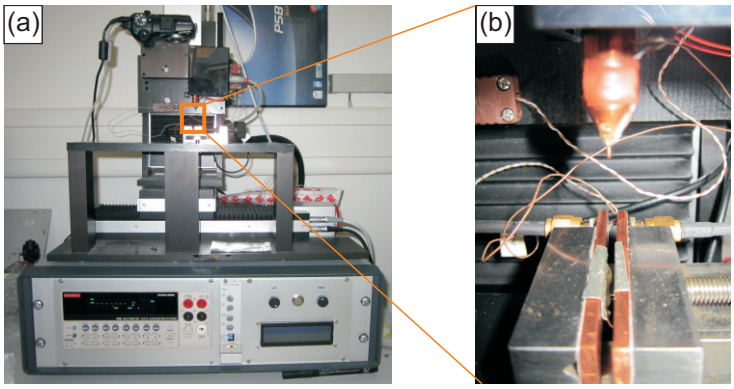

Figure 3.2: (a) Picture of the potential Seebeck microprobe measurement station. (b) Closer image of the measurement setup.

The PSM [LOT07, Zas10], depicted in figure 3.2 (a), is suitable to perform space-resolved measurements of the Seebeck coefficient S on bulk material, as well as on thin films. The photograph 3.2 (b) shows a closer view of the sample holder. A sample can be mounted between the lathe chucks, which also serve as heat sinks, and above the measurement probe is installed. During measurements the surface area is sensed piecewise with the measurement probe. The copper (Cu) tip of the probe is heated to generate a local temperature gradient on the sample. The temperature of the sample (T_0) and the temperature of the heat source (T_1) are both measured. Additionally, the potential U_2 between the measurement probe

and the sample/heat sink is measured by a CuNi wire of the probe. Also the potential U_1 between the heated sample and the tip is measured (compare the scheme in ref. [LOT07]). With the knowledge of the SEEBECK coefficients of Cu and CuNi the SEEBECK coefficient of the sample is calculated according to the equations;

$$\begin{aligned} U_1 &= (S_{\text{sample}} - S_{\text{Cu}}) \cdot (T_1 - T_0) \\ U_2 &= (S_{\text{sample}} - S_{\text{CuNi}}) \cdot (T_1 - T_0) \\ S &= \frac{U_1}{U_2 - U_1} \cdot (S_{\text{Cu}} - S_{\text{CuNi}}) + S_{Cu} \end{aligned} \tag{3.2}$$

The maximum area that can be scanned is 150 mm × 50 mm and the diameter of the tip

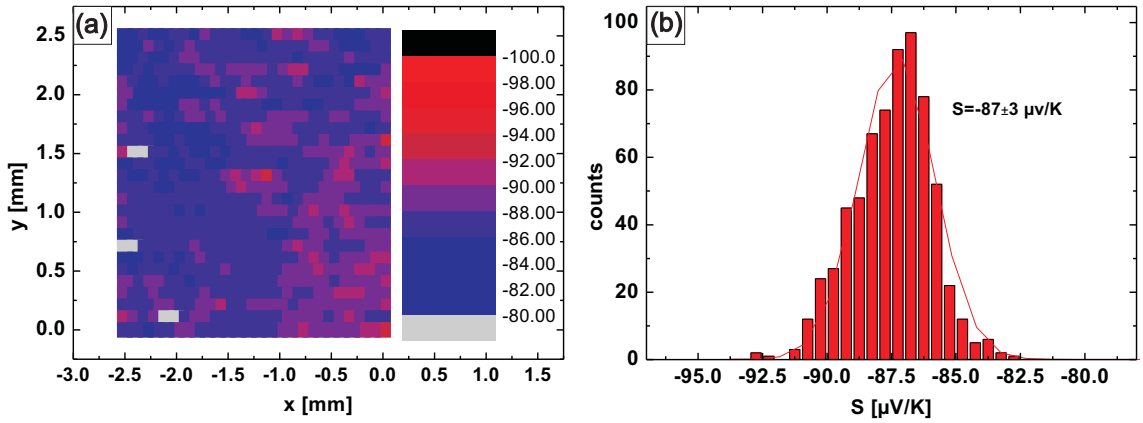

Figure 3.3: (a) SEEBECK coefficients of an area-scan on the surface of a BiSb film. (b) Abundance of the measured SEEBECK coefficients during the 2D scan.

is approximately ten micrometers. The electrodeposited thin films remain on a conductive substrate to be thermally and electrically linked to the heat sink of the PSM.
Figure 3.3 (a) shows, exemplarily for all other films, a $2.5 \times 2.5\,\text{mm}^2$ map of the SEEBECK coefficient. The corresponding electrodeposited film is deposited at a constant potential of −220 mV from the electrolyte Cl-d-BiSb (see app. A.1.3), further analysis of the composition by EDX gives an amount of 5 at % antimony and 95 at % bismuth. The abundance of the single measurements are plotted in a histogram with a interval length of $0.5\,\mu\text{VK}^{-1}$. The median as well as the standard deviation of the SEEBECK coefficient is determined by fitting a GAUSS distribution to the results. The SEEBECK coefficient is $S = -87 \pm 3\,\mu\text{VK}^{-1}$ and the small standard deviation of only $\pm 3\,\mu\text{VK}^{-1}$ allows to draw the conclusion that the composition is homogeneous over the whole film.

3.4 Pure Bismuth Thin Films

As a reference for the BiSb composite material a pure bismuth thin film is deposited and analyzed. A scanning electron micrograph of a bismuth thin film as-prepared and after

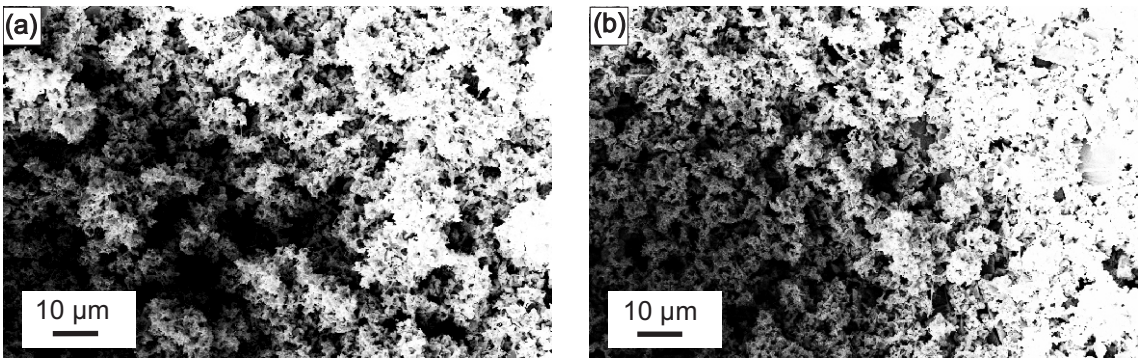

Figure 3.4: (a) SEM image of the surface of a Bi thin film as-prepared. (b) Top-view of the Bi thin film after annealing.

annealing in nitrogen atmosphere for 24 h at 200 °C is given in figure 3.4 (a)+(b). The surface structure of the film shows only minor changes.

3.4.1 Structural Analysis of Bi Thin Films

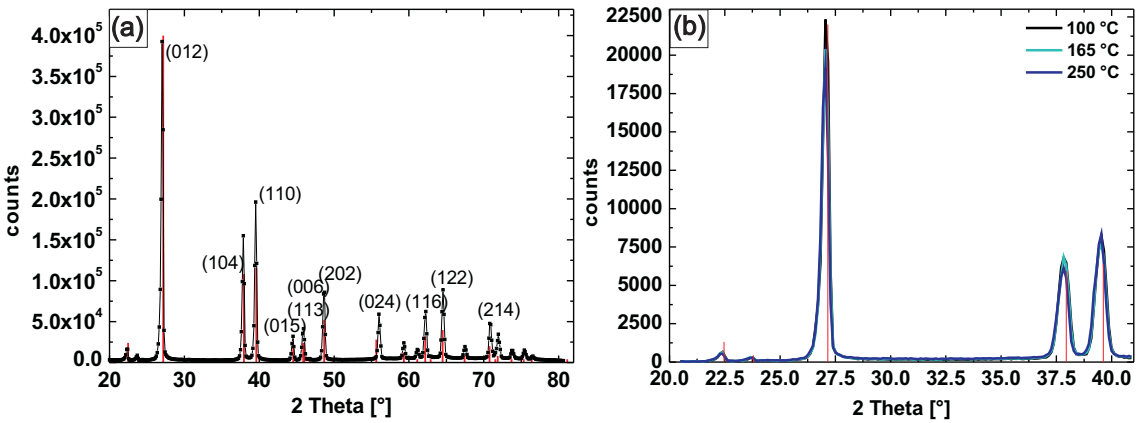

Figure 3.5: (a) Full XRD spectra of the Bi thin film; the red bars indicate the position and relative intensity of the peaks taken from the literature. (b) In-situ XRD spectra of the electrodeposited Bi thin film captured during the annealing of the sample.

The XRD results of the pure bismuth thin film are given in figure 3.5 (a)+(b). The left graph shows the full XRD spectrum of the film with the red bars indicating the position and relative intensities of the peaks of bismuth taken from the literature. The spectrum reveals that the electrodeposited thin film is polycrystalline and the good agreement of the peak positions with the positions in literature indicates that the film is single phase and there is no strain in the sample. All peaks could be indexed according to the hexagonal cell ($R\bar{3}m$). Figure 3.5 (b) shows in-situ XRD spectra which are taken during the tempering of the film. The spectra verifies the impression, given from the SEM images above, that no major change of the crystallinity of the film occurs during an annealing process.
Chien *et al.* [YLH+99, CYL+00] reports on electrodeposited Bi thin films from aqueous solutions onto Si(100) wafers with a 10 nm thick Au layer at room temperature. The deposition conditions are comparable to those used in this work and they found the as-prepared films to be polycrystalline. The films changed to single crystals at temperature near 268 °C which is very close to the melting point of bismuth (271.2 °C). Depending on the previously used deposition parameters the resulting single crystal thin films showed different orientations.

3.4.2 Seebeck Coefficient of Bi Thin Films

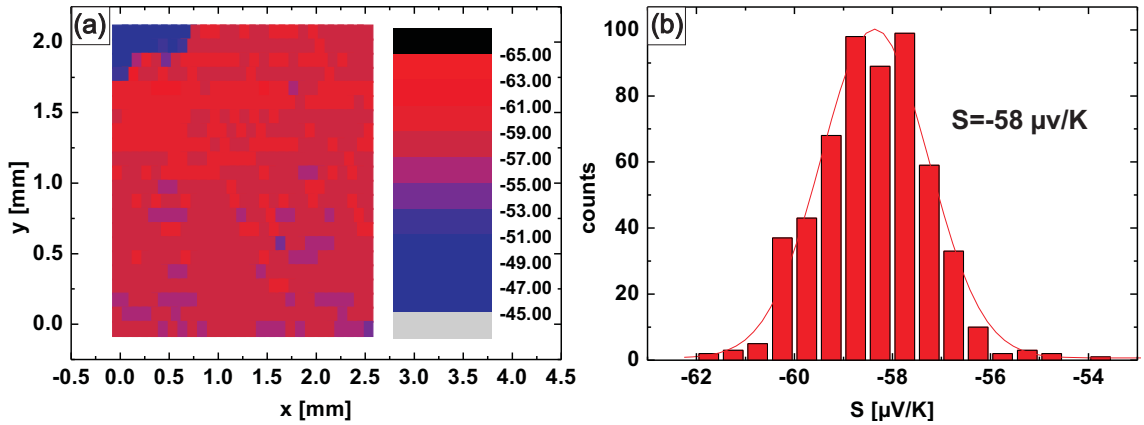

Figure 3.6: (a) Seebeck coefficients of an area-scan on the surface of an as-prepared Bi thin film. (b) Abundance of the measured Seebeck coefficients during the 2D scan.

To complete the analysis the Seebeck coefficient at room temperature room temperature (RT) of the bismuth thin film is measured before and after the heat treatment. The map of the Seebeck coefficient and the abundance of the measured results in intervals of 0.5 µVK and 1 µVK are shown in figure 3.6 and 3.7. The measured value of the Seebeck coefficient is $S = -58 \pm 1.5\,\mu VK^{-1}$ for an as-prepared pure bismuth film and is used as a reference for the results on BiSb thin films. After annealing the film the Seebeck coefficient is determined

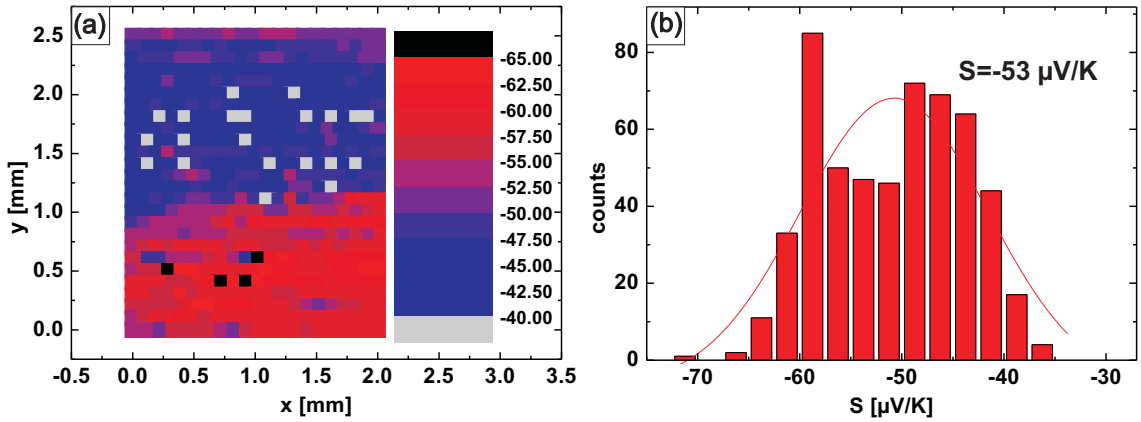

Figure 3.7: (a) Seebeck coefficients of an area-scan on the surface of an annealed Bi thin film. (b) Abundance of the measured Seebeck coefficients during the 2D scan.

S(300 K) $[\mu VK^{-1}]$	**preparation**	**comments**	**Ref.**
−30 – -62	vacuum evaporation on glass substrates	*S* measured between 300 – 470 K	[DS87]
−55	MBE grown on CdTe (211)	measurements transverse and perpendicular to the growth direction	[Cho99]
−10 – −55	vacuum evaporation on glass substrates	polycrystalline films	[BLJ+00]
−55	vacuum evaporation on glass, mica and polyamide	*S* is at RT the same for all substrates	[Kom99]
−58	electrodeposition	as-prepared	present work
−53	electrodeposition	annealed	present work

Table 3.1: Overview of the reported Seebeck coefficients of pure Bi thin films.

again.

Some values of the Seebeck coefficient at room temperature of Bi thin films reported in literature are given in table 3.1. Even so the here studied bismuth thin films are polycrystalline the absolute value of the Seebeck coefficient correspond to those measured for bulk Bi single crystals ($S = -51.4\,\mu VK$) perpendicular to the three fold axis [Cha59].

However since no reports on the Seebeck coefficient of electrodeposited bismuth thin films are available no direct comparison between those can be drawn. However, it seems feasible that the here investigated polycrystalline bismuth thin films can compete with thin films prepared with either high vacuum or high pressure methods, but without the need for an expensive and complex experimental equipment.

3.5 Bismuth Antimony Thin Films

Numerous thin films are deposited potentiostatically using the electrolytes on HNO_3 and HCl basis, presented in the section 2.2.2. The deposition of the bismuth antimony thin films is carried out with different deposition potentials at room temperature The chemical composition as well as the thermoelectric properties of the films are analyzed depending on the deposition potential and the antimony content respectively. On selected BiSb thin films X-ray diffraction spectroscopy is performed in order to gain information about structural changes due to variations in the composition.

3.5.1 Structural Analysis of BiSb Thin Films

Figure 3.8 (a)-(f) shows the XRD spectra of a series of thin films containing different amounts of antimony. For comparison the peak position of pure Bi and Sb phases are given in fig. 3.8 (a) and (f). The displayed peaks correspond to lattices with a trigonal symmetry ($R\bar{3}m$). All peaks in the following BiSb spectra are indexed on the basis of the hexagonal cell, proving a single phase, as it has already been observed for pure Bi thin film (compare sec. 3.4).
The spectrum of the bismuth antimony film shown in fig. 3.8 (b) contains all expected peaks indicating a polycrystalline phase. With increasing antimony content all peaks expect for the (012) peak become less pronounced. The thin film with Sb > 50 at % appears to be highly textured and the position of the (012) peak has shifted to the value of pure Sb. Comparable results have been reported for $Bi_{1-x}Sb_x$ electrodeposited thin films deposited galvanostatic and potentiostatic [BBL00, VRSS03].
The average grain size of the thin films is calculated using equation (3.1). The peak width B, the full width half maximum (FWHM) of the peaks is determined and the Scherrer factor K of 0.62 – 2.08 reveals grains size of a few ten nanometer. For $K = 1$ the calculated grain size of the films with an antimony content ≤ 16 at % and pure bismuth films is ~ 40 nm.

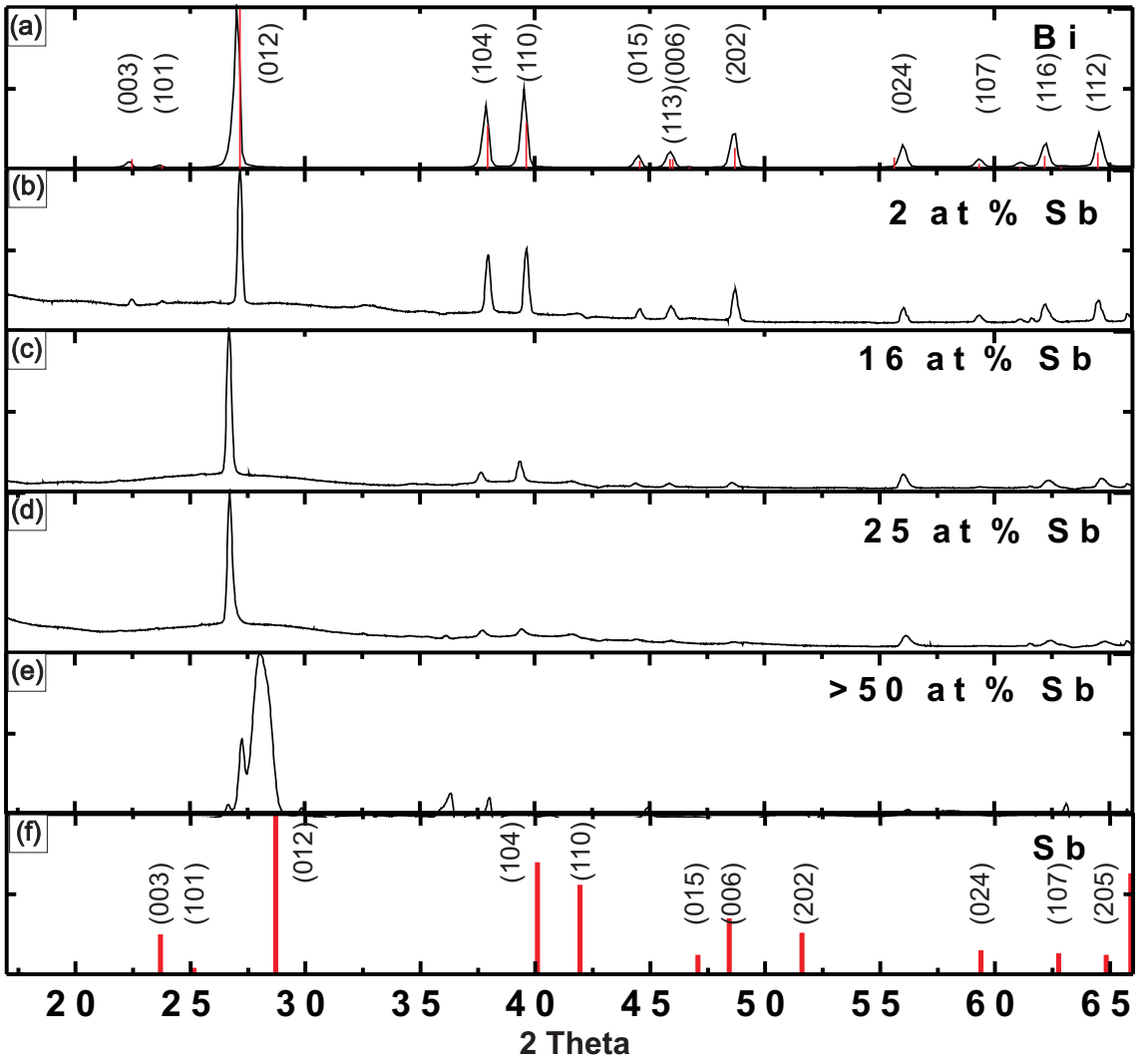

Figure 3.8: X-ray diffraction spectroscopy diagrams of electrodeposited BiSb thin films, (a) pure bismuth thin film, (b) thin film obtaining ~ 2 at % Sb, (c) ~ 16 at % Sb, (d) ~ 25 at % Sb and (e) > 50 at % Sb, (f) indexed peak positions of pure antimony.

3.5.2 Thin Films from BiSb Electrolytes on HNO_3 Basis

Thin films are prepared from the electrolytes described in section 2.2.2 with potentials reaching from −80 mV to −250 mV and the antimony content is determined. The antimony content of the thin films versus the deposition potential is given in figure 3.9 (a). It is shown that the antimony concentration of the films stays below < 10 at % for deposition potentials down to −180 mV. Also, at more negative voltages the antimony content saturates at a value around 60 – 70 at % independent of the deposition potential. In the small range from −180 mV to −200 mV the antimony concentration increases dramatically. Since the Bi/Sb ratio between

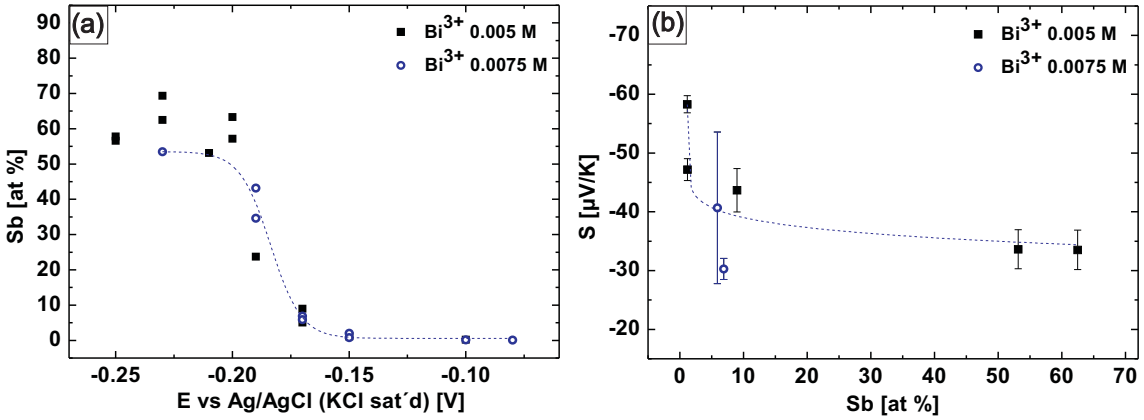

Figure 3.9: (a) Composition of BiSb thin films, deposited at various potentials from HNO_3 electrolytes. (b) SEEBECK coefficients of electrodeposited thin films versus the antimony concentration.

both electrolytes does not differ significantly they both show the same behavior.
The investigation of the SEEBECK coefficient depending on the antimony content implies an increase of the total value with decreasing antimony content. For thin films with an antimony concentration above 50 at % the SEEBECK coefficient saturates at a value of $-35\ \mu VK^{-1}$. Whereas S becomes more sensitive to changes in the concentration for an antimony content below 20 at %. The highest value of $S = -57 \pm 2\ \mu VK^{-1}$ is reached at the lowest antimony concentration (Sb < 2 at %). The dashed line in figure 3.9 (b) is a guide to the eye and the red spot marks the value of the SEEBECK coefficient for pure bismuth. Thus BiSb thin films deposited from electrolytes on HNO_3 basis can reach the same thermoelectric performance as pure bismuth thin films but could not extend beyond that.

3.5.3 Thin Films from BiSb Electrolytes on HCl Basis

A series of thin films is deposited from two different aqueous electrolytes with HCl as a solvent and varying bismuth content. The details for the used solutions can be found in section 2.2.2 and appendix A.1.3. The depositions are performed in a potential range between −220 mV and −370 mV in potentiostatic mode.

Figure 3.10 (a) gives the results of the composition analyses for both electrolytes. The black and the blue dashed line are linear fits to the data points found for the electrolyte with a bismuth concentration of 0.05 M and 0.075 M bismuth(III) chloride, respectively. Both electrolytes show the same slope with an offset regarding the different bismuth/antimony ratio of the electrolytes. The antimony content can be varied constantly in a range of 0 – 60 at % by passing the deposition voltage through from −370 mV to −220 mV. Figure 3.10 (b) shows

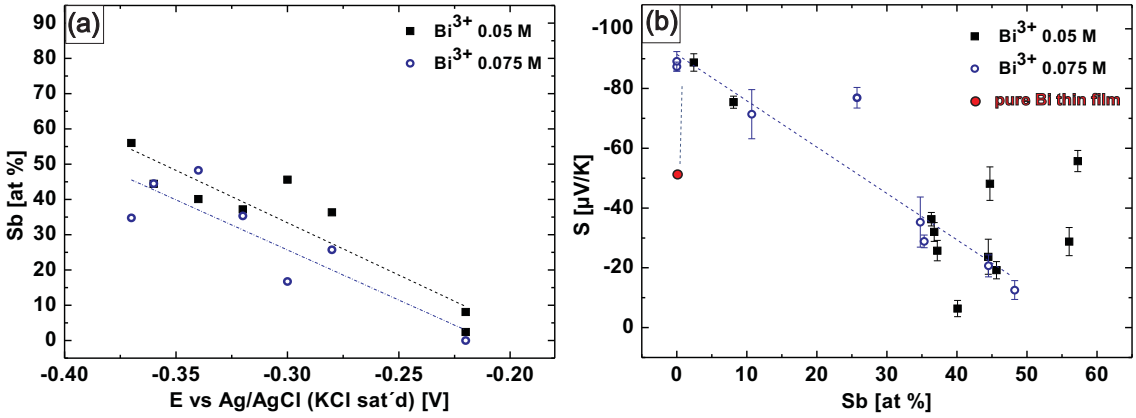

Figure 3.10: (a) Composition of BiSb thin films, deposited at various potentials from HCl electrolytes. (b) SEEBECK coefficients of electrodeposited thin films versus the antimony concentration.

that in the range of 0 to 50 at % the absolute value of the SEEBECK coefficient decreases with increasing antimony concentration. The dashed line is a linear fit to the data points with Sb< 50 at %. Above that the absolute value of the SEEBECK coefficient increases again. The highest SEEBECK values are found for the films with the lowest antimony concentrations. Thin films with an antimony content < 5 at % have the highest values of $S = -85\,\mu VK^{-1}$ which is remarkably higher compared to the value reached for pure bismuth thin films (see sec. 3.4). Based on the results, depositions of nanowires from these electrolytes with deposition potentials of more positive values than −300 mV is performed to achieve wires with an antimony content < 15 at % (see sec. 4.2.4 and 4.3.2).

S(300 K) $[\mu VK^{-1}]$	**structure**	**preparation**	**$Bi_{1-x}Sb_x$**	**Ref.**
−60 – −76	single crystals	BRIDGAM method	$0.1 < x < 0.13$	[Aon78]
−110	single crystals	zone melting	$0.05 < x < 0.12$	[SW62]
−57	polycrystalline alloys	hot pressing	$x = 0.15$ and $x = 0.33$	[LGH+13]
−77	1000 nm	MBE grown on CdTe(211)	$x = 0.08$	[Cho99]
-50 – -100	1000 nm	MBE grown on CdTe(111)	$0 \leq x \leq 0.18$	[CDW+99]

Table 3.2: Overview of the reported SEEBECK coefficients of BiSb alloys.

Most of the publications on electrodeposited $Bi_{1-x}Sb_x$ thin films concentrate on the optimization of the electrolyte [BBL00, MGPK+03] (also compare sec. 2.2.2). No SEEBECK co-

efficient of electrodeposited BiSb thin films have been reported yet. Nevertheless numerous reports on single crystalline as well as polycrystalline $Bi_{1-x}Sb_x$ alloys prepared with different techniques are available. The table 3.2 give a small overview on Seebeck coefficients reported in literature.
The best thermoelectric performance is shown for antimony concentrations < 12 at %. For films with higher antimony concentration Trefny [Tre81] measured values of the Seebeck coefficient even below that of pure bismuth thin films, which is an effect that has also been observed for the here presented electrodeposited thin films (compare fig. 3.10 (b)). In 1962 Smith and Wolfe [SW62] found the Seebeck coefficient at room temperature to be the highest for single crystal BiSb alloys containing 5 at % with a value of $S = 110\,\mu VK^{-1}$, whereas the highest absolute value of $S = -220\,\mu VK^{-1}$ is reached for the 12 at % antimony alloy at 20 K. The magneto-Seebeck coefficients for $Bi_{1-x}Sb_x$ alloys with 0, 2, 5, 8 and 12 at % have been calculated using the Boltzmann equation by [TKY+08]. The found room temperature values for S are between approx. $-70\,\mu VK^{-1}$ and $-140\,\mu VK^{-1}$ with the highest value for a antimony concentration of 5 at %. Yim and Amith [YA72] found that the absolute value of the Seebeck coefficient for $Bi_{1-x}Sb_x$ single crystal alloys increases with increasing antimony content up to 12 at % Sb and decreases with further addition of antimony until for a high (>60 %) Sb concentration a change in the sign from negative to positive occurs. The measured values at 300 K are between $-55\,\mu VK^{-1}$ for pure bismuth and $-90\,\mu VK^{-1}$ for $Bi_{0.88}Sb_{0.12}$, measured perpendicular to the trigonal axis. Also for polycrystalline $Bi_{1-x}Sb_x$ alloys the samples with an antimony concentrations of 12 at % showed the best performance with a Seebeck coefficient of $-100\,\mu VK^{-1}$ [DSRD09].

Overall it can be stated that the absolute Seebeck coefficient of BiSb alloys is higher than that of pure bismuth with the best performances shown for alloys with low antimony content ($x < 0.18$). In case of the electrodeposited thin films the best performance is reached for Sb < 10 at %. In section 5.4 the Seebeck coefficient of single BiSb nanowire of similar composition is analyzed.

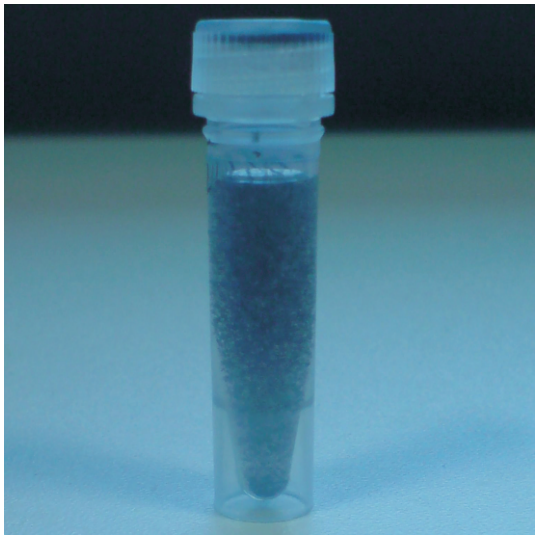

4 Template Assisted Electrodeposition of Nanowires

The controlled electrochemical oxidation (anodization) of aluminum to anodic aluminum oxide (AAO) membranes is a well-known technique for many years. These membranes are often used as templates for different cylindrical nanostructures. The next two pages show a scheme of the different preparation steps. During the first anodization step (I), after the electropolishing of pure aluminum chips, a porous unordered aluminum oxide layer is formed. Dissolution of aluminum oxide leaves the surface of the aluminum chip with periodical imprints (II), which lead to an ordered porous AAO structure after a second anodization process (III). For the usage of the membranes as templates for nanowires the backside is opened wet chemically and one side is covered with an Au film (IV). Such membrane can then be filled by electrodepostion (V) (see sec. 4.2). A detailed oversight of the electrodeposition of nanowires is given in section 4.2 Removing the Au film again (VI) and the dissolution of the membrane (VII) enables the contacting of single wires for electrical characterization (VIII) described in the chapter 5.1. It also allows the structural characterization of single wires by transmission electron microscopy (TEM), which is presented in section 4.3.

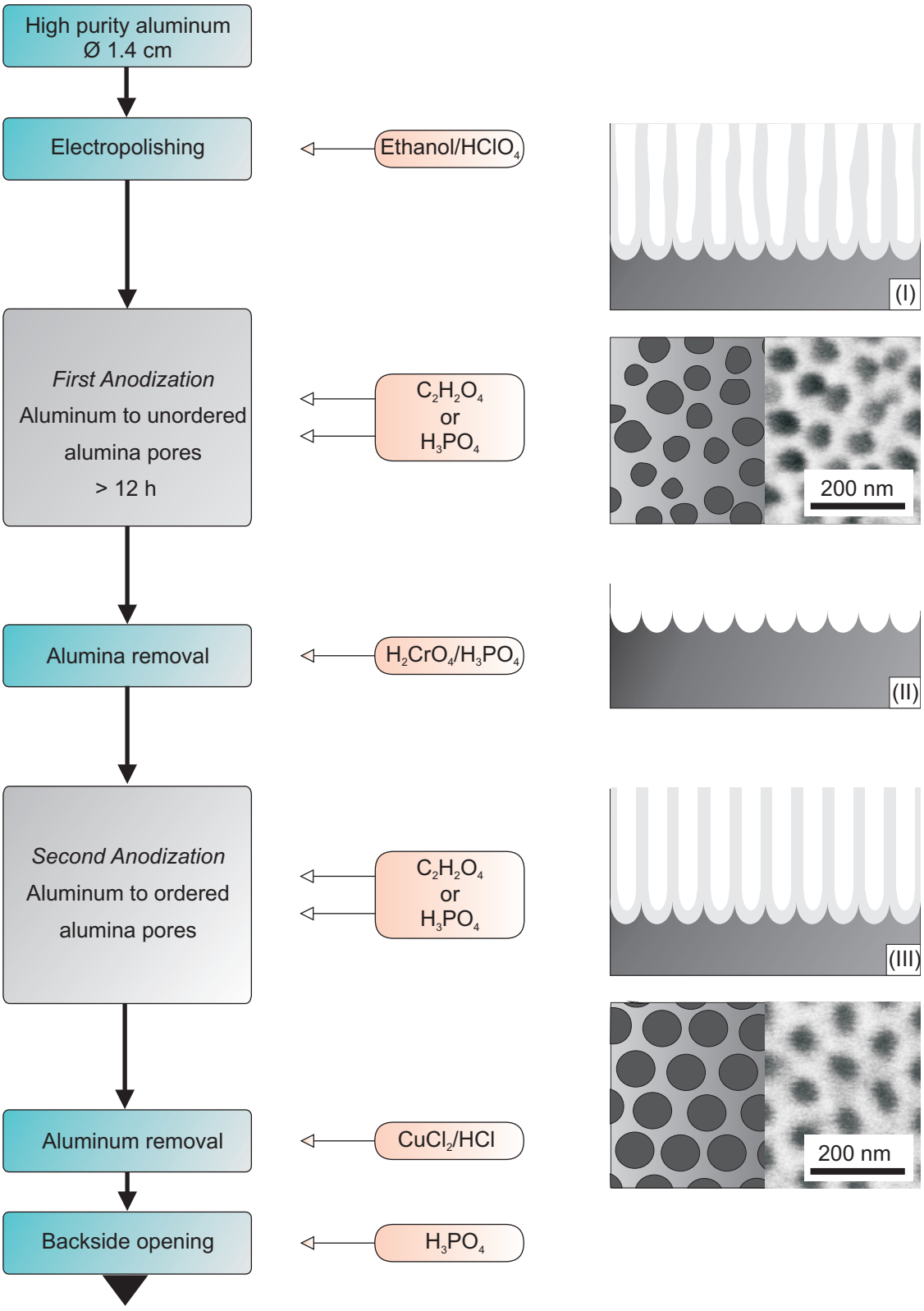

Figure 4.1: Scheme of the preparation steps of the AAO membranes to use as templates for the electrodeposition of nanowires.

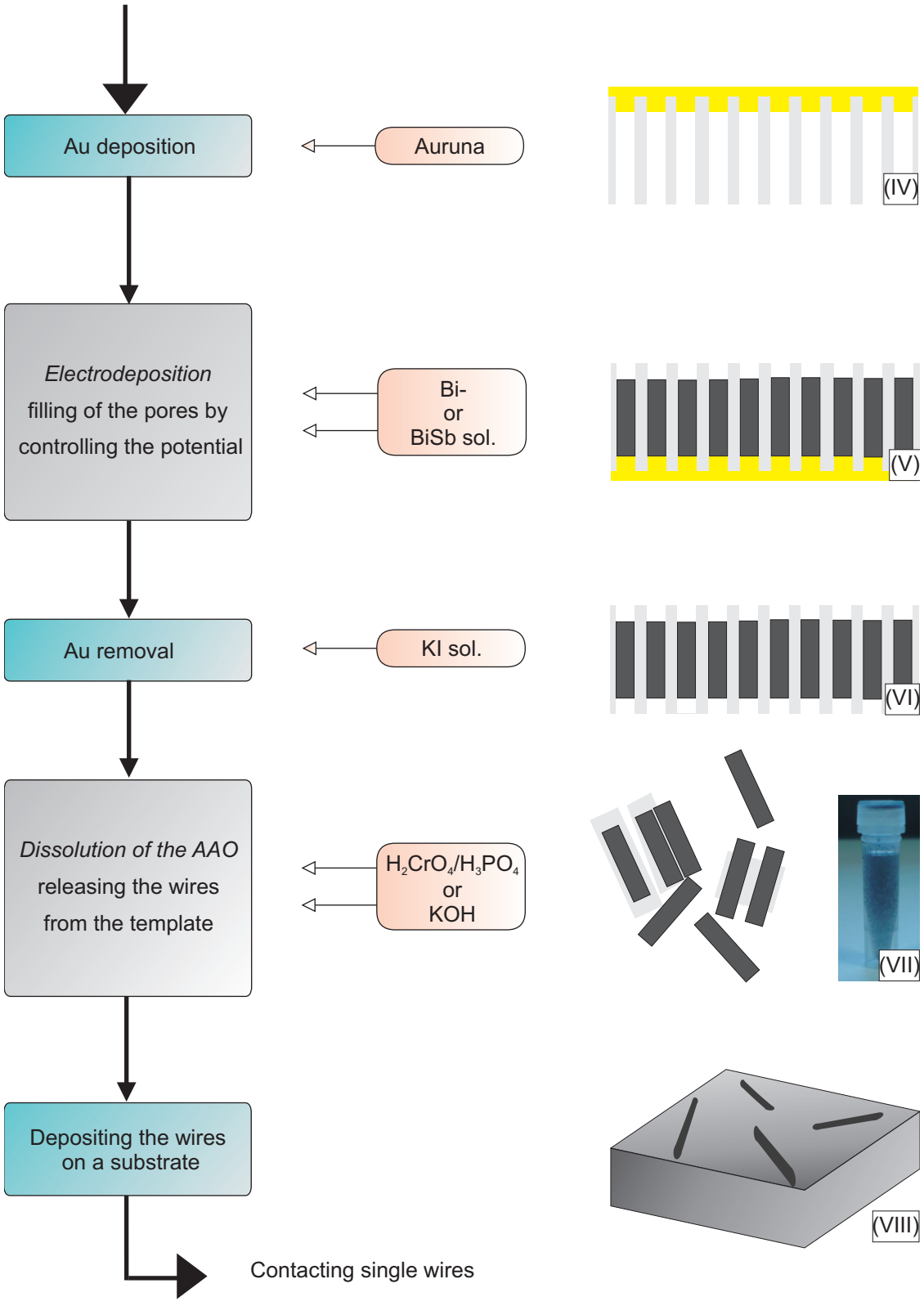

Figure 4.2: Scheme of the preparation steps of the AAO membranes, continued and their subsequent use as templates for the electrodeposition of nanowires.

4.1 Preparation of AAO Membranes

During this work, oxalic acid membranes as well as phosphoric acid membranes are fabricated as templates for the electrodeposition of nanowires. Both processes are based on a two step anodization process of high purity aluminum with an acidic electrolyte which leads to self-ordered pores within the membrane [MF95, Sul08, YHSX04]. In former years, a lot of efforts were made to find the optimum conditions for the growth of these structures in different acids, i.e. sulfuric acid [ZLPZ07, KSVD04, SSM+02], oxalic acid [SBZJ10] and phoshporic acid [NCS+02, YHSX04]. Beside straight ordered pores also y-shape structures and other AAO types, like modulated pores can be designed by changing the anodization conditions [HMX+11, TMB+04, LJGN06]. Since the literature is already wide on this field the following chapter is supposed to give a brief overview of the different membranes that have been prepared in the interim of this thesis.

The synthesis route starts with the electropolishing of aluminum chips to clean and flatten their surfaces. This is realized with a mixture of perchloric acid and ethanol for three minutes at a potential of 20 V. During the following first anodization the nucleation of the pores occurs randomly at small edges of the aluminum surface resulting in an unordered alumina pore structure. With proceeding time the pores become more uniform in size and interpore distance, leading to a periodic structure on the surface of the aluminum chip after removing this first alumina layer (compare fig. 4.1 (II)). These imprints are the nucleation sites for the pores at the beginning of the second anodization resulting in an ordered array of nanopores that have been grown perpendicular to the aluminum surface, as it can be seen in figure 4.3.

Using oxalic acid the anodizations is carried out at 8 °C and a potential of 40 V wherein the

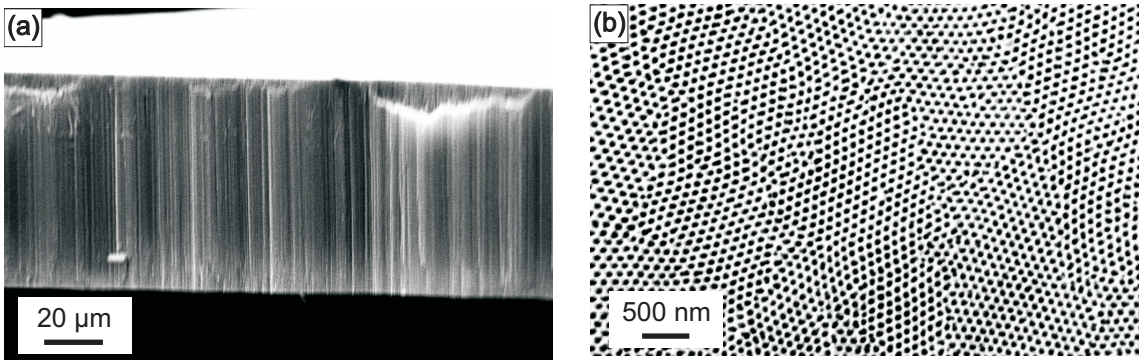

Figure 4.3: (a) Cross-section of an AAO membrane. (b) Top view of nanopores with a long range order.

first anodization runs at least 12 h to ensure periodical imprints on the aluminum surface. During the second anodization the pores have been formed with a growth rate of 3.5 $\mu m h^{-1}$. The anodizations with phosphoric acid is run at 2 °C and a potential of 195 V. In order to avoid fusing of the aluminum chips, the first three hours of the anodizations are carried out at 170 V. After the removal of the AAO layer the second anodizations runs directly at a potential of 195 V. The growth rate for phosphoric acid membranes is 2 $\mu m h^{-1}$. More details of the process are given in the appendix A.3.
Figure 4.4 (a) shows a representative scanning electron micrograph of the top view of an oxalic acid membrane with a typical pore diameter of 60 nm and an inter-pore distance of 120 nm. For comparison, a top view of a phosphoric acid membrane with an average pore diameter of 200 nm and an inter-pore distance of 400 nm is given in figure 4.4 (b).
To achieve free standing AAO membranes, the backside aluminum and the barrier oxide

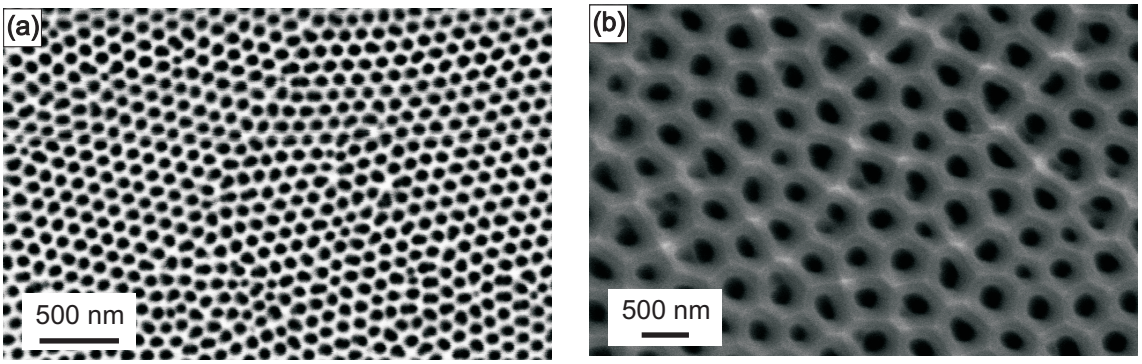

Figure 4.4: a) Top view of an oxalic acid membrane with typical pore diameter of 60 nm. b) Top view of a phosphoric acid membrane with typical pore diameter of 200 nm.

at the bottom of the pores is removed using wet chemical etching (see app. A.3.7). Since the membranes are used as templates for the electrodeposition of nanowires, a thin (20 nm) gold layer is sputtered at the back side of the membrane. To mechanically stabilize this layer and to close the back side of the membrane more gold is deposited electrochemically from a commercial Auruna 5000 (*umicore Electroplating*) solution (compare fig. 4.2). This gold layer forms the electrical contact for the following electrodeposition into the pores.

4.1.1 Nanostrutured AAO Membranes

For measurements on single nanowires (see sec. 5) it is important to release the wires from the membranes. This is done wet chemically e.g. with chromic acid or a strong base like NaOH or KOH. Due to its filling no solvent can infiltrate the membrane. Thus lateral etching of the alumina is suppressed and dissolution may take up to weeks with a mixture of

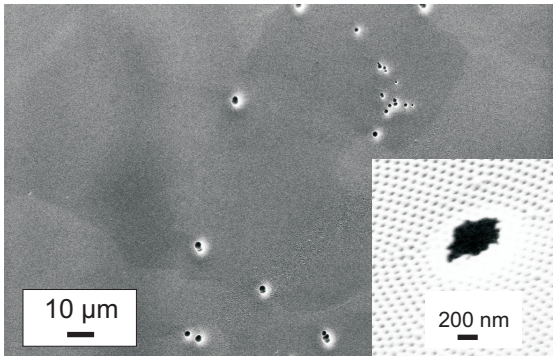

Figure 4.5: Top view of front side of an oxalic acid membranes with major damages in the long range order.

chromic and phosphoric acid in a warming cabinet at 42 °C. By designing a template that allows the filling of only every third pore this process might be strongly accelerated.

An approach that is investigated in this work is based on the work of Han *et al.* [HMX+11]. The aim is to prepare AAO membranes with a diameter of 60 nm but to have every third pore blocked. The preparation route follows the standard process for oxalic acid membranes with one difference: at the end of the second anodization process, the voltage is increased to a potential of 70 V. Reducing the voltage by the factor $\frac{1}{\sqrt{n}}$ (n; non-negative integer) during anodization, leads to branched pores with decreased diameters of the branches [MJC+05, CAEL99]. On the other hand, increasing the voltage is supposed to cause the opposite effect on the further growth. Theoretically, by increasing the voltage by the factor $\sqrt{3}$ only every third pore can continue growing with increased diameter and the other pores are blocked. The relation between the inter-pore distance D_{int} and the applied voltage U can roughly be described by the expression: $D_{\text{int}} = 2.5\,\text{nmV}^{-1} \times \text{U}$ [BGG+08].

First experiments with just increasing the voltage from 40 V to 70 V in the last period of the second anodization shows that this approach works in principle, but the quality of the membranes may be improved. As expected, the pores at the bottom of the alumina exhibit a larger diameter than on top of the membrane, but the long range order indicates major damages (compare fig. 4.5). This is due to stress in the aluminum oxide caused by the higher voltage. Some efforts are made to optimize the conditions in the final anodization stage. Satisfying results are achieved by cooling the system down to 2 °C before increasing the voltage. Further improvements are observed by rising the voltage stepwise from 40 V to 70 V with a speed of 0.1 mVs^{-1}. The results of the experiments are given in the overview 4.6. The first micrograph shows the front side of a membrane with the oxalic acid-typical pore width of 60 nm, the next micrograph demonstrates the enlarged pore diameter at the bottom

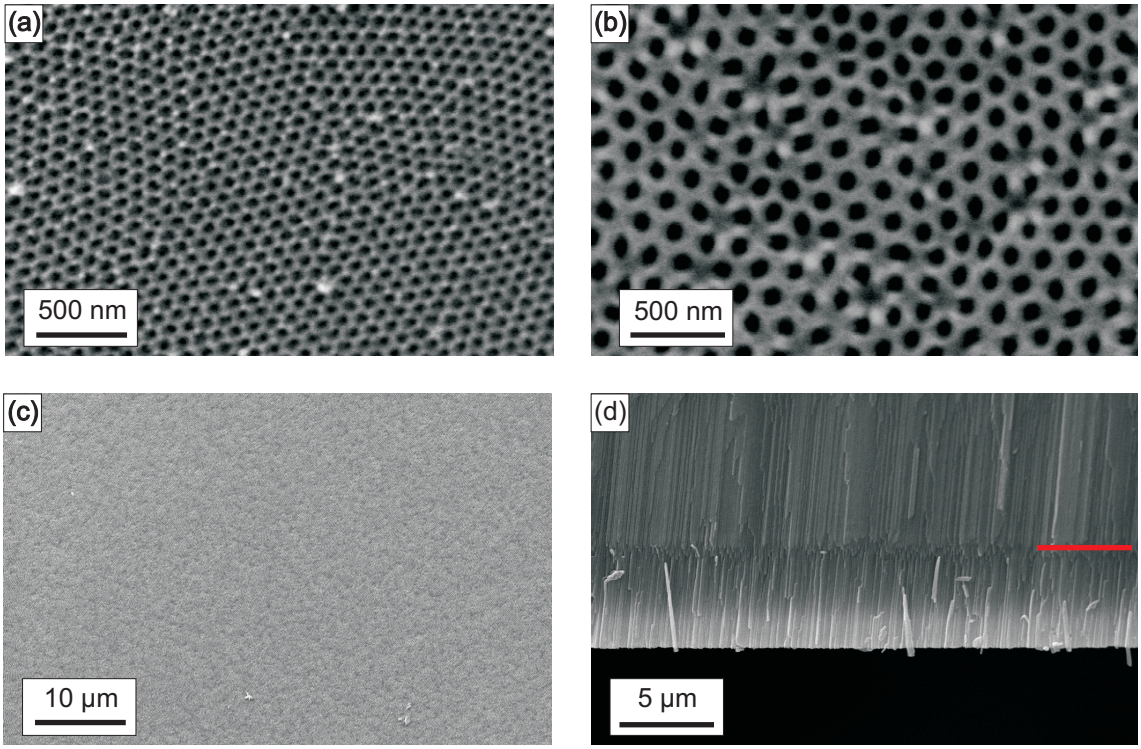

Figure 4.6: (a) Top view of the front side of oxalic acid membranes with a pore diameter of 60 nm. (b) Top view of the back side of a oxalic acid membrane with a pore diameter of 70 nm due to increasing the anodization potential to 70 V. (c) Overview of the front side without major damages. (d) Cleaved edge of the membrane, the bar indicates the point where the pores start to grow with an increased diameter.

side of the membrane, the change of the diameter can also bee seen at the cleaved edge shown in picture 4.6 (d). The wide-range plane view of the membranes (see fig. 4.6 (c)) does not reveal major damages in the membrane. The results are verified in practical test and it is proven that these nanostructured oxalic acid AAO membranes dissolve faster.

4.1.2 Modulated AAO Membranes

Since on the nanometer scale the electronic properties of wires strongly depend on the diameter, it is not only interesting to prepare wires with tailor-made diameters but also such with modulated diameter. Different approaches are well-established to produce adequate AAO-membranes as templates. Besides alternating steps of mild and hard anodization [LJGN06] to prepare membranes with uniform diameter modulations, it is also possible to achieve modulated pores by means of wet chemical etching and atomic layer deposition. This approach has been pursued in this work.

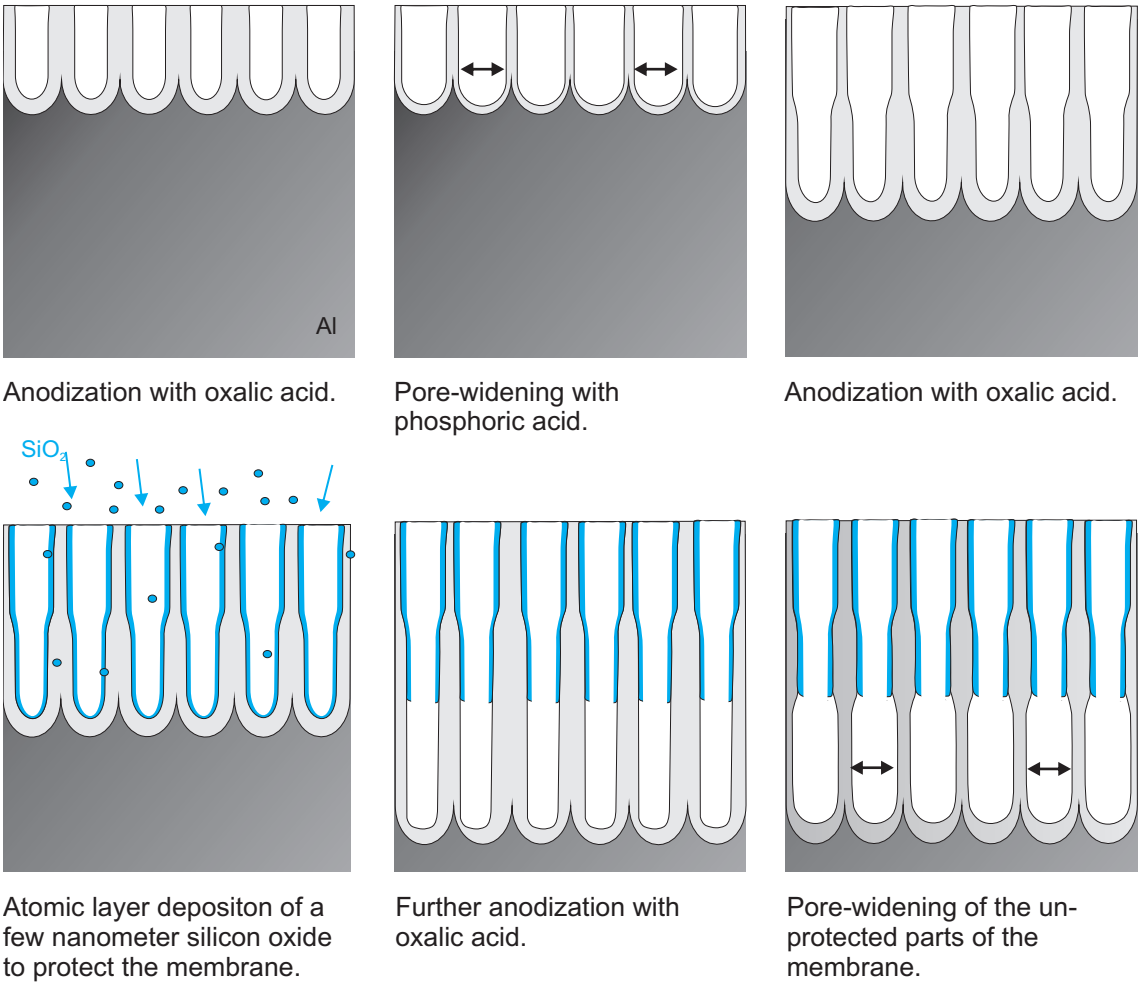

Figure 4.7: Scheme of the preparation steps to achieve modulated AAO membranes.

An overview of the process is given in the schematic diagram 4.7. After the first anodization process and the removal of the aluminum oxide membrane, a second anodization under common conditions (see sec. 4.1) can be started. The duration of the first interval of the second anodization determines the length of the first segment. Afterwards, the obtained pores are widened with phosphoric acid (10 wt %) at 42 °C with an etch rate of about 1 nm min^{-1}. Further anodization with oxalic acid will continue the growth of the membrane with the familiar diameter of 60 nm. A following intermediate step allows to cover the inner walls of the pores with a very thin (1.75 nm) layer of silicon dioxide by ALD. To achieve an additional modulation, the anodization is resumed. Afterwards the pores can be widened again with phosphoric acid, but now only the last grown part of the membranes is etched by the acid whereas the rest is protected due to the silicon dioxide layer. With this technique modulated pores, as presented in the last sketch of figure 4.7, can be realized. The diameter transitions

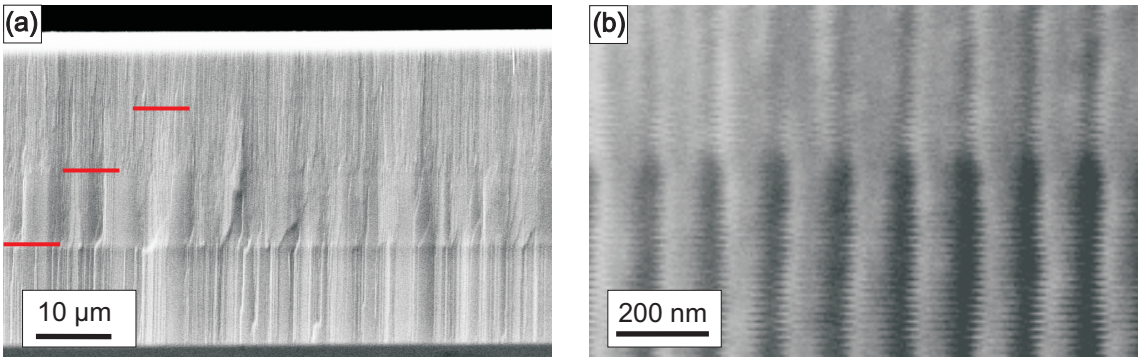

Figure 4.8: (a) Cleaved edge of a AAO membrane with four diameter modulations. (b) Closer view of one modulation.

go from ~ 75 nm for the bigger parts to ~ 55 nm for the thinner parts. The scanning electron micrographs in figure 4.8 gives a first impression of such modulated membranes. Figure 4.8 (a) gives an overview of a cleaved edge of this kind of membrane. Each bar indicates the begin of a segment with varying diameter. The change of the diameter may also be seen by slight changes in the color of the micrograph. The higher magnification in figure 4.8 (b) exhibits clearly a transition from smaller to bigger diameters.

4.2 Electrodepositon of Nanowires

During the electrodeposition process into AAO membranes the ions from the electrolyte diffuse through the pores to the working electrode (cathode, compare scheme 4.2) at the pore bottom of the membrane. There, the metallic cations are reduced and they are accumulated at the bottom of the pores. So the growth takes places along the length of the pores. If the growth rate of the wires strongly differs, a limited number of pores is filled up to the top of the membrane, starting an overgrowth. Due to the transition from 1D diffusion limitation, to 3D diffusion the growth on top of the membranes is much faster compared to the nanowire growth in the membrane. Additionally, the overgrowth covers open pores and prevent further growth of the wires. Thus, to achieve large amounts of nanowires with a length in the range of several micrometers, it is essential to fill the pores homogeneously.

Numerous deposition attempts into AAO membranes, potentiostatic as well as potentiodynamic have been performed during this work. It is found that the growth rate within the pores is much more homogenous by the pulsed electrodeposition technique, as the comparison in figure 4.9 shows.

A summary of the depositions performed into AAO membranes is given in the following

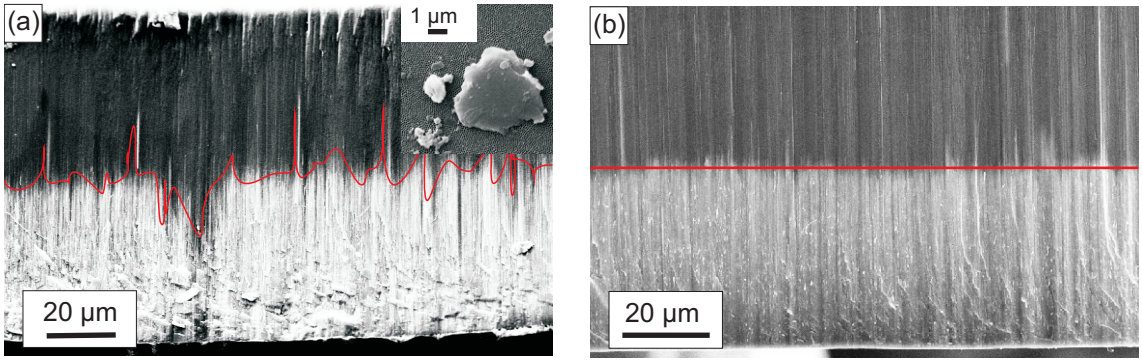

Figure 4.9: (a) Cleaved edge of an AAO membrane filled by unpulsed deposition. In the inset; overgrowth on top of the membrane. (b) Cleaved edge of an AAO membrane filled by pulsed electrodepositon.

section. As far as the samples in tables 4.1 – 4.4 are not signed further, the depositions are carried out into standard oxalic acid AAO membranes. All pulsed electrodepositions are performed potentiodynamic with t_{on} = 10 ms and t_{off} = 50 ms pulse cycles and at room temperature.

4.2.1 Electrodepostition of Bi Nanowires

sample	U_{on} [mV]	U_{off} [mV]	**time** [h]	**length** [µm]	**comments**
So2 DIV	−140	−60	4	20	AAO+SiO_2
S14 CI	−140	-60	6	30	–
S15 CI	−140	−60	5.5	30	–
S16 DI	−140	−50	5		AAO 30 min at 70 V+SiO_2
S16 AIII	−140	−60	7	35	–
S15 DII	−140	−45	6	6	AAO+SiO_2
S15 DII	−140	−45	8.5	25	AAO+SiO_2
S17 CI	−140	−45	5	10	**AAO 15** min **at 70** V**+SiO_2**
S17 CIV	−140	−60	3	25	**AAO 15** min **at 70** V**+SiO_2**
S15 BIII	−140	−45	6	–	AAO+SiO_2
Po1 CIII	−140	−60	4	30	**phosphoric acid AAO**

Table 4.1: Overview of depositions into AAO membranes from Bi electrolytes.

An overview of the depositions into AAO membranes from the described Bi electrolyte is given in the table 4.1. The samples that are dissolved from the membrane successfully are in bold print. Further structural analysis of the dissolved wires are discussed in the section 4.3.

The length of the wires is determined by scanning electron microscopy SEM from cleaved edges of the membranes as it is shown in fig. 4.9 (b). First regular oxalic acid membranes are used. Due to difficulties in forming OHMic contacts to the wires (compare sec. 5.1) some membranes are covered by ALD with a 2 nm thin SiO_2 layer, to avoid the oxidation of the wires during the process of dissolving the wires from the membranes. Finally this technique is combined with the nanostructuring of the pores by anodization at 70 V for several minutes to improve the quota of samples that are dissolved from the AAO matrix. Details of this process are described above in section 4.1.1.

4.2.2 Electrodeposition of BiSb Nanowires on HNO_3 Basis

sample	**electrolyte**	U_{on} [mV]	U_{off} [mV]	**time** [h]	**length** [µm]	**Sb** [at %]
S14 DI*	BiSb-a-sol	−180	−55	5	6 – 8	–
S14 DIV*	BiSb-a-sol	−180	–	5	6 – 8	2
S14 DIII*	BiSb-a-sol	−180	−55	5.5	6 – 8	–
S12 DII	BiSb-a-sol	−180	–	8	6 – 8	2
S14 DII*	BiSb-d-sol	−180	−45	5	6 – 8	2
S11 AII	BiSb-d-sol	−180	–	8	6 – 8	2
S15 AI	BiSb-d-sol	−160	−60	4.5	6 – 8	2
S12 CI	BiSb-d-sol	−160	−80	7.5	6 – 8	2
S15 AI	BiSb-d-sol	−160	−60	5	6 – 8	2
P01 CI	BiSb-d-sol	−200	–	4	6 – 8	2

Table 4.2: Overview of depositions into AAO membranes from BiSb electrolytes on HNO_3 basis.

Table 4.2 shows an extract of the depositions performed potentiostatically and potentiodynamically from the BiSb electrolytes on HNO_3 basis introduced in section 2.2.2, into AAO membranes. Sample names that are printed in bold letters mark samples which are dissolved from the membrane. The sample labeled P01 CI is a phosphoric acid membrane, all other depositions are carried out using oxalic acid membranes. Additionally, the stars mark samples which are deposited into nanostructured oxalic acid membranes. Those samples where no U_{off} potential is given are deposited potentiostatically. The antimony concentration is determined by SEM-EDX of cleaved edges of the membranes. Due to the limited material that is present in the membrane and overlapping peaks given from the membrane the intensity of the signal is low. Based on this analysis no final statement can be made whether the composition is homogenous throughout the whole length of the wires but a reasonable overview on the composition of the whole sample is given. A typical EDX analysis of a cleaved edge is shown in figure 4.10. Independent of the deposition times and parameters no growth front

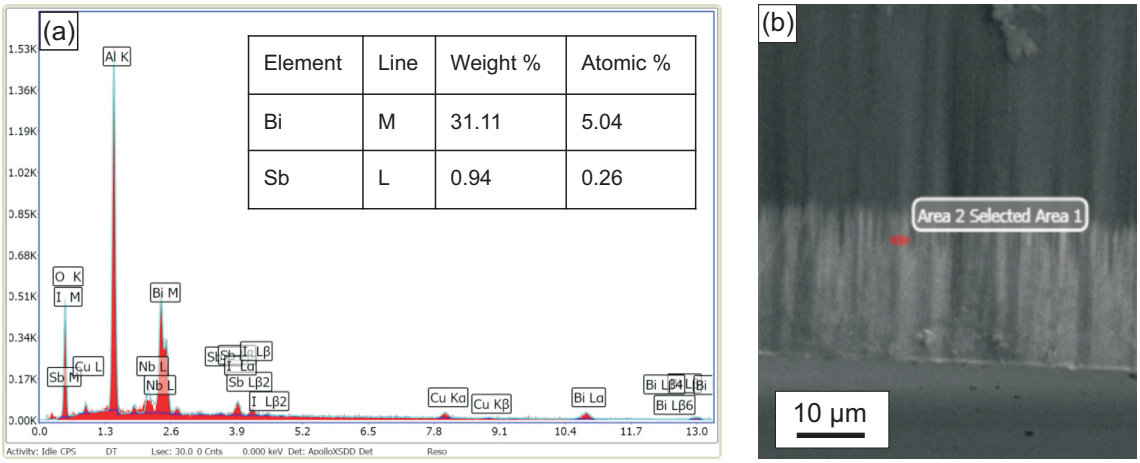

Figure 4.10: (a) Exemplary EDX graph of intensities of BiSb nanowires embedded in an AAO membrane. (b) Scanning electron micrograph of the cleaved edge of a filled AAO membrane.

exceeded a height of 6–8 µm, hence these wires are too short to form electrical contacts onto them by laser lithography (compare sec. 5.1 and sec. 5.2.1). Probably at this length the resistance of the wires reaches a magnitude where the applied deposition potential is no longer sufficient to drag ions from the solution into the membranes.

4.2.3 Galvanostatic Deposition of BiSb Nanowires on HNO_3 Basis

sample	***I*** [µA]	**time** [h]	**length** [µm]	**Sb** [at %]	**comments**
S13 I	−180	22	24	85	–
S14 BIII	−140	13	16	75	–
S11 AI	−180	14	8	50	–
S11 AIII	−140	12	12	10	–
S15 AII	−140	6.5	12	70	AAO+SiO_2
S15 AIII	−120	9.5	15	50	AAO+SiO_2
S15 BI	−100	7	12	45	AAO+SiO_2
S15 BII	−100	5	15	45	AAO+SiO_2
S15 AIV	−100	5	15	70	AAO+SiO_2
S15 BIV	−80	18.5	10	30	AAO+SiO_2
S15 BIII	−80	5	10	8	AAO+SiO_2
S17 DII	−80	24	16	15	15 min at 70 V+SiO_2

Table 4.3: Overview of galvanostatic depositions into AAO membranes from BiSb electrolytes on HNO_3 basis.

During galvanostatic depositions the amount of the current is directed to the system and

the potential is regularized to keep the current constant (see sec. 2.1.1). The samples listed in table 4.3 show that with this technique longer wires than by potentiodynamic deposition are achieved, while it is much more laborious to control the antimony content. As the example of the samples S11 AIII and S15 AII show, guiding the same amount of current to the sample does not lead to the same antimony concentration in the wires. Further TEM analysis of galvanostatic deposited wires (see sec. 4.3) reveal that these wires are not suitable for electrical measurements due to the poor crystallinity.

4.2.4 Electrodepositon of BiSb Nanowires on HCl Basis

In addition to the deposition of nanowires from BiSb electrolytes on HNO_3 basis, wires from the electrolytes on HCl basis are investigated. Firstly, thin films are prepared and analyzed (see sec. 3.5.3) to get a sense of the potential range where $Bi_{1-x}Sb_x$ with $x \approx 0.1$ is deposited. Table 4.4 presents an extract of the wires retrieved from electrolytes on HCl basis. Potentiostatic depositions are performed with deposition potentials around −300 mV. SEM-EDX analysis is used to verify whether the antimony content of the wires matches the expected amount of 10 – 15 at % and if a maximum length of 6 µm is exceeded. Since both revisals are positive, pulsed depositions in the same potential range are performed due to the expected enhanced crystallinity of pulsed deposited wires and higher growth density (compare sec. 4.2). The sample **P01 CIV** marked in bold print is resolved successfully and

sample	**electrolyte**	U_{on} [mV]	U_{off} [mV]	**time** [h]	**length** [µm]	**comment**
S15 DIII	HCl-a-BiSb	−350	–	2.5	15	AAO+SiO_2
S18 AIV	HCl-a-BiSb	−300	–	4.5	–	AAO 15 min at 70 V+SiO_2
S18 AIII	HCl-d-BiSb	−300	–	3	20	AAO 15 min at 70 V +SiO_2
S16 DIII	HCl-d-BiSb	−300	–	2.5	–	AAO+SiO_2
S16 DII	HCl-d-BiSb	−300	−210	6	25	AAO+SiO_2
S16 DIII	HCl-d-BiSb	−320	−150	3	–	AAO+SiO_2
P01C IV	**HCl-d-BiSb**	**−300**	**−150**	**5**	**40**	**phosphoric acid AAO**

Table 4.4: Overview of depositions into AAO membranes from BiSb electrolytes on HCl basis.

TEM-EDX investigations (compare sec. 4.3.2) yield that the composition of the wires is in the desired range. Thus, also electrical measurements are performed on these wires (see sec. 5.4).

4.3 Structural Characterization of Single Nanowires

Structural characterization of the nanowires is performed with TEM, at the Technische Universität Hamburg Harburg and by Dr. Pippel from Max Planck Institute Halle. Typically high voltages of 120 kV are used for the analysis of the samples.

4.3.1 TEM of Single Bi Nanowires

The bismuth nanowires presented here are deposited by pulsed electrodeposition from a bismuth electrolyte (compare tab. 4.1) with t_{on} = 10 ms and t_{off} = 50 ms. The deposition potentials were U_{on} = −140 mV and U_{off} = −60 mV respectively. Figure 4.11 (a) shows a

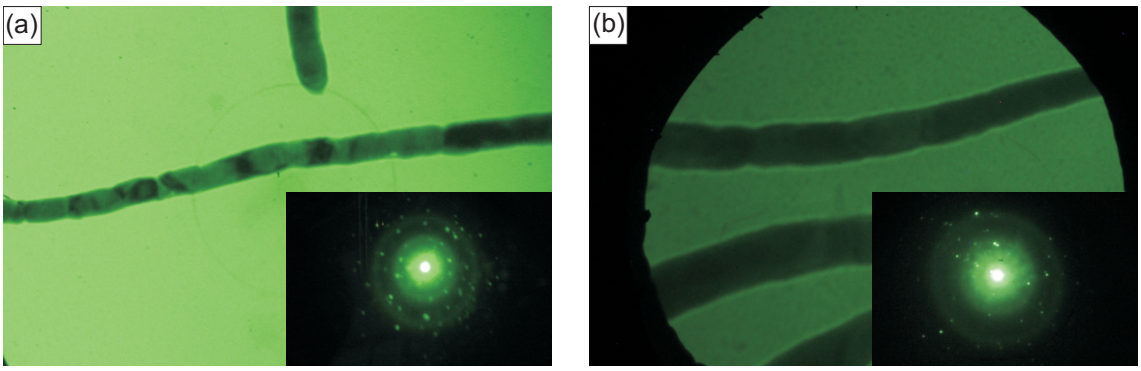

Figure 4.11: (a) TEM image and the corresponding SAED pattern of a Bi nanowire deposited into an oxalic acid AAO membrane. (b) TEM image and the corresponding SAED pattern after annealing of the nanowires.

transmission electron micrograph and the corresponding selective area diffraction pattern (SAED) as inset of the sample S14 CI that has been resolved from oxalic acid alumina membranes. The diameter of the wires is ≈ 60 nm and they have a length of several micrometers. Defined spots in the diffraction pattern suggest that the wires are crystalline. A transmission electron micrograph of the same sample after the annealing for 24 h in N_2 atmosphere at 125 °C is depicted in figure 4.11 (b). As for the Bi thin films no major differences in the micrograph and in diffraction pattern is observable.

Also, bismuth nanowires deposited under similar conditions into nanostructured oxalic acid membranes covered with a silicon oxide shell show comparable results (compare fig. 4.12). In figure 4.12 (a) a transmission electron micrograph of pulsed electrodeposited bismuth nanowires from sample S17 CI (compare again tab. 4.1) with a silicon oxide shell is shown. The corresponding selective area (electron) diffraction pattern given in figure 4.12 (b) indicates that the wires are crystalline as well. Some pronounced refraction spots are de-

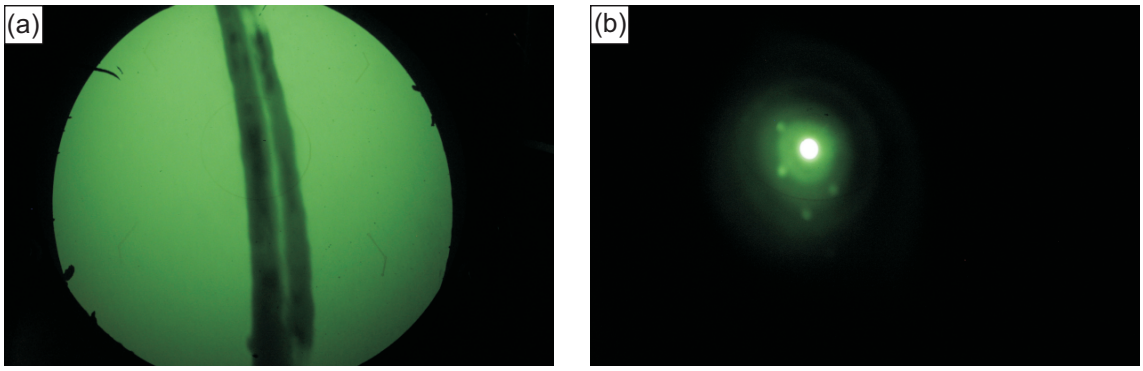

Figure 4.12: (a) TEM image and the corresponding SAED pattern (b) of a Bi nanowire deposited into an oxalic acid AAO membrane with SiO_2 shell.

tected as well as some circles which may indicate amorphous material but might in this case be addressed to the TEM grid itself and additionally to the silicon oxide shell.

Exemplary results of a nanowire from the batch P01 CIII (see tab. 4.4) with a diameter of 200 nm are presented in figure 4.13. The pink circles in figure 4.13 (a) indicate the spots where the refraction images are taken. More diffraction patterns are taken between the encircled points, proving that the wire is single crystalline over a length of > 2.5 µm. Still the wires consist of grains, as images of higher magnification prove. Figure 4.13 (b) gives a closer image of this wire, the darker areas mark grain boundaries, indicating a grain size between half the diameter and multiple diameters. The on-growth at the wires are most likely remnants from the AAO membrane. TEM-EDX investigations shows that they consist of phosphorus and oxygen. Furthermore the energy dispersive X-ray analysis has reinforced the claim that the wires consist of pure bismuth.
A high resolution transmission electron microscopy (HR-TEM) image of the electrodeposited bismuth nanowire is given in fig. 4.14 (a). At the edge of the nanowire a thin bismuth oxide (Bi_2O_3) shell with a thickness of 5–10 nm is observable. The bismuth oxide shell is very robust and makes contacting of single bismuth nanowires challenging (see sec. 5.1 [Cro02]). The indexed SAED pattern in fig. 4.14 (b) shows that the long axis of the wire is textured along the (110) direction.
The crystallographic orientation of the wires could be appointed under the assumption of trigonal bismuth with the space group R3m and the lattice constants a = 0.455 nm and c = 1.186 nm. It is found that the texturing along the wire axis always is along the (110) direction or its opposite (-1-10). In principle -(110) crystal faces are closely stacked, which is common for crystal growth due to energy reasons. A (110) texturing along the wire axis of bismuth nanowires has already been found by other groups, using different growth methods

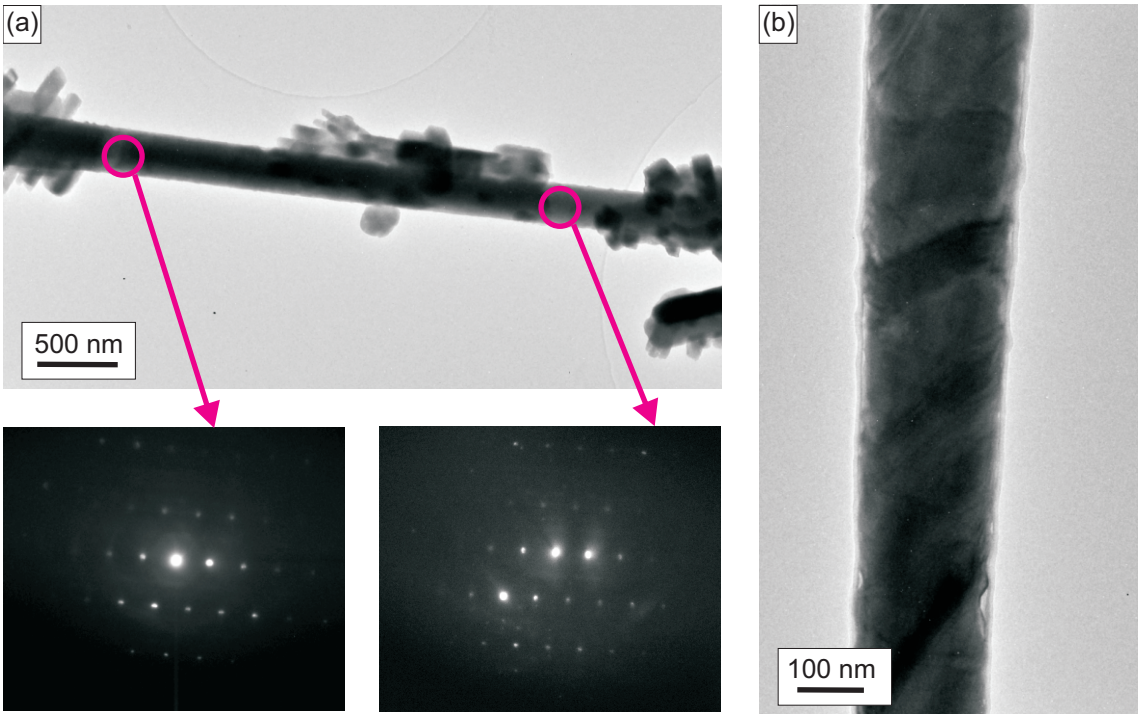

Figure 4.13: (a) Transmission electron micrograph of a single bismuth nanowire and the corresponding refraction images. (b) Closer view of a single bismuth nanowire.

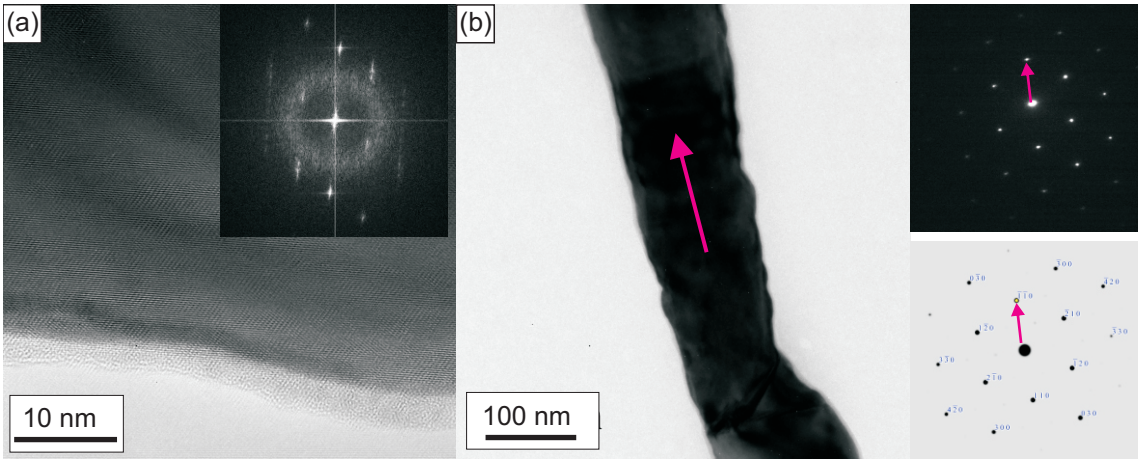

Figure 4.14: (a) HR-TEM image of a single bismuth nanowire with an approx. 5 nm thick bismuth oxide shell. (b) TEM image of a bismuth nanowire and an indexed selected area electron diffraction refraction pattern.

[SHL+09, YZL+08, LLH+10]. Cornelius *et al.* [CBC+05] determined for elelctrodeposited bismuth nanowires depending on the growth parameters either a (110) or a (100) texture of the wire. Depending on the deposition conditions they found the wires deposited potentio-

static to be single crystalline and potentiodynamic deposited wires to have grain boundaries at a distance of about 500 nm in good agreements with the results from the wires presented here.

4.3.2 TEM of Single BiSb Nanowires

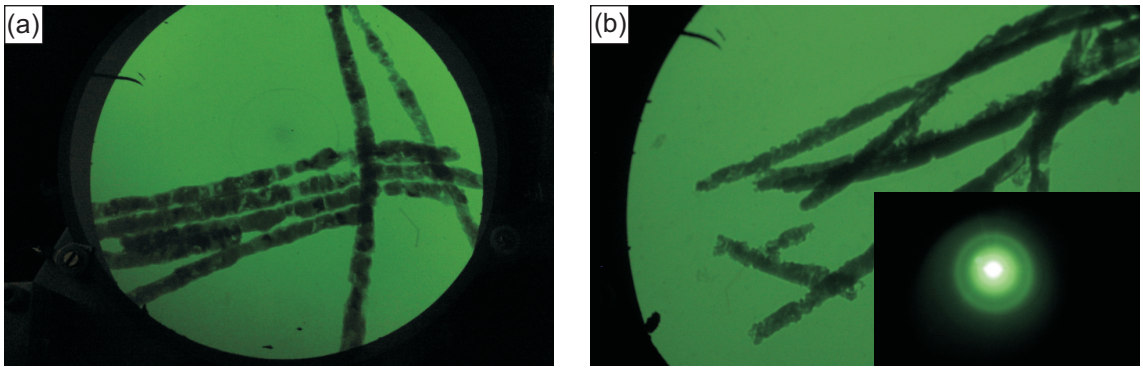

Figure 4.15: TEM images of BiSb nanowires deposited galvanostatic into oxalic acid AAO membranes.

Galvanostatic and potentiondynamic electrodeposited bismuth antimony nanowires are also analyzed by transmission electron microscopy. Two different types of galvanostatic deposited nanowires from BiSb electrolytes on HNO_3 basis are reviewed. Pictures 4.15 (a)+(b) show low resolution transmission electron micrographs of wires from the batches S11 AI and S11 AIII. For details on the deposition parameter see table 4.3. Both kinds exhibit a poor crystallinity and rough surface structure. Hence these wires are not chosen for electrical measurements.
Additionally pulsed deposited bismuth antimony nanowires from the electrolyte HCl-BiSb-d (compare tab. 4.4) are analyzed. The nanowires P01 CIV are prepared by pulsed electrodeposition with on/off deposition potentials of −300 mV and −150 mV subsequently and pulse lengths of t_{on} = 10 ms and t_{off} = 50 ms. A phosphoric acid membrane is used as a template. Coming from the experience with electrodeposited thin films from this electrolyte (compare sec. 3.5.3) an antimony content of ~ 10 at % is expected for the wires. This is also verified by EDX measurements. The ratio of Bi:Sb is determined to 92 : 8 at %. As for the bismuth nanowires, some contamination with nanoparticles is observable on the wires. These nanoparticles contain phosphorous and oxygen and can be identified as residuals from the phosphoric acid membrane.

The transmission electron micrographs shown in figure 4.16 (a)+(b) and the corresponding selective area electron diffraction patterns (spaces marked by red circles) prove that also

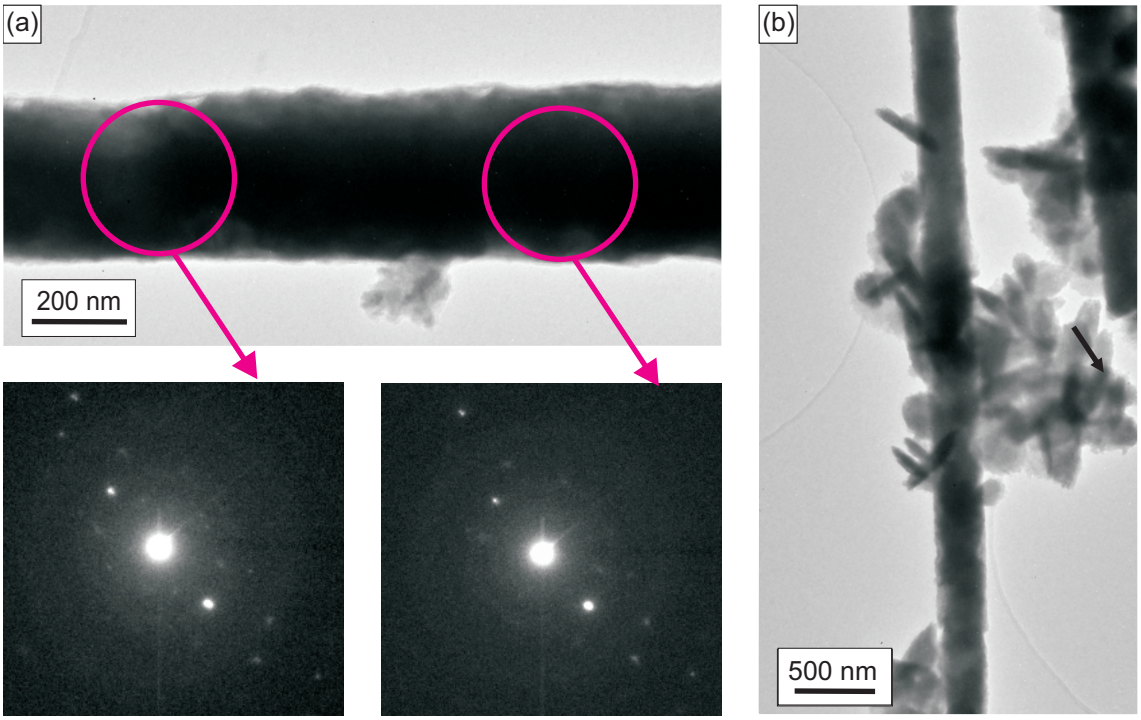

Figure 4.16: (a) Transmission electron micrograph of a single bismuth antimony nanowire and the corresponding refraction images. (b) Closer view of a single bismuth antimony nanowire. The on-growth on the wire is left over from the phosphoric acid membrane.

the bismuth antimony nanowires are single crystalline. The wires are surrounded with a native oxide layer, which has to be removed for contacting single wires, as it is described in the following section.

It was not possible to determine the crystalline direction for the BiSb nanowires for several reasons. Due to the high atomic mass of bismuth in combination with the large diameter of the bismuth antimony nanowires of about $d = 280 \pm 50$ nm a full set of refraction images was not achievable. As for pure bismuth nanowires the (110) direction is a preferred growth direction also for bismuth antimony nanowires [PMGK+03, DZH+06] and since the growth conditions have been similar, the chances are considerable that the here presented nanowires are oriented along the (110) direction as well.

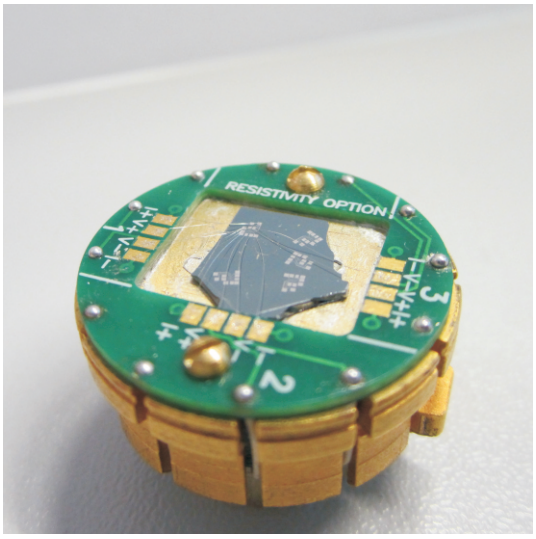

5 Transport Characterization of Single Nanowires

Temperature dependent measurements on single nanowires are fundamental to get the absolute values of the resistivity ρ, SEEBECK coefficient S and conductivity σ. Prior to the electrical characterization a suitable contacting process for the single nanowires with native oxide shell is developed. Drops from the nanowires diluted in DI-water are spread and evaporated on substrates. With a proper two layer resist system, laser lithography, sputter cleaning and Ti/Pt OHMic contacts are formed on the wires. Pure bismuth and bismuth antimony nanowires, deposited under different conditions and into different kind of membranes, are reviewed in this chapter. Temperature dependent transport measurements and SEEBECK measurements are presented of bismuth and bismuth antimony nanowires.

5.1 Fabrication of Ohmic Contacts to Single Nanowires

One bottle neck of this work is to design proper Ohmic contacts to single bismuth and bismuth antimony nanowires. Especially the fabrication of Ohmic contacts to bismuth nanowires is challenging due to a hard bismuth oxide shell surrounding the wires. Thus, it has been more common to characterize arrays or nanowires embedded in single pore membranes. The principle of the measurements is always similar. Metallic drops or stripes are fabricated on both sides of a membrane thus the wires which go through the whole length are contacted. The direction of the current is along the long axis of the wires. Various kind of sample preparation techniques are described in the literature, such as AAO membranes filled by electrodeposition [LCS98], the combination of AAO membranes and a pressure injunction vapor phase technique [HTL+00] and other type of membranes like ion track etched membranes [KWC+09], polycarbonate membranes [LCSYZ98a, TKCM08] or porous Al-Si films [FD08] are used to achieve arrays of bismuth nanowires with diameter ranging from a few nanometer to some micrometer. Such measurements can only exhibit relative values of the resistance since the exact number of contacted wires can not be determined.
Hence, single pore membranes have been used to performe measurements on single wires [CTMNK06, MCC+04] still, due to the two-probe measurement technique a contribution of the contact resistance has to be taken into account. To achieve real four-point measurements on a single bismuth nanowire, complex contacting methods are described in the literature. In general several lithography steps combined with focused ion beam (FIB) [CLR+02b, CLR+02a] or argon sputtering [LLH+10, SHKL09] before the in-situ deposition of the contact materials are required. Already in 1980 Gurvitch [Gur80] designed Ohmic contacts to single bismuth nanowires by using HF (hydrofluoric acid) dip before the deposition of copper and gold. One of the latest technique is described in [TGG+12] where, with a combination of lithography, metal deposition, etching and transfer techniques a surface damages of the wires during the contacting process is prevented. Nevertheless a pre-treatment of the wires is necessary to remove the oxide shell from its surface at the contact points.

Different approaches have been tested within this thesis, until a method for the design of proper Ohmic contacts to single wires is found. A droplet of a diluted nanowire solution is spread on a (100) Si wafer with a 200 nm thick insulating SiO_2 layer. Afterwards the substrate is covered with a two layer system of optical resists for lithography consisting of *LOR 3B* from *Micro Chem* and the positive resist *ma-P 1205* from *micro resist technology*. First attempts on contacting of single wires are done using UV light and a four-contact shadow mask. Afterwards, by using a commercially available laserwriter *μPG 101* system from *Heidelberg Instruments* two different contact designs are realized, one for magnetoresistance measurements

lithograpy	pre-treatment	contacts	post-treatment	comments
UV-light	–	Cr+Au	–	re-oxidation
UV-light	2 – 8 min CHF_3 etching	Cr+Au	–	re-oxidation
UV-light	HCl dip	Cr+Au	–	re-oxidation
UV-light	HCl dip	Cr+Au	6 h annealing in Ar-atmosphere	re-oxidation
laser	20 min Argon sputter clean	Al+Au	–	too long sputter cleaning, the wires has been removed
laser	10 min sputter clean	Al+Au	–	suitable method
laser	5 min sputter clean	Ti+Pt	–	no complete removal of the oxide
laser	**10** min **sputter clean**	**Ti+Pt**	**–**	**standard process**

Table 5.1: Overview of different contacting approaches that are tested for contacting single wires.

on single wires, (compare fig. 5.5) and one for Seebeck measurements (compare fig. 5.6). A *Cressington 308R* sputter machine is used to form the macroscopic contacts consisting of chromium as an adhesion layer and diffusion barrier to the platinum layer. Since none of the contacts works, different pre-treatments are used to remove the oxide from the nanowires. Removing the Bi_2O_3 with CHF_3 by reactive ion etching (RIE) for several sets of minutes is tried. Furthermore, some of the samples are treated by wet chemical etching with a HCl or aqua regia dip. However none of these approaches lead to proper Ohmic contacts to the wires. Since the samples have air contact before the deposition of the contact material a new oxide layer is formed. Also some post-annealing of the contacts in argon atmosphere at 200 °C for > 15 h shows only minor enhancement of the contacts.
Finally, with the *CRC-600* sputter system from *TORR International INC*, a system is accessible that include the possibilities to execute a sputter process with argon ions and the in situ sputtering of metals. Hence the oxide shell around the wires can be removed and the contact material can be sputtered onto the wires without re-oxidation in air. The clearance of the surface from the oxide is called sputter-cleaning and it is carried out with an argon flux of 15 sscm and a power of 20 W. Afterwards, as adhesion layer, titanium is sputtered with a power of 80 W before platinum as contact material is sputtered onto the samples with a power of 25 W. Details of this process can be found in appendix A.4 and in [Glu11].
An overview on different contact approaches that are tested during this work is summarized in table 5.1. Using this technique various nanowires are contacted. It is found that the

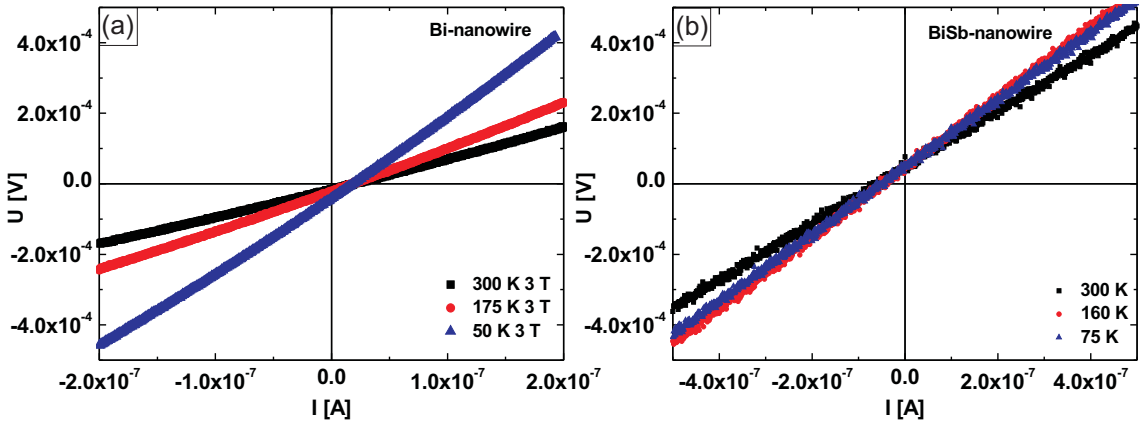

Figure 5.1: (a) I-V characteristics of a Bi nanowire (d = 140 nm) at different temperatures. (b) I-V characteristics of a BiSb nanowire at different temperatures.

same parameter are suitable for bismuth antimony nanowires with an higher success rate. In the year 2002 Cronin [Cro02] also studied intensively the contacting of single bismuth nanowires with different approaches such as e-beam lithography, photolithography and UV lithography in combination with different techniques to remove the oxide from the nanowire shell like HF dip and focused ion beam. The finding was that a non-linear I-V characteristic indicates that the oxide layer is not removed completely. Figure 5.1 (a) and (b) show typical I-V characteristics of a bismuth and bismuth antimony nanowire at different temperatures. Both kind of wires have sufficiently linear I-V characteristics, which leads to the conclusion that proper Ohmic contacts are achieved with this method.

Furthermore, the scheme 5.2 and 5.3 give an outline of the different steps of the contacting process. It starts with nanowires laying randomly on the substrate surface (I). The whole substrate is coated with a two layer photo resist system. Contact masks on single wires are exposed using a *µPG 101* laser writer system with a power of 60 % at 15 mW (II)+(III). Subsequent development of the exposed photo resist prepares the structures for deposition of the contact material (IV). A sputter cleaning process using argon ions is performed to remove the oxide shell on top of the wires (V) prior to the sputter deposition of the contact material (VI). The lift-off process leaves the contacted single wires on the substrate (VII)+(VIII).

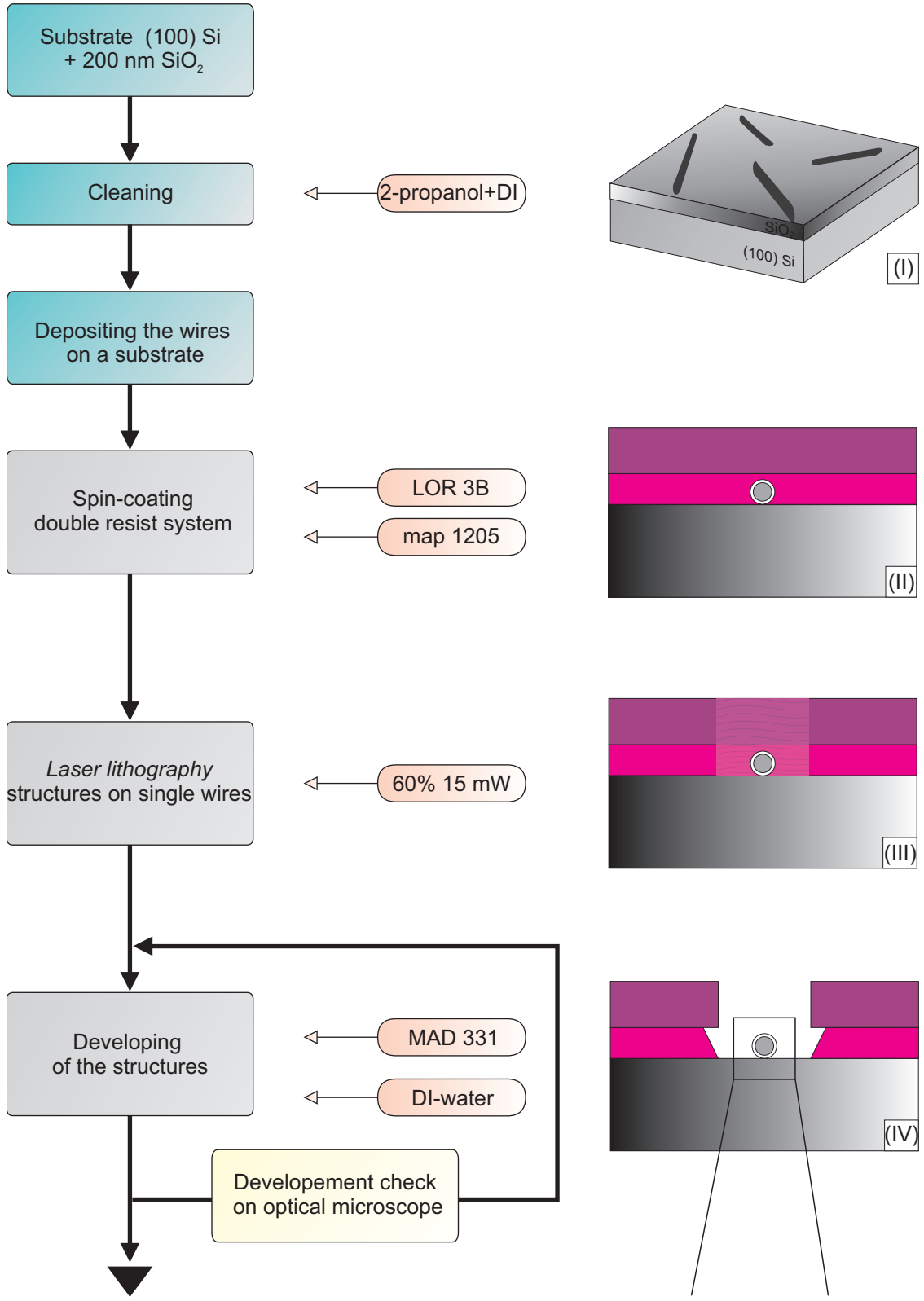

Figure 5.2: Scheme of the lithography steps for contacting nanowires.

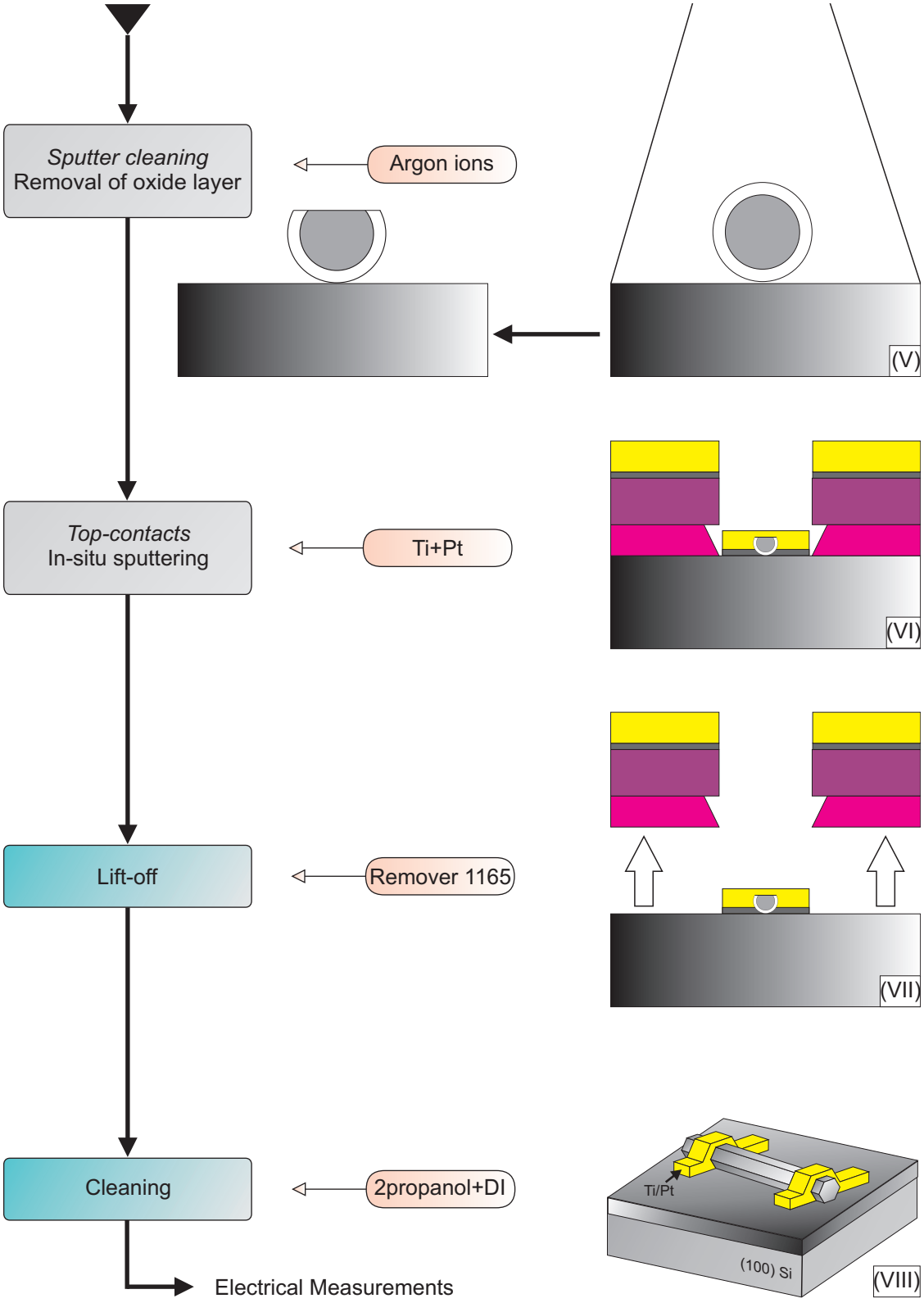

Figure 5.3: Scheme of the lithography steps for contacting nanowires, continued.

5.2 Electrical Characterization of Single Nanowires

For electrical characterization of single nanowires two measurement setups from *Quantum Design* are available. The *Versalab* measurement system depicted in figure 5.4 (a) and the *Dynacool PPSM* which is shown in figure 5.4 (c). Both systems contain a sample holder with twelve bond pads (compare figure 5.4 (b)) evenly distributed to three channels. Each channel can be controlled by the electrical transport option (ETO) of the measurement systems. They are capable of applying a sinusoidal excitation current of several mA to the system, which is much more than is needed for the measurements of nanostructures. To avoid cross-talk between the channels, a different frequency is used for each. The basic measurement routines of both are similar and are described in the following. The *Versalab* is suitable for measurements in a temperature range of 50 – 400 K and a magnetic field up to ±3 T, whereas the *Dynacool* opens the opportunity to cool the samples down to 1.8 K and to apply a magnetic field up to ±9 T. For both systems the measurements take place under helium atmosphere.

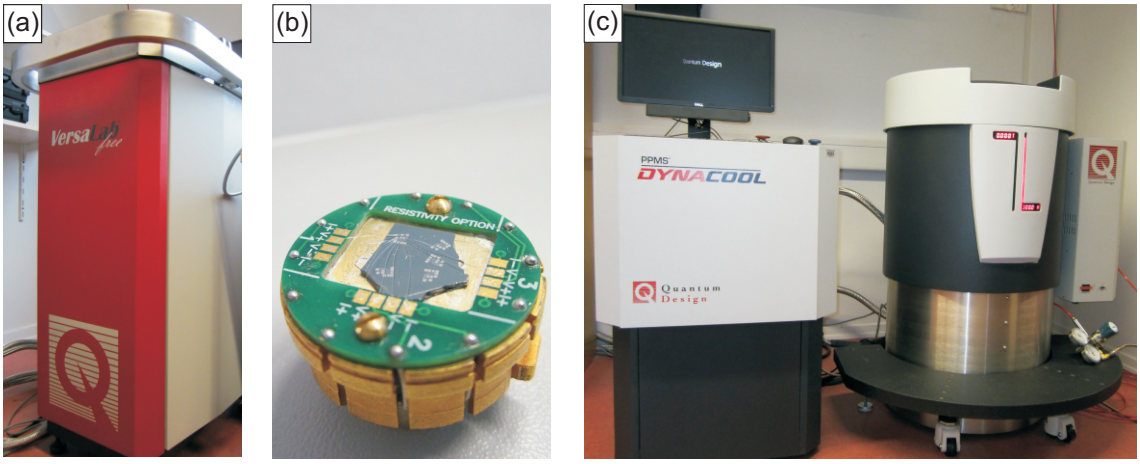

Figure 5.4: (a) *Versalab* measurement system from *Quantum Design*. (b) Picture of the sample holder with twelve bond-pads, suitable for both measurement systems. (c) *Dynacool* measurement system from *Quantum Design*.

5.2.1 Magnetoresistance Measurement

The magnetoresistance (MR) effect that is observed in bismuth and bismuth antimony nanowires is the so called ordinary magnetoresistance (OMR), caused by the LORENTZ force **F** which changes the trajectory of charge carriers in a magnetic field. The LORENTZ force is given by

the equation:

$$\mathbf{F} = q \cdot (\mathbf{E} + \mathbf{v} \times \mathbf{B}) \tag{5.1}$$

with the electrical field **E**, the magnetic field **B** and **v** the velocity of the carriers. The general definition of the magnetoresistance is:

$$MR\,[\%] = \frac{\Delta\rho}{\rho_0}\,[\%] = \frac{R(B) - R(0)}{R(0)} \cdot 100 \tag{5.2}$$

with R(B) and $R(0)$ being the resistance with and without applied magnetic field. One has to distinguish between the transverse magnetoresistance (TMR) and the longitudinal magnetoresistance (LMR). Those denominate the direction of the magnetic field with respect to direction of the electrical current. The TMR is measured with the magnetic field applied perpendicular to the current and the LMR is determined by measurements with the electrical and magnetic field lines pointing in the same direction, with the TMR effect always being higher than the LMR effect. The major influencing factor in the magnitude of the MR effect is $\omega_c \cdot \tau$ with the relaxation time τ, the cyclotron frequency $\omega_c = \frac{eB}{m^* c}$, and the effective mass m^*. To observe high MR effects the requirements on a material are a long relaxation time, in other words a long mean free path and a small effective mass. Bismuth combines all these properties and very large magnetoresistance effects have been observed in bismuth single crystals and polycrystalline material [VSS+00, TB06] for thin films [BLJ+00] as well as for nanowires [MSP+10].

Magnetoresistance measurements are performed on bismuth and on bismuth antimony

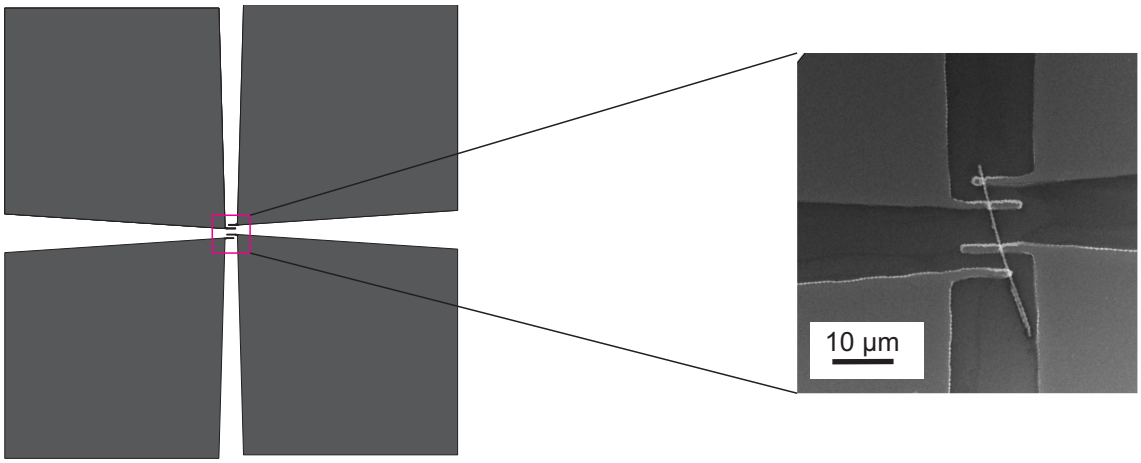

Figure 5.5: Scheme (left side) and SEM image of the four point measurement the magnetic field points in z-direction during the measurements.

single nanowires using a four-point contact design, presented in figure 5.5. For the measurements a sinusoidal excitation current up to 1 µA with typical frequencies of 6.1 Hz and 9.1 Hz for using channel one or two, respectively, is applied through the outer two contact pads and the potential is measured between the inner contacts. The typical distance between the inner two contact fingers is 6 µm. The magnetic field points perpendicular to the substrates and to the wire axis, thus the transverse magnetoresistance is measured.
The measurement routines are performed with the *Versalab* measurement system. First the measurements from 300 – 50 K in 25 K steps are carried out and afterwards the same measurements are repeated up to 400 K. The field sweeps are carried with a sweep rate of 0.5 mTs^{-1} starting at zero field, run up to ±2 T and back to zero field.

5.2.2 Seebeck Measurement Setup

For measurements of the SEEBECK coefficient S the setup shown in figure 5.6 is used. The wires are contacted by two quasi four-point contacts with a distance of 8 µm which serve as thermometers. A heater loop (contacts 9 & 10) is positioned close to one wire end to realize a temperature gradient between the thermometers. By applying a current of a few mA up to a maximum of 10 mA, on this contact, JOULE heating generates a temperature gradient of about $\Delta T \approx 0.5$ K along the wire axis. For different heating currents the thermovoltage

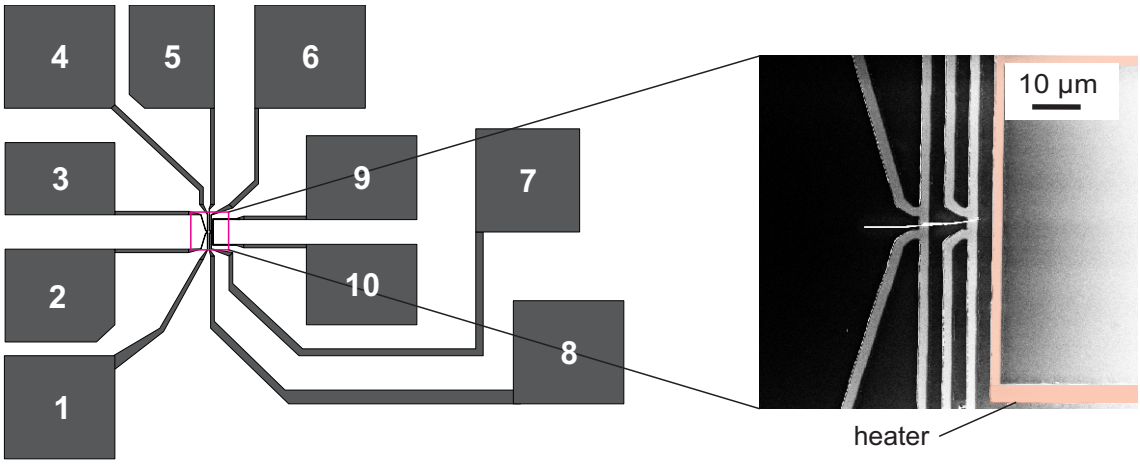

Figure 5.6: Scheme (left side) and SEM image (right side) of the SEEBECK structure for single wire measurements.

U_{thermo} is measured along the wire via the contacts 1 & 8. In order to prevent additional JOULE heating an alternating current (AC) of 10 µA is applied to the contacts (pads 1 & 4 and 5 & 8) to measure the resistance R of the thermometer via contacts 2 & 3 and 6 & 7. Figure 5.7 (a) shows exemplary calibration curves for the two thermometers. A linear fit

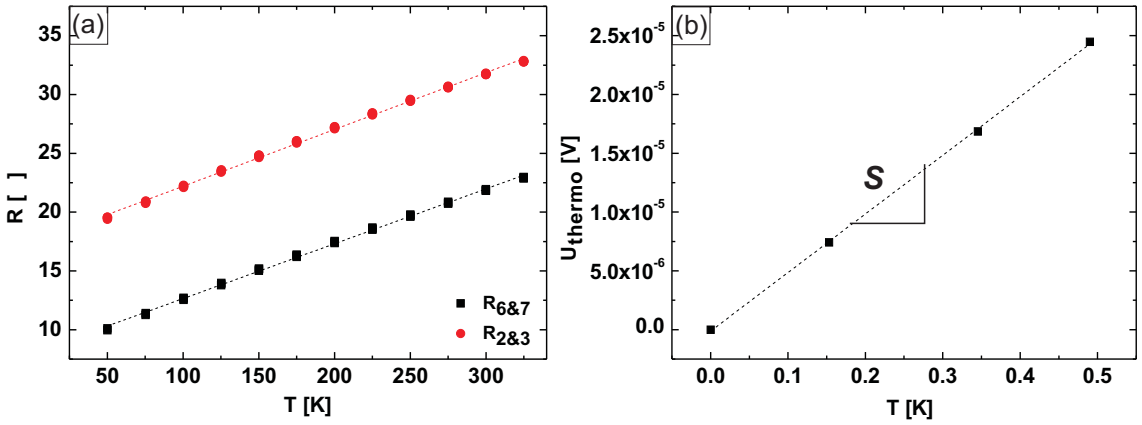

Figure 5.7: (a) Exemplary calibration curve of the two thermometers of a SEEBECK structure. (b) Thermovoltage measured at different heating currents, versus the temperature difference of the thermometers. The data points are fitted linear and the slope gives the SEEBECK coefficient.

between the data points allows to determine the temperatures T_{hot} ($R_{6\&7}$) and T_{cold} ($R_{2\&3}$) on both wire ends. Thus with the temperature difference ΔT and the measured thermo voltage U_{thermo} the SEEBECK coefficient is then determined by the relation:

$$S = \frac{-U_{\text{thermo}}}{\Delta T} = \frac{-U_{\text{thermo}}}{T_{\text{hot}} - T_{\text{cold}}} \tag{5.3}$$

The SEEBECK coefficient has been measured in the *Versalab* downwards from 300 K to 50 K in 25 K steps and upwards with the same step size to 400 K.

5.3 Electrical Characterization of Single Bismuth Nanowires

The resistivity ρ of different nanowires with diameters d of 200 nm, 170 nm and 140 nm is determined at room temperature with a four-point measurement setup (compare fig. 5.5). The nanowires show a resistivity of $\rho = 3.79 \cdot 10^{-6}\,\Omega$m, $\rho = 3.51 \cdot 10^{-6}\,\Omega$m and $\rho = 2.07 \cdot 10^{-6}\,\Omega$m respectively which is in same order of magnitude as the bulk value ($\rho = 1.29 \cdot 10^{-6}\,\Omega$m). According to the MAYADAS-SHATZKES model [MS70, CTMNK06], designed for thin metallic films, the ration $\frac{\rho_{\text{wire}}}{\rho_{\text{bulk}}}$ is directly linked to the grain size of the sample with a higher ratio indicating a smaller grain size.

Graph 5.8 shows the diameter dependence of the resistivity at 300 K. The red dots represents the wires that are measured during this work and the open symbols are comparisons with values obtained by other groups ([MNH+10, NMH+10, MYT+12, Cro01, SKiL+08]). The

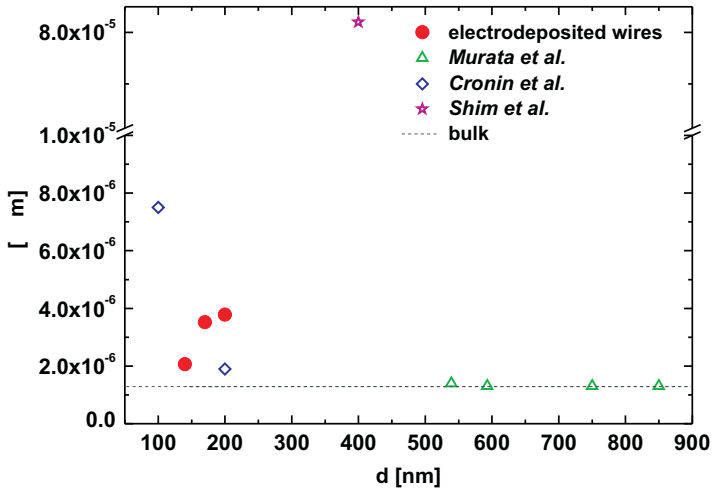

Figure 5.8: (a) Resistivity dependence of the diameter of the bismuth nanowires at 300 K. The dashed line is the bulk value of bismuth. The open symbols are values achieved by other groups.

wires from Murata *et al.* [MNH+10, NMH+10, MYT+12] and Cronin *et al.* [Cro01, Cro02] have been prepared by molten pressure injection into a template system. All wires show a value of ρ very close to the value of bulk bismuth, with exception to the wire of d = 100 nm which shows an increase resistivity. However the wires grown by on-film formation [SKiL+08] which also claim a very good crystallinity have a remarkable higher resistivity already at d = 400 nm. The resistivity of the electrodeposited wires from the present work tends to decrease with decreasing diameter. In summary, non uniform diameter dependence is observable.

Having perfectly single crystalline nanowires one would expect an increase of the resistivity with decreasing diameter due to enlarged surface scattering. For the here presented wires with diameter between roughly 150 – 200 nm no such size effects can be observed. On the contrary the resistivity and the ratio $\frac{\rho_{\text{wire}}}{\rho_{\text{bulk}}}$ with values of 2.94, 2.72 and 1.6 for d = 200 nm, d = 170 nm and d = 140 nm respectively decreases with the diameter. Thus less grain boundary scattering seems to take place and scattering due to size effects is not crucial to the behavior of the resistivity at room temperature. An explanation is that the size of the grains stays the same, but with decreasing diameter the total number of grains, and therefore of grain boundaries, is reduced which reduces the resistivity. Moreover the simultaneous growth of different crystals becomes less probable with reduced diameter and the number of grains is reduced [Coro06]. The obtained results for the resistivity are in good agreement with the transmission electron microscopy results (compare fig. 4.13), which show grain sizes in the magnitude of the wire diameters and the single crystallinity of the grains.

5.3.1 Temperature Dependent Transport Properties of Bi Nanowires

The resistivity $\rho(T)$ as a function of the temperature is an interaction between the carrier concentration $n(T)$ in a material and its mobility $\mu(T)$. Whereas the mobility itself is a combination of different scattering mechanism such as phonon scattering, impurity scattering, grain boundary scattering and sample surface scattering. The interrelation between the carrier concentration an the mobility can be figured by the simple equation:

$$\frac{1}{\rho(T)} = \sigma(T) = e \cdot n(T) \cdot \mu_{\text{total}}(T) \tag{5.4}$$

In bulk bismuth the carrier concentration and the mobility have opposite temperature dependencies. The carrier concentration decreases between 300 K and 4.2 K by a factor of ten whereas the mobility in this region increases by order of 3.5 magnitudes [Har69, MI72]. Thus the temperature coefficient of resistance (TCR) is positive, the resistance decreases with decreasing temperature.
However, in nanostructures one has to take sample boundary and grain boundary scattering mechanism into account which limit the rise of the mobility. Hence, the increase of the mobility with decreasing temperature is less pronounced and the carrier concentration becomes the dominant factor for the slope of the resistance. The temperature dependent resistivity between 50 and 400 K for wires with different diameters and for bulk are shown in the graph 5.9 (a)+(b). The values of the bulk resistivity are calculated with the relation [BM01]:

$$\rho(T)[\Omega\text{m}] = 3.88 \cdot 10^{-9} \cdot T[K] \tag{5.5}$$

All samples below ~ 200 K show an increase of the resistivity with decreasing temperature. In the range between 200 – 400 K the resistivity for the 140 & 170 nm diameter wires decreases slightly whereas the resistivity of the bigger wire d = 200 nm increases as it is in bulk bismuth. Also the slope of the resistivity is roughly the same as for bulk material, as it can be seen comparing the black curve and the blue curve in graph 5.9 (a). A similar behavior of the resistivity is reported by Komnik *et al.* [KBNA71] for bismuth thin films.
Since the early 1960th one can find numerous publication on different temperature and size dependent transport properties of bismuth single crystals [Kao63], bismuth thin films [GKS72] and finally bismuth nanowires [WZS+01] experimentally and theoretical [MvML62]. The found negative, positive and nonmonotonic temperature coefficients of resistance are all attributed to different dimension, direction and crystallinity of the investigated samples. As one of the first Gurvitch [Gur80] presented temperature dependent resistivity mea-

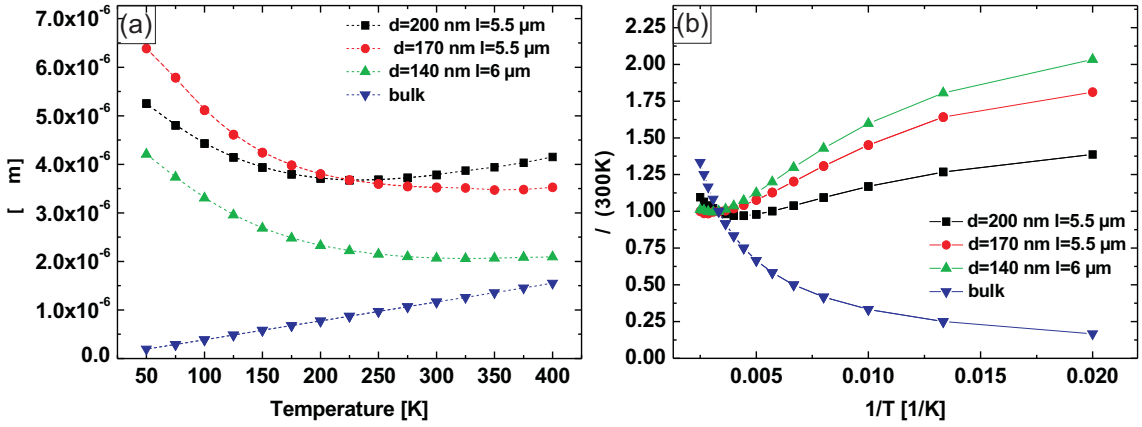

Figure 5.9: (a) Temperature dependent resistivity of bismuth nanowires with various diameters. (b) Normalized resistivity versus the reciprocal temperature of bismuth nanowires and bulk bismuth. The lines are guides to the eye.

surements of single crystal bismuth nanowires with diameter between 180 nm and 2 µm. As in bulk bismuth he found a positive TCR for all samples with the largest values of ρ found for the wires with the thinnest diameter. This is explained by the single crystallinity of the samples and therefore the increased surface scattering being the dominate mechanism.
The increase of the resistivity with decreasing temperature also is observed in several samples such as polycrystalline thin films [YLH+99] and polycrystalline nanowires [HYL+99]. Cornelius *et al.* [CTMNK06] reported on a nonmonotonic behavior of the resistance with the maximum shifting to lower temperatures for samples with decreasing grain size and decreasing diameter. The presented wires are electrodeposited into single pore membranes under different conditions and the measurements took place in the membrane thus the contact resistance has to be considered. Nevertheless, they reported for wires embedded in a membrane, on values of $\frac{\rho_{\text{wire}}}{\rho_{\text{bulk}}}$ of 7.8, 3.8 and 2.8 for different deposition conditions, which is comparable to the ratios found for the here presented nanowires. Heremans *et al.* [HTL+00] observed for single-crystal nanowires both, a negative TCR for bismuth nanowires with diameter below 50 nm and a non monotonic behavior for thicker wires. For the thinner wires they found sample boundary scattering to be dominating over the whole temperature range whereas the other can be divided into two temperature regimes. A regime at low temperatures where scattering at the walls of the wires is the dominant factor and a regime at higher temperatures where phonon scattering determines the resistance.

In bismuth commonly a two band model is used to describe transport phenomena that covers three degenerated electron pockets and one ellipsoidal hole pocket [Har69, XHY+08] (compare fig. 1.2). In this case electrons and holes contribute to the electrical current and

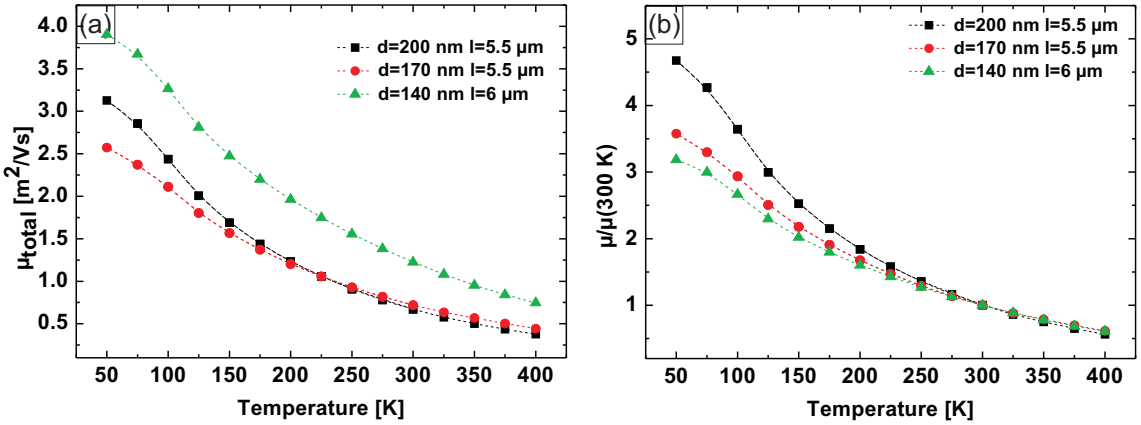

Figure 5.10: (a) From the resistivity data calculated temperature dependent total mobility of bismuth nanowires. (b) Total mobility of the Bi nanowires normalized to the value at 300K. The dashed lines are guides to the eye.

the resistivity is given by:

$$\frac{1}{\rho} = \sigma = e[n_e(T)\mu_e(T) + n_h(T)\mu_h(T)] = en(T)(\mu_e + \mu_h) \tag{5.6}$$

with the electron and hole concentrations $n_e(T)$ and $n_h(T)$ and the corresponding mobilities $\mu_e(T)$ and $\mu_h(T)$. Due to the highly anisotropic Fermi surface of bismuth the mobilities strongly depend on the crystal orientation. But, assuming the same carrier density for all wires like in bulk bismuth one can calculate the total mobility $\mu_{\text{total}} = \mu_e + \mu_h$. For the here presented results, the carrier density values calculated by Michenaud and Issi [MI72] are used. A fit to their values leads to the equation:

$$n(T)[\frac{1}{\text{m}^3}] = 1.433 \cdot 10^{-24} \cdot \exp\left(\frac{T[\text{K}]}{300} - 1.44 \cdot 10^{24}\right) \tag{5.7}$$

The results are given in figure 5.10 (a) with the normalized values given in figure 5.10 (b). All samples show the same temperature dependent behavior. As expected the total mobility increases with decreasing temperature.[1]

Furthermore, they show a change of the slope below approx. 200 K just like the resistivities do. Thus different mechanisms become overriding. Whereas at high temperatures the influence of the mobility and the carrier concentration balance each other out, leading to a constant or only slightly decreasing resistivity.

[1]For our calculations the carrier density at 75 K is assumed to be the same as the from Michenaud and Issi reported value at 77 K and the carrier concentration at 50 K is assumed to be $3.8 \cdot 10^{23}$ m^{-3} which is higher than the value calculated from the fit (see eq. 5.7).

5.3.2 Magnetoresistance of Bi Nanowires

To get more information on the transport properties in bismuth nanowires the MR has been determined. Measurements are performed between 50 – 400 K and in magnetic fields up to ±2 T with the magnetic field perpendicular to the substrate and the long axis of the wire (see section 5.2.1).

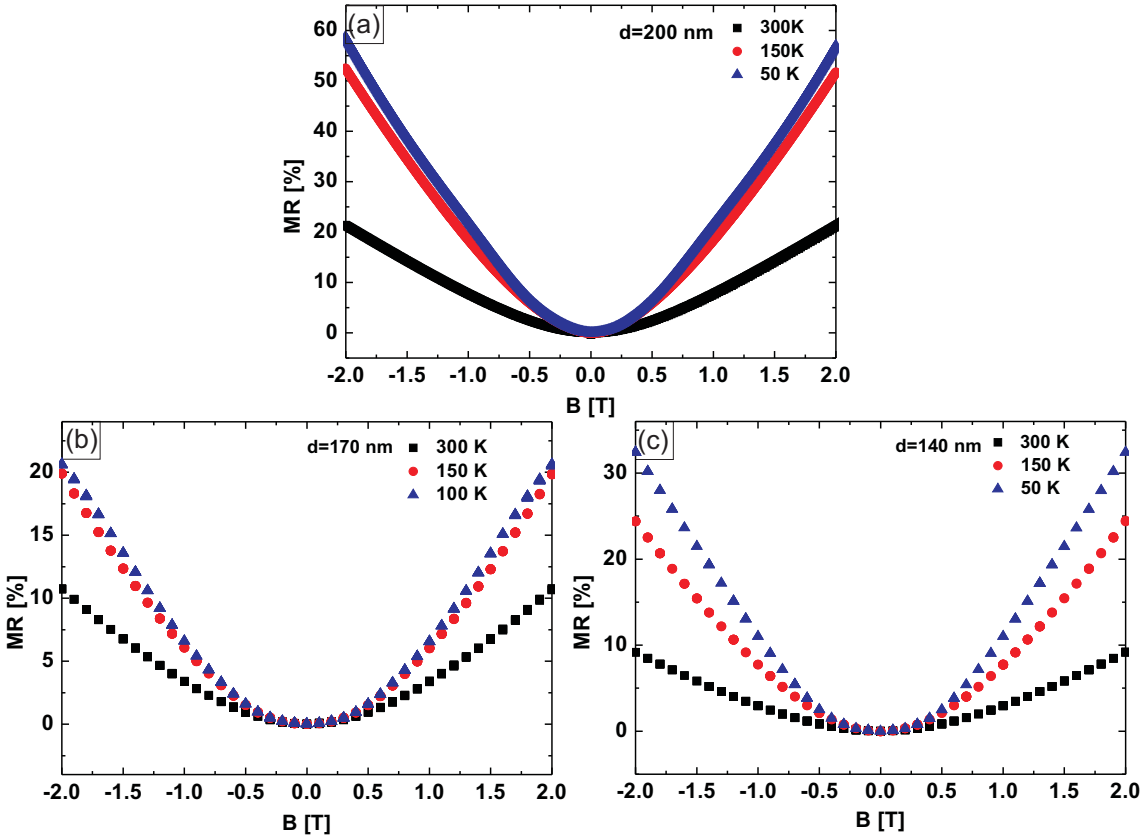

Figure 5.11: (a) Magnetic field dependent magnetoresistance effect of a 200 nm diameter bismuth nanowire at different temperatures. (b) Magnetic field dependent magnetoresistance effect of a 170 nm diameter bismuth nanowire at different temperatures. (c) Magnetic field dependent magnetoresistance effect of a 140 nm diameter bismuth nanowire at different temperatures.

The transverse magnetoresistance TMR effect in a metallic or semiconductive non magnetic nanowire is caused by having more than one kind of carrier. The TMR in a two band model is given by the equation [Smi78]:

$$\frac{\Delta\rho}{\rho_0} = \frac{n_i n_j \mu_i \mu_j (\mu_i + \mu_j)^2}{(n_i \mu_i + n_j \mu_j)^2} \cdot B^2 \tag{5.8}$$

with $\mu_{i,j} = \frac{e\tau_{i,j}}{m_{i,j}}$ being the mobility of the carriers, $\tau_{i,j}$ is the live time and $m^*_{i,j}$ the correspond-

ing effective masses. For the special case that $\mu_i = \mu_j$ equation 5.8 becomes zero, thus no transverse magnetoresistance can be observed in such materials. The group of Searson reported in the late 90th on the magnetoresistance effect in electrodeposited thin films and nanowires. Measurements on electrodeposited thin films revealed values between several hundred percent for polycrystalline material and up to 153000 % at 5 K for single crystalline thin films at low temperatures [YLH+99, YLCS99]. On polycrystalline bismuth nanowire arrays in fields up to 55 T magnetoresistance effects of 600 – 800 % are observed [HYL+99]. Single crystalline wires grown by on-film formation showed an even higher transverse magnetoresistance effect of up to ~ 2500 % at 110 K [SKiL+08, SHL+09]. The graphs 5.11 (a)-(c) show the field dependent magnetoresistance effect of the different wires for temperatures between 50 and 300 K. The here reached values of the magnetoresistance effect at a field of 2 T are with 20 % at 300 K and up to 70 % at 50 K in good agreement with the values found by Liu *et al.* for Bi nanowires consisting of large grains [LCSYZ98b]. Above a critical field the MR effect, respectively the change of the resistivity in a magnetic field should drop down because the cyclotron radius becomes smaller than the diameter of the wire. Then surface scattering is suppressed and the resistance becomes smaller (see sec. 5.4.3). Such effects cannot be found for our wires in fields up to ±2 T.
They all show a quadratic dependency at low fields (B < 0.5 T) according to the relation [SF31, HTL+00]:

$$MR = \frac{R(B,T) - R(0,T)}{R(0,T)} \sim A \cdot B^2 \tag{5.9}$$

with the galvanomagnetic coefficient (magnetoresistance coefficient) A having the unit T^{-2} which is equal to the unit of the squared mobility μ, with $1\,T^{-2} = 1\,m^4V^{-2}s^{-2}$. A is a tensor with eight different components $A_{ij} \geq 0$ that depend on the direction of the current and the magnetic field as well as on the crystal orientation of the sample. Thus it is challenging to determine the single components due to high demands on the crystallinity of the material. The temperature dependent fitting parameter A is shown figure 5.12 (a). All fits are performed on the field dependent magnetoresistance curves in the range of $-0.4\,T < B < 0.4\,T$. The dashed lines are guides to the eye. The direct comparison of the galvanomagnetic coefficient A used to fit the MR at low fields $B < 0.4\,T$ and the magnetoresistance effect at 2 T (fig. 5.12 (a) and (b)) both show the same course. All wires which have both parameters constantly rising with decreasing temperature down to 75 – 125 K. Below that the magnetoresistance effect starts to decrease. In general one would expect an constant increase of the MR effect due to an increase of the mean free path which can be assumed by the constant increase of the absolute mobility given in figure 5.10. But also the galvanomagnetic coefficient A, which is directly linked to the mobilities in a material, shows a decrease at low temperatures. Thus

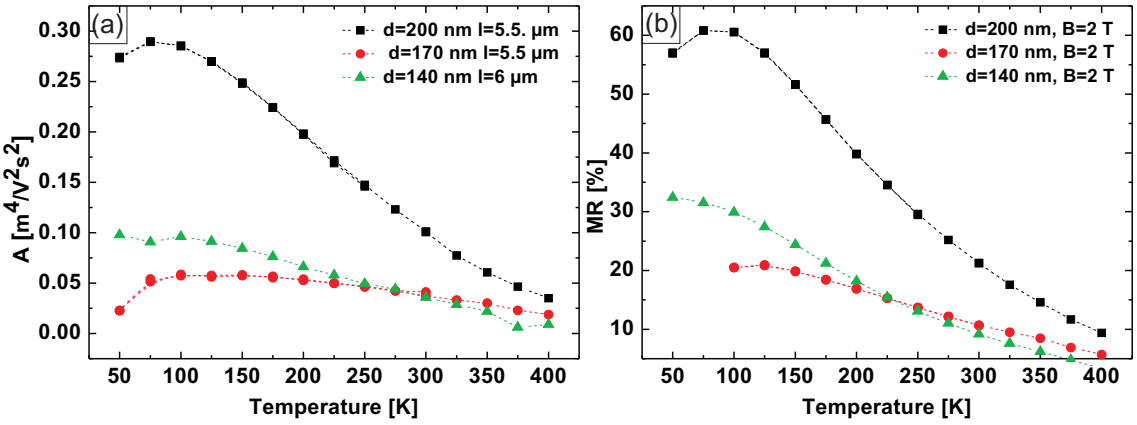

Figure 5.12: (a) Fitting parameter A for the quadratic region of the magnetoresistance for different nanowires. (b) Temperature dependent magnetoresistance effect at 2 T. The dashed lines are guides to the eye.

more information to describe this behavior are needed. Proceeding the assumption from section 5.3.1 that the concentrations of electron and holes in the wires are equal $n_h = n_e = n$, the equation(5.8) simplifies to the following relation:

$$MR = \mu_i \mu_j \cdot B^2 \tag{5.10}$$

together with eq. 5.9 the galvanomagnetic parameter A can then be written as:

$$A = \mu_e \cdot \mu_h \tag{5.11}$$

The equation 5.4 gives the relation:

$$\frac{1}{\rho n(T) e} = \mu_e + \mu_h \tag{5.12}$$

Both relations can be combined to the quadratic equation:

$$0 = \mu_{\mathrm{i,j}}^2 - \frac{1}{\rho n(T) e} + A \tag{5.13}$$

This equation is solved by the the term:

$$\mu_{\mathrm{i,j}} = \frac{1}{2 \cdot e \cdot n(T) \cdot \rho(T)} \pm \sqrt{\frac{1}{4 \cdot e \cdot n(T) \cdot \rho(T) - A}} \tag{5.14}$$

The calculated mobilities $\mu_{i,j}$ of the different nanowires are shown in the graphs 5.13 (a)+(b).

Since in the following SEEBECK measurements the sign of the SEEBECK coefficient is the negative, the higher value of $\mu_{i,j}$ is ascribed to the electrons, identifying them as the dominant carriers. The electron mobility μ_e of all wires rises continuously with dropping temperature whereas the hole mobility μ_h shows an discontinuous temperature dependence. Even though the electron mobilities increases continuously the slope decreases around 100 K indicating a saturation behavior. Together with the decreasing hole mobility with decreasing temperature the depletion of the magnetoresistance effect at low temperatures can be explained. Consequently the rise of the mean free path of carriers in the wires is diminished by the average grain size. If this limit is reached the mean free path, hence the mobility of carriers can not rise further.

The here calculated mobilities at room temperature are comparable to those measured on

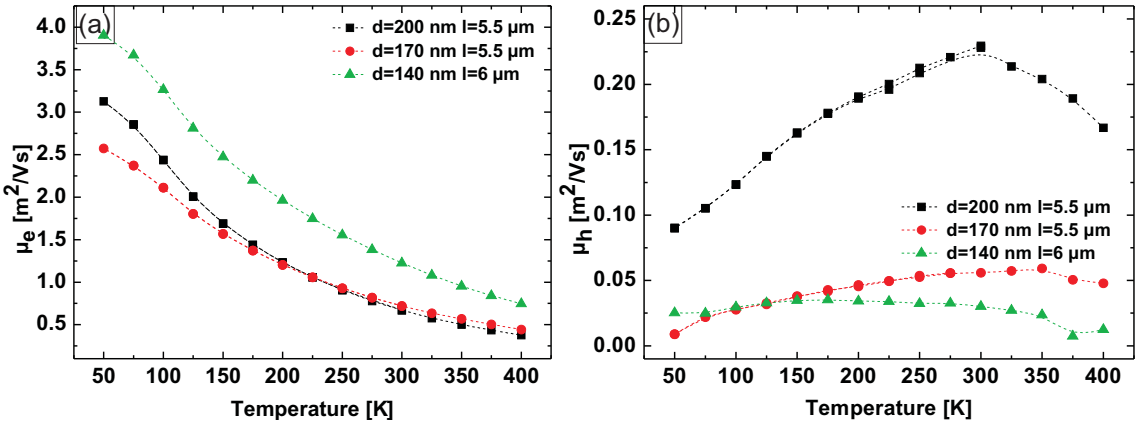

Figure 5.13: (a)Temperature dependence of the electron mobilities of different bismuth nanowires. (b) Temperature dependence of the hole mobilities of different bismuth nanowires. The dashed lines are guides to the eye.

polycrystalline bismuth thin films [dKB83]. Up to now the largest published value on the electron mobility of single bismuth nanowires at room temperature is $\mu_e \approx 7.7\,\mathrm{m^2V^{-1}s^{-1}}$ [SHL+09] which is in the order of carbon nanotubes ($7.9\,\mathrm{m^2V^{-1}s^{-1}}$) [DGCF04]. This value has been calculated with the assumption that the resistivity of the wire is the same as in bulk bismuth. Thus, by making the same assumption for the here presented wire a value of approx. $2\,\mathrm{m^2V^{-1}s^{-1}}$ for the wire with $d = 140$ nm is reached here. Typical values for MBE grown III/V compound nano-whiskers are in the order of a few $1 \cdot 10^{-2}\,\mathrm{m^2V^{-1}s^{-1}}$ [OBP+02, Hei08] which is already large (two orders of magnitude higher) compared to Si nano-whiskers [CDHL00].

5.3.3 Seebeck Coefficient of Bi Nanowires

The SEEBECK coefficient S of a bismuth nanowire with a length of 7.5 µm and a diameter of 210 nm is determined between 50 – 350 K. The room temperature value of $S = -12\,\mu VK^{-1}$ is much lower than the value found for bismuth thin films ($S = -55\,\mu VK$, compare sec. 3.4). For the single bismuth nanowire a maximum of the SEEBECK coefficient $S_{max} = -33\,\mu VK^{-1}$ occurs at 175 T, showing the high anisotropy of bismuth. The resistance of the wire is measured via a two point measurement between the contact pads 3 & 7 of the SEEBECK structure (compare fig. 5.6). At room temperature the resistivity of the wire is $\rho = 3.6 \cdot 10^{-6}\Omega m$ which is very close to the value of the $d = 200$ nm wire presented above. Assuming the same temperature dependence of the resistivity for both wires a maximum power factor of $pf_{max} \approx 250\,\mu WK^{-2}m^{-1}$ at 175 K is calculated.
Bismuth nanowires have a very small thermal band gap ΔE and electrons and holes contribute to the transport and the SEEBECK coefficient. The contribution to S have different signs which leads to a reduced absolute value of the SEEBECK coefficient. With rising temperature the contribution of the electrons and holes to the SEEBECK coefficient equalize and the absolute value of S decreases. Few reports on temperature depending SEEBECK measurements of single bismuth nanowires are available so far (see table 5.2). However with additional consideration of the reports on bismuth thin films and bismuth bulk material, the observed behavior varies widely between the different researches stating the high anisotropy of the material (compare also sec. 1.3). A maximum SEEBECK coefficient at approx. 120 K is reported for Bi thin films [CVW+97]. Investigation of S for different film thickness contains a change in sign depending on the temperature and the thickness of the film. For bulk single

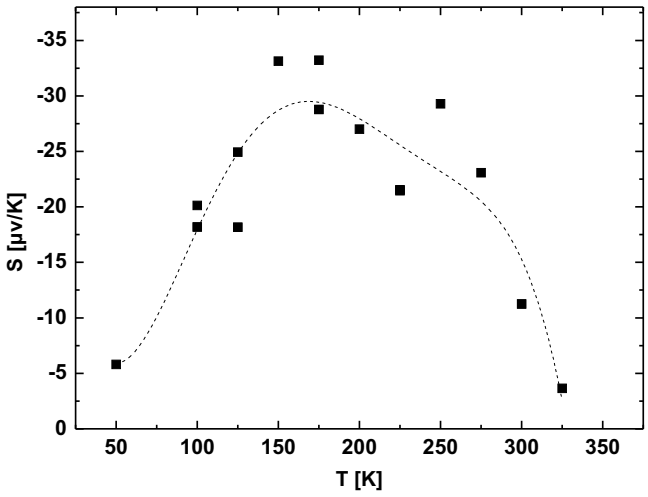

Figure 5.14: Temperature dependence of the SEEBECK coefficient of a single bismuth nanowire. The dashed line is a guide to the eye.

diameter [nm]	$\mathbf{S_{max}}$ [μVK^{-1}]	**comments**	**Ref.**
539, 593 & 850	−57 at 300 K	S decreases with T and becomes positive at 100 K	[MNH+10, MNH+09, NMH+10]
72	−25.2 at 300 K	monotonic decrease with T	[BXH06]
65	−42 at 300 K	nanowire array	[LRC+02a]
100	−18 at 300 K	nanowire array	[Mue12]
200	−33 at 175 K		present work
thin film	−55 at 300 K		present work

Table 5.2: In the literature reported SEEBECK coefficients of bismuth nanowires.

crystals a maximum of the SEEBECK coefficient is found at approx. 125 K measured perpendicular to the three-fold axis [Cha59]. Also for thin films it is found that the position of the maximum SEEBECK effect depends on the direction of the current in respect to the crystal axis [Cho99].

5.4 Electrical Characterization of Single Bismuth Antimony Nanowires

As already mentioned for $Bi_{1-x}Sb_x$ thin films and $Bi_{1-x}Sb_x$ bulk alloys the properties are very sensitive to slight changes of the antimony concentration in the range between $0 < x < 0.15$. The analysis of single BiSb nanowires with TEM-EDX resulted in a Bi:Sb ration of 92 : 8 at % (compare sec. 4.3.2), what means an antimony concentration in the highly interesting region. Since it is uncertain if this value is accurate for all wires, the properties of the electrical measured wires might vary between the different samples. Also the influence of the different diameter between the measured wires might be taken into account. Hence it is hardly suprising that nearly each wire shows slightly different temperature and magnetoresistance behavior. The details will be discussed in the next sections. Additionally a comparison of as-prepared as well as annealed nanowires is performed. The temper (or annealing) process of the wires is carried out prior to the deposition of the metallic contacts, under nitrogen atmosphere at 180 °C for ~ 15 h. Test gone ahead with already contacted and characterized BiSb nanowires demonstrated that the contacts are effected during the annealing process and no measurements could be performed afterwards. All investigated bismuth antimony nanowires originate from the same phosphoric acid made AAO. Thus with exception of an annealing process they all experienced the same treatments. The values of the resistivity ρ of

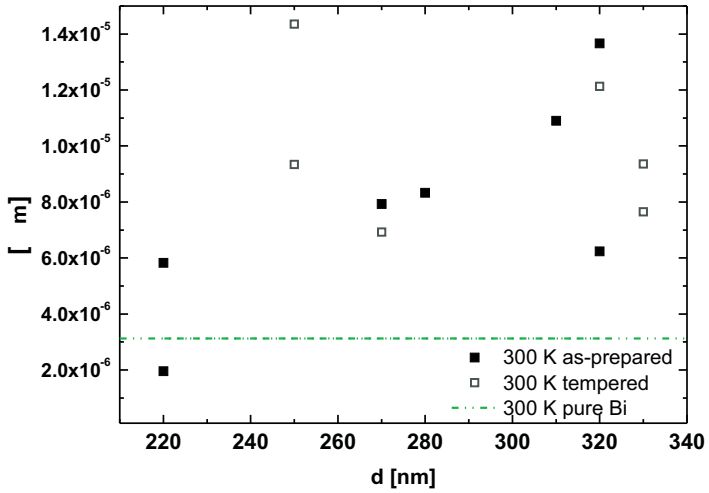

Figure 5.15: Diameter dependence of the resistivity of as-prepared (black squares) and tempered (open black squares) BiSb nanowires at 300 K. The dashed green line is the resistivity value of pure bulk bimsuth.

BiSb nanowires at room temperature plotted versus the diameter are given in the graphs 5.15. Filled black squares resemble the values of the as-prepared wires and the open squares resemble the values of the tempered wires. For comparison the average value of the presented pure bismuth nanowires is shown via the dashed line (green).
As already observed for pure bismuth nanowires (compare sec. 5.3) no diameter dependence can be identified neither for the as-prepared nor for the annealed wires.

5.4.1 Temperature Dependent Transport Properties of BiSb Nanowires

The thermoelectric and galvanomagnetic properties of bulk BiSb alloys have been studied extensively, predominating for single crystalline material [ZBBK00, LDP+95] but also some reports for polycrystalline alloys [YT02, KNK+04] are available. As already mentioned in the section 3.5.3 about electrodeposited thin films, the alloys with low antimony concentration (< 20 at %) show the most exciting behavior.
The temperature dependent electrical resistivity of several BiSb nanowires is shown in figure 5.16 (a)+(b). The different wires exhibit mixed slopes with negative temperature coefficient of resistance at high temperatures (roughly $T < 175$ K) and for some samples a positive TCR below this value. The resistivity of the wires with diameters of 270 and 280 nm increases with decreasing temperature and show a change of the slope around 175 K. The resistivity of the wires with the diameter $d = 320$ nm and $d = 310$ nm have temperature maxima at 175 K

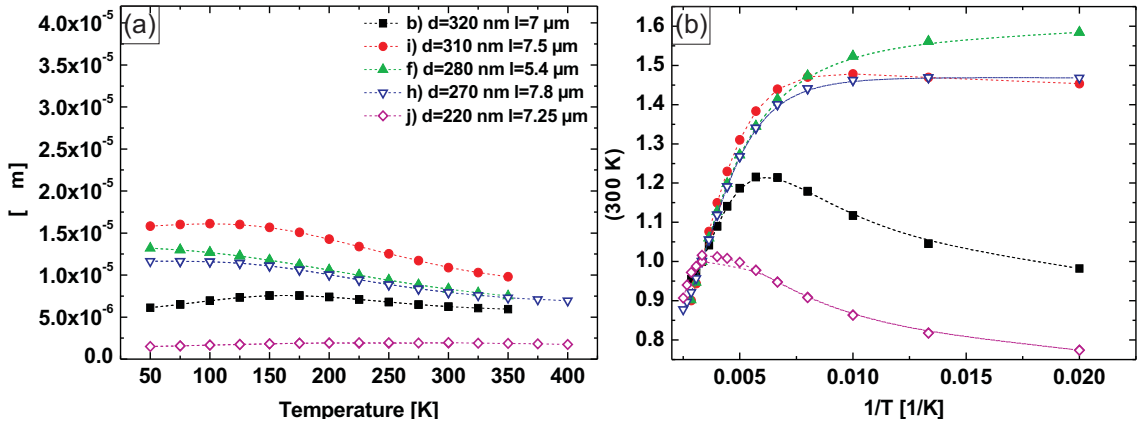

Figure 5.16: (a) Absolute resistivity as a function of temperature for as-prepared BiSb nanowires with different diameters. (b) Normalized resistivity as a function of $1/T$ for different as-prepared BiSb nanowires. The dashed lines are guides to the eye.

and 150 K and the resistivity of the d = 220 nm wires starts to decrease again at even higher temperature. The different slopes of the resistivity is also expressed by plotting ρ against the reciprocal temperature (compare graph 5.16).
In comparison, all wires that have been annealed show semiconducting behavior with a negative TCR over the whole temperature range (compare figure 5.17 (a)+(b)). Under the assumption that ρ(T) follows an exponential law the thermal band gap ΔE can be estimated by the relation:

$$\rho \sim \rho_0 exp\left(\frac{\Delta E}{2k_B T}\right) \tag{5.15}$$

where ρ_0 is a constant, k_B is the Boltzmann constant and ΔE the band gap. Note that the thermal band gap includes both, thermal activation of carriers via the direct band gap E_g and the transition via indirect band gaps. In this case $\log(\rho)$ plotted versus $1/T$ is fitted linear in the temperature range of 350 – 125 K and the band gap is calculated using the slope of this fit. The achieved value of the band gap for all annealed wires is ΔE = 17 ± 3 meV. For comparison fig. 5.18 gives the values of the energy gap of $Bi_{1-x}Sb_x$ depending on the antimony concentration x that have been determined by other groups [Jai59, LCM+96, LDC+98, MDM+12, MPH90, CDW+99]. The temperature ranges which are given in the legend of graph 5.18 correspond to the temperature ranges the data have been fitted exponentially. In the case of Cho the value of the band gap is calculated for T = 0 K [CDW+99]. As one of the first Jain [Jai59] calculated the band gaps for different single crystal bulk $Bi_{1-x}Sb_x$ alloys from the temperature dependent resistivity assuming an exponential law (see equation 5.15). The largest band gap E_g Jain found is around 14 meV at a composition of 12 at %

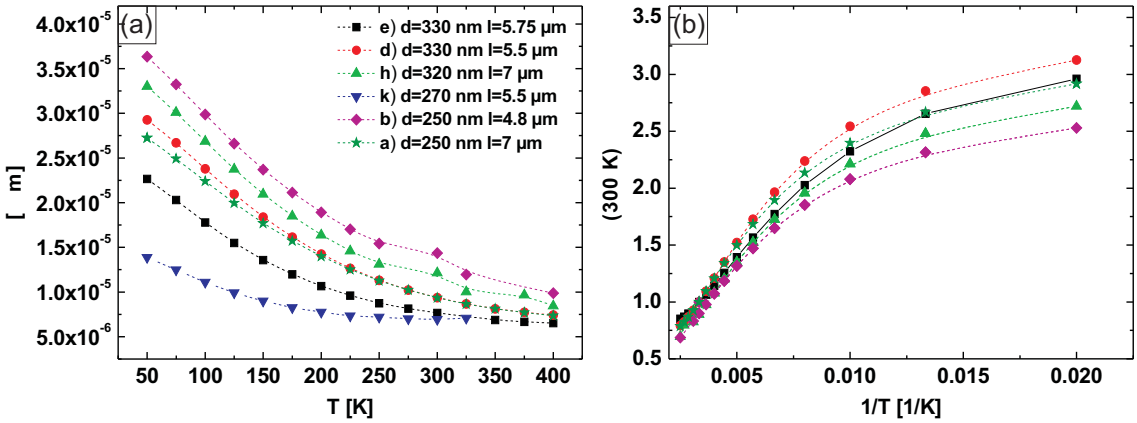

Figure 5.17: (a) Absolute resistivity as a function of temperature for tempered BiSb nanowires with different diameters. (b) Normalized resistivity as a function of $1/T$ for the tempered BiSb nanowires. The dashed lines are guides to the eye.

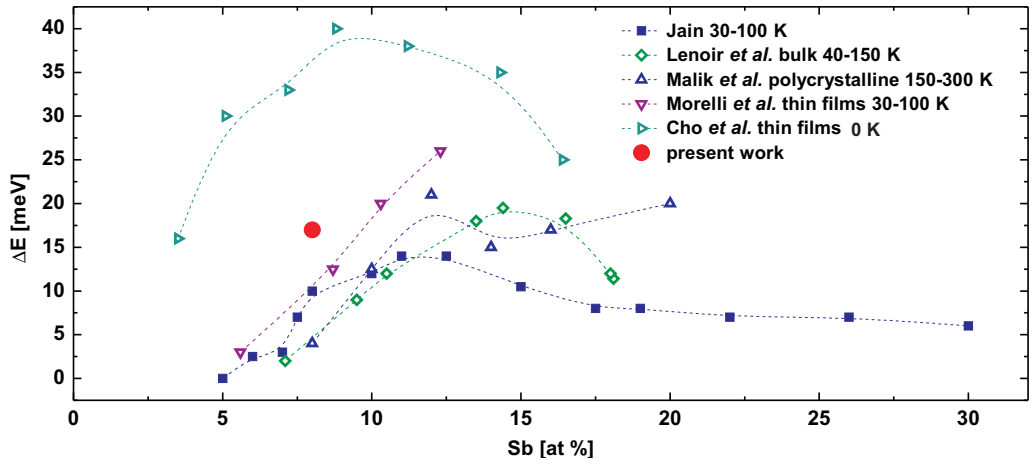

Figure 5.18: Experimental evaluated band gaps of BiSb alloys depending on the antimony concentration.

Sb. In the next years investigations of Yim and Amith , Brown *et al.* and Dugue verified that the maximum band gap of ~ 20 meV occurs at a antimony concentration between 12 – 15 at % [YA72, BH64, BS64, Dug65].

Malik *et al.* reported on the properties of polycrystalline $Bi_{1-x}Sb_x$ alloys. They found the temperature dependent resistivity to increase with rising Sb content and the maximum band gap of 21 meV for the alloy with 12 at % Sb. The red spot indicates the thermal band gap ΔE from the present work, with its position in good agreement to the other experimental values and verifying that the by TEM-EDX determined antimony concentration of 8 at % is correct.

5.4.2 Magnetoresistance Effect of BiSb Nanowires

The magnetic field dependent resistance of bismuth antimony nanowires is measured in the temperature range of 50 – 400 K in transverse magnetic fields up to ±2 T using the electrical transport option ETO from the *Versalab* (see sec. 5.2.1).

Exemplarily the field dependent MR effect at 150 K is shown in figure 5.19 (a) and in figure 5.20 (a) for the as-prepared and the tempered nanowires respectively. Both kind of wires show a parabolic behavior at low magnetic fields.

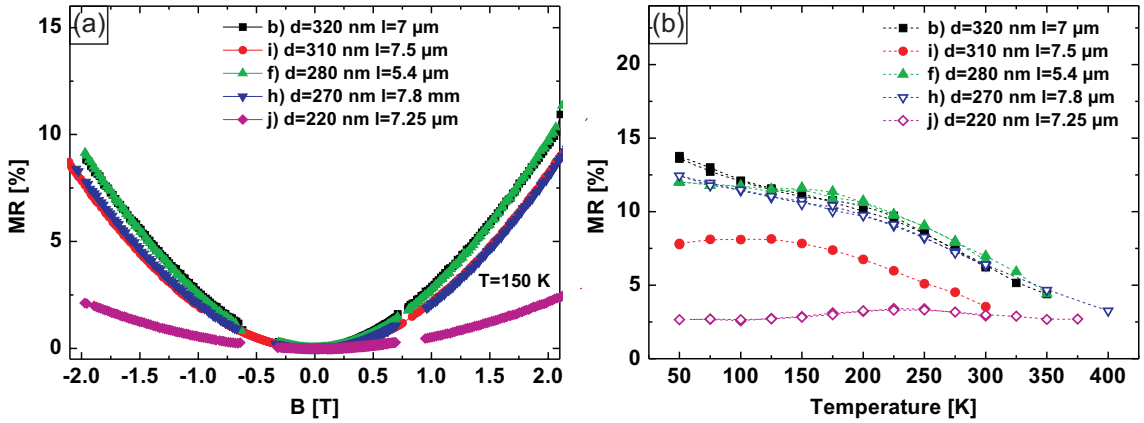

Figure 5.19: (a) Magnetic field dependent magnetoresistance effect for different as-prepared BiSb nanowires at 150 K. (b) Temperature dependent magnetoresistance effect for different as-prepared BiSb nanowires at transverse magnetic field of 2 T. The dashed lines are guides to the eye.

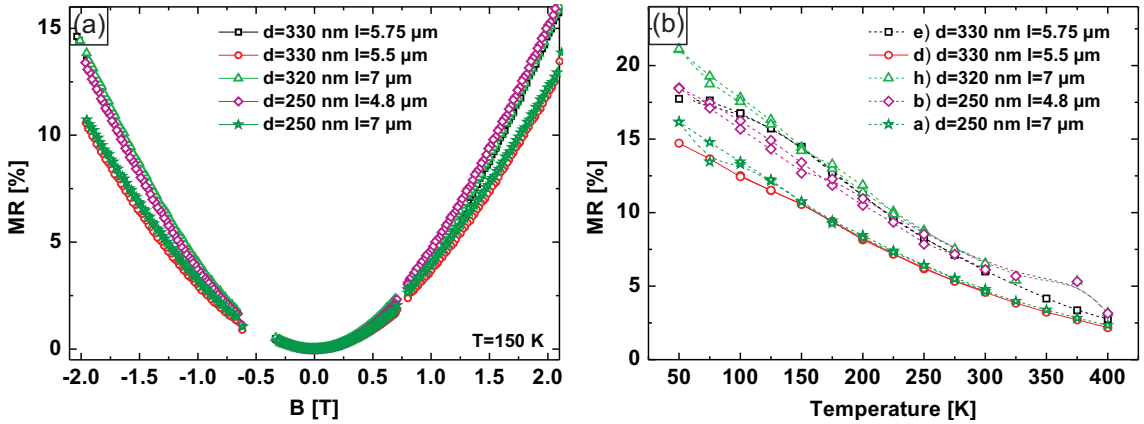

Figure 5.20: (a) Magnetic field dependent magnetoresistance effect for different tempered BiSb nanowires at 150 K. (b) Temperature dependent magnetoresistance effect for different tempered BiSb nanowires at transverse magnetic field of 2 T. The dashed lines are guides to the eye.

The comparison of the temperature dependent MR effect at 2 T displays mixed performances of the as-prepared nanowires (see fig. 5.19 (b)) and a monotonic increase of the MR effect for bismuth antimony nanowires after annealing (see fig. 5.19 (b)). The increase of the MR effect at a given magnetic field is for the as-prepared wires less pronounced than for the annealed. This can be ascribed to less impurity scattering, resulting in longer lifetimes τ of the carriers (see sec. 5.2.1) in the annealed wires.

To fit the experimental data and for the determination of the galvanomagnetic coefficient A, equation 5.9 is used. As it has been already mentioned in the section about pure bismuth nanowires 5.3, A is highly related to the mobilities and therefore to the mean free path of the carriers. Figure 5.21 (a) shows the temperature dependence of A for the as-prepared bismuth antimony nanowires with different diameters. All wires show a minor temperature dependence with slightly pronounced maxima which shifts to higher temperatures for wires with smaller diameters. The temperature dependence of A for the annealed bismuth antimony nanowires is given in figure 5.21 (b). All wires show essentially a monotonic increase of A with decreasing temperature.

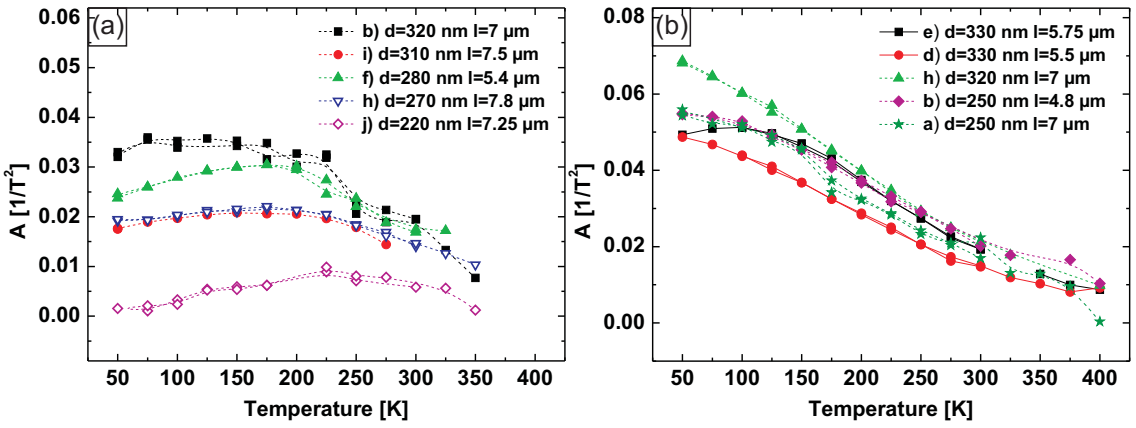

Figure 5.21: (a)Temperature dependence of the magnetoresistance coefficient A for as-prepared BiSb nanowires. (b) Temperature dependence of the magnetoresistance coefficient A for annealed BiSb nanowires. The coefficient has been fitted to a square function of the magnetic field at low fields. The dashed lines are guides to the eye.

The insignificant change of the galvanomagnetic coefficient A with temperature indicates that in the as-prepared nanowires impurity scattering is more pronounced than in the wires after annealing what can be ascribed to a less homogenous distribution of the antimony atoms in the wires.

For polycrystalline $Bi_{1-x}Sb_x$ alloys it has been shown by Malik *et al.* [MDM+12] that the resistivity rises with the Sb content because of increased impurity scattering and decreas-

ing grain sizes due to lattice changes caused by the smaller Sb atoms. Whereas in case of the annealed wires a similar behavior of the galvanomagnetic coefficient A of pure antimony nanowires is explained by the key influence of phonon scattering to the total mobility [HTL+01]. For BiSb nanowires prepared with a pressure injection technique it was found that the Sb concentration along the wire is inhomogenous [HOE02] and for alloys of nanowires that have been prepared with a similar method it has been shown that the (magneto) transport properties strongly depend on the antimony concentration [LRC+02a].
In total it becomes obvious how sensitive this system is to structural or compositional changes. However the presented measurements of single electrodeposited $Bi_{1-x}Sb_x$ nanowires have shown that the properties of the wires become reproducable after an annealing process, making these wires promising candidates for further investigation.

5.4.3 Low Temperatures and High Fields

Additional to the investigation of the magnetotransport properties of BiSb nanowires in the temperature range 50 – 350 K and in magnetic fields up to ±2 T, an as-prepared bismuth antimony nanowires measured using the *Dynacool* measurement setup (see sec. 5.2). With temperatures down to 1.8 K and magnetic fields up to ±9 T some more features of the wires were observable, which is already pronounced in the slope of the temperature dependent resistance. The temperature dependent resistivity of a bismuth antimony with a diameter

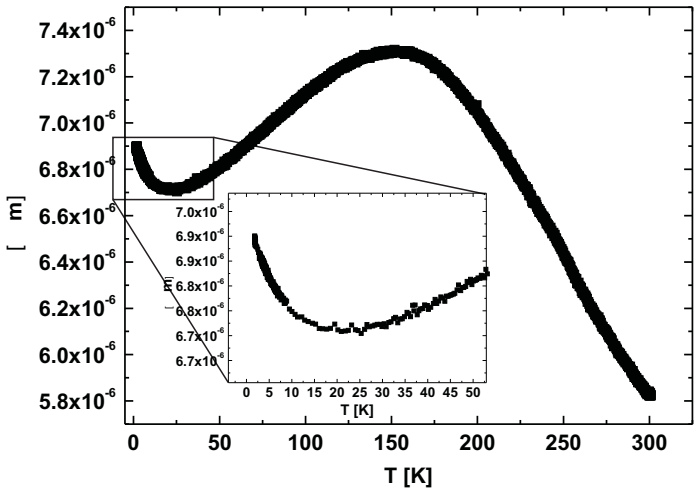

Figure 5.22: Resistance of a $d = 220$ nm BiSb nanowires in the temperature range 1.8 – 300 K the inset shows the anomalous increase of the resistance below 10 K.

of $d = 220$ nm and a length of $l = 5.2$ µm is given in figure 5.22. As previously observed the resistivity of as-prepared BiSb nanowires have nonmonotonic temperature dependence.

Here the resistivity increases with decreasing temperature and starts to decrease again below 140 K. At temperatures < 10 K the resistance re-increases, (see the inset of fig. 5.22) which indicates some kind of localization or size effects.
The existence of size effects is also shown in the temperature depending behavior of the resistance in presence of a magnetic field. In figure 5.23 (a) the MR effect of the wire measured in fields up to $B = \pm 9$ T is given for different temperatures. As already seen before it is quadratical depending on the field for low magnetic fields. With rising strength of the magnetic field the increase becomes linear above fields of ±3 T. A comparison of the MR effect at $B = 2$ T (black squares) and $B = 9$ T (red dots) is given in figure 5.23 (b). Below a temperature of 50 K one has to differ between low-field and high-field behavior of the magentoresistance. Regarding field strength of 2 T the effect saturates at low temperature whereas the slope at decreases further at 9 T. For illustration, the field-dependent magnetoresistance effects for temperatures below 30 K are given in figure 5.24 (a). One can not distinguish between the curves, all values are at the same level up to fields of ±6.5 T where a decrease in the slope of the curves is observable.

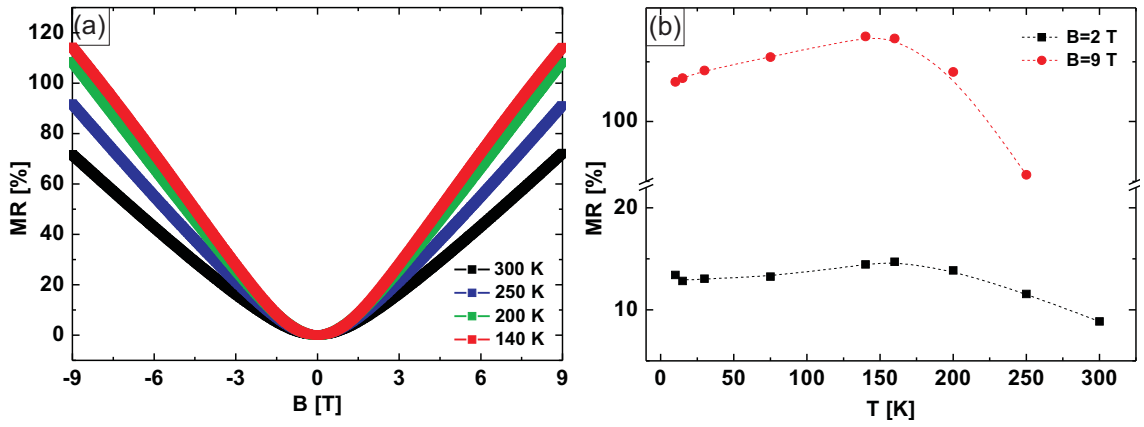

Figure 5.23: (a) Magnetic field dependent MR effect of a $d = 220$ nm BiSb nanowire in fields up to ±9 T for different temperatures. (b) Temperature dependence of the magnetoresistance effect at $B = 2$ T (black squares) and $B = 9$ T (red dots). The dashed lines are guides to the eye.

This inflection point occurs when the cyclotron radius r_c, given by $r_c = \frac{m^* \cdot v_F}{eB}$ with the effective mass m^*, the fermi velocity v_F, the electron charge e and the magnetic field B, becomes smaller than the dimension of the measured sample. Then surface scattering is suppressed resulting in a decrease of the MR effect.
Also at low magnetic fields, size effects are observable at temperatures below 3 K. As indicated by the vertical line in figure 5.24 (b) a steplike increase of the magnetoresistance is shown at 1.8 K and at 2 K. The position of the step is temperature independent and the corresponding critical magnetic field B_c marks the position at which the magnetic length

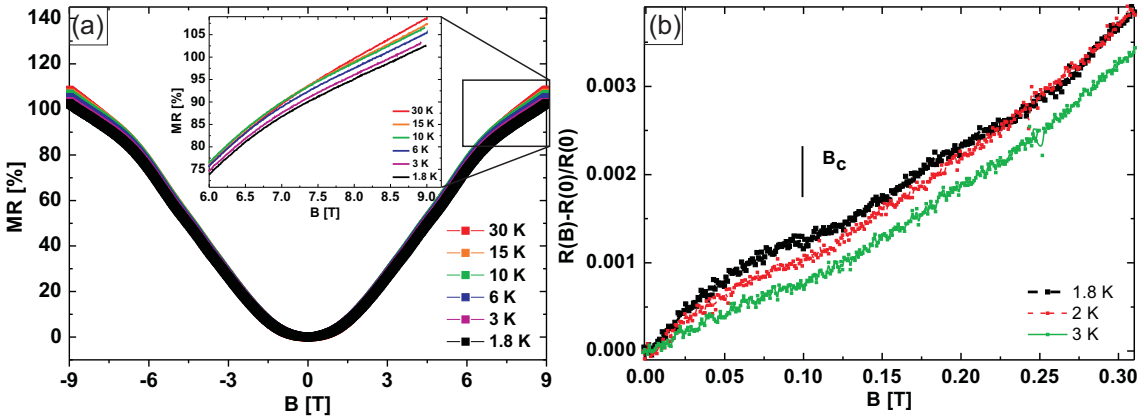

Figure 5.24: (a) Magnetic field dependent magnetoresistance effect of a BiSb nanowire in fields up to ±9 T and below temperatures of 30 K. The inset shows the damping of the MR effect of a BiSb nanowire at high field above ±6 T and at temperature between 1.8 – 30 K. (b) Anomaly of the magnetoresistance at low fields and low temperature.

L_H equals the wire diameter d. Then the magnetic length correspond to the spatial extent of the wave function of an electron at the ground state (lowest LANDAU level (ground state) (LLL) [OZD+12]) and is expressed by the equation:

$$L_H = \sqrt{(\frac{\hbar}{eB_c})} \tag{5.16}$$

with $\hbar$ being PLANCK´s constant. Thus by knowing the diameter of the wire the critical magnetic field B_c can be calculated or for known critical magnetic field the diameter of the wire can be determined.
In this study B_c = 0.103 T has been determined which leads to a calculated diameter of d = 200 nm. This value is in excellent agreement with the diameter determined by SEM. Similar effects have been reported by HEREMANS *et al.* [HTZ+98] for arrays of pure bismuth and pure antimony nanowires but not for BiSb alloys. Further investigation of the material especially of tempered BiSb nanowires are desirable.

5.4.4 Seebeck Coefficient of BiSb Nanowires

To determine the SEEBECK coefficient of bismuth antimony nanowires the thermovoltage U_{thermo} dependent on the heating power is measured. The temperature at both ends of the wires, thus the temperature gradient ΔT is measured via platinum stripes over the nanowires which act as thermometers and as well as contacts (compare sec. 5.2.2). Thus the SEEBECK coefficient can be calculated using equation (1.1) from section 1.1. The sign of the measured

Seebeck coefficient of as-prepared and tempered BiSb nanowires is negative, and the temperature dependent values are given in figure 5.25 (a)+(b). The black squares resemble the

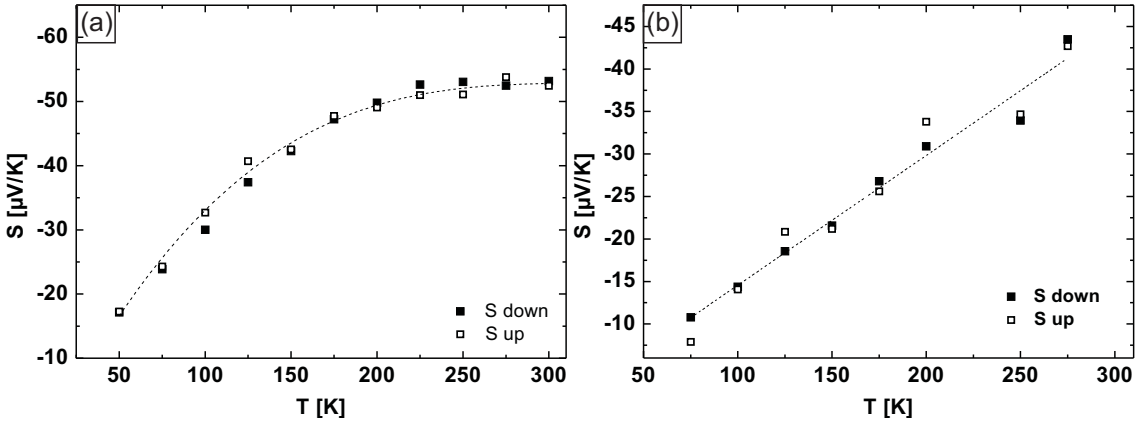

Figure 5.25: (a) Temperature dependent Seebeck coefficient of an $d = 250\,\text{nm}$ as-prepared BiSb nanowire. The dashed line is a guide to the eye. (b) Temperature dependent Seebeck coefficient of a $d = 360\,\text{nm}$ BiSb nanowire after an annealing process. The dashed line is a linear fits to zero with a slope of $0.152\,\mu\text{VK}^{-2}$.

values of S determined during the measurements from 300 K to 50 K and the open squares those from the measurements upwards from 50 K to 300 K. For both traces the Seebeck coefficient show the same temperature dependence within a deviation of $\pm 4\,\mu\text{VK}^{-1}$ between the single values. Thus, S can be considered independent of the measurement cycle.

The Seebeck coefficient of the as-prepared BiSb nanowire, given in fig. 5.25 (a), exhibits a positive slope over the whole temperature range and a saturation at temperatures above 250 K. Thus, the maximum power factor pf is expected to be in this temperature range. The diameter and length of the wire are determined by SEM to $d = 250\,\text{nm}$ and $l = 8\,\mu\text{m}$ and its resistance is measured via the contact pads 3 & 7 of the Seebeck structure (compare fig. 5.6). The measured resistance $R \approx 2\,\text{k}\Omega$ led to a resistivity of $\rho = 1.2 \cdot 10^{-5}\,\Omega\text{m}$ which can be assumed as the maximum limit since it is determined by a two-point measurement technique. With the Seebeck coefficient of $S = -52\,\mu\text{VK}^{-1}$ at 300 K the lower limit of the power factor $pf = S^2 \cdot \sigma$ can be calculated to $250\,\mu\text{WK}^{-2}\text{m}^{-1}$. Regarding the resistivity values of the wires presented previously, power factors between $250 - 450\,\mu\text{WK}^{-2}\text{m}^{-1}$ can be estimated. Since the exact value of the Seebeck coefficient for the single wires is not known this is only taken as an assumption on the order of magnitude of the power factor of as-prepared electrodeposited nanowires.

The temperature dependent Seebeck coefficient of an annealed BiSb nanowire is given in figure 5.25 (b). The absolute value of S rises linear with a slope of $-0.152\,\mu\text{VK}^{-2}$ and does not show any saturation behavior towards higher temperatures. The slope is in the same

order of magnitude as for GaN nanowires presented by Lee *et al.* [LYZK09] and for bismuth nanowires presented by Heremans and Trush [HT99]. With the assumption that the Mott relation [MD71] is valid and that the mobility is energy-independent, the carrier concentration can be calculated using the following equation:

$$n = \frac{1}{3\pi^2}\left(\frac{\pi^2 k_B^2 m^*}{\hbar^2 e S/T}\right)^{3/2} \tag{5.17}$$

where k_B is the Boltzmann constant, $\hbar$ is Planck 's constant, m^* is the effective mass and e is the electric charge. Estimating an effective mass of BiSb in the order of $m* = 0.01 m_e$ [Gol70, CDW+99] a carrier density of $n \approx 5 \cdot 10^{17}\,\mathrm{cm}^{-3}$ is determined.
The measured two-point resistance of the wire is $R = 400\,\Omega$. Together with the diameter of $d = 360\,\mathrm{nm}$ and length $l = 8\,\mu\mathrm{m}$ the resistivity is calculated to $\rho = 0.5 \cdot 10^{-5}\Omega\mathrm{m}$. The power factor of the annealed bismuth antimony nanowire taking a Seebeck coefficient of $S = -45\,\mu\mathrm{VK}^{-1}$ is $pf \approx 400\,\mu\mathrm{WK}^{-2}\mathrm{m}^{-1}$. Thus, even though the Seebeck coefficient of the annealed wire is lower than that of the as-prepared wire, the power factor is in the same order of magnitude. A similar effect is observed in bismuth thin films (compare section 3.4) which also show a slightly lower Seebeck coefficient after an annealing process.
Nevertheless, taking the other temperature and field depending measurement on single BiSb nanowires into account one can state that also for the thermoelectric performance an annealing process is useful. Since the Seebeck coefficient of the annealed wire does not tend to saturate, already even higher power factors can be expected for higher temperatures. Values

S_{max} [$\mu\mathrm{VK}^{-1}$]	pf_{max} [$\mu\mathrm{WK}^{-2}\mathrm{m}^{-1}$]	diameter [nm]	$Bi_{1-x}Sb_x$	comment	Ref.
−48 at 300 K	–	65	$x = 0.05$	NW array	[LRC+02a,
−55 at 300 K		40			LRC+02b]
−15 at 180 K	—	100	—	NW array	[Mue12]
−10 at 300 K		50			
−170 at 70 K	$60 \cdot 10^3$	1600	$x = 0.02$	monocrystalline	[NKH+12]
−150 at 225 K		400			
−120 at 250 K		300			
−52 at 300 K	250	250	$x = 0.08$	as-prepared	present work
−45 at 300 K	400	360	$x = 0.08$	annealed	present work

Table 5.3: The table gives a small overview on the Seebeck coefficient of BiSb nanowires reported in the literature.

of measured Seebeck coefficients of nanowire (NW) arrays as well as of single wires are given in table 5.3. The comparison of those values shows, as for pure bismuth samples,

the anisotropy of BiSb, but also the potential of the material for thermoelectric applications [LCM+96, LDC+98, SW62]. As pure bismuth, BiSb is highly anisotropic and its properties and peak performances does not only depend on the crystal orientation and temperature, but also on the antimony content [LCM+96, LDC+98, SW62]. Cho *et al.* [CDW+99] has observed non-monotonic temperature dependent behavior of the Seebeck coefficient of $Bi_{1-x}Sb_x$ thin films regarding different antimony concentration. Peak performances and a power factor of $pf = 12 \cdot 10^3\,\mu WK^{-2}m^{-1}$ at 80 K has been achieved for $x = 0.12$, whereas the maximum power factor $pf = 600\,\mu WK^{-2}$ for thin films with an antimony concentration of 7.2 at % occurred around 220 K.

In general one can say that the maximum values of S of single Bi and $Bi_{1-x}Sb_x$ nanowires are slightly lower than those achieved for thin films (compare sec. 3.4 and sec. 3.5). Nevertheless, as for the thin films the slight addition of antimony to the structure has a positive effect on the absolute value of the Seebeck coefficient. And with a suitable contacting process it is possible to determine the power factor of electrodeposited single nanowires. Furthermore it is shown that a tempering process of $Bi_{1-x}Sb_x$ nanowires improve the internal or crystal structure of the single wires and allows prediction of their behavior. As-prepared BiSb nanowires showed mixed temperature dependent transport behavior, changing from semiconductive to metallic behavior with decreasing temperature. Whereas the tempered wires show a semiconductive increase of the resistivity with decreasing temperature over the whole range 300 – 50 K, indicating that the heat treatment leads to a homogeneous distribution of the antimony atoms in the wires.

Summary and Outlook

A comprehensive investigation of electrodeposited bismuth and bismuth antimony nanostructures has been carried out during this work. The uniqueness of this material system and the suitability of electrodeposition as synthesis method has been verified by measurements on thin films and single nanowires.
In the first instance different bismuth and bismuth antimony electrolytes, using either HNO_3 or HCl as solvent and different concentration of $Bi(NO_3)_3 + 5H_2O$ and $BiCl_3$ respectively have been characterized. By using cyclic voltammetry (CV) the suitable deposition potentials have been determined (see sec. 2.2). Based on these results, series of BiSb thin films have been deposited. Structural analysis with XRD have shown that the electrodeposited films are single phase and polycrystalline with an increasing texturing along the (012) direction for increasing antimony content. To obtain the composition of the films, deposited with different potentials, chemical analysis and EDX analysis have been performed. It was found that the antimony content increases with more negative potentials (compare figure 3.9 and figure 3.10).
Additionally the Seebeck coefficient S of the thin films at room temperature has been measured. For the first time the Seebeck coefficient depending on the antimony content could be reported for electrodeposited thin films. Below an antimony concentration of ~ 40 at % the value of S increases with decreasing antimony concentrations. Above this value the Seebeck coefficient drops even below the value of pure bismuth thin films ($S_{Bi} = -55\ \mu VK^{-1}$ see sec. 3.4 and sec. 3.5). Whereas the highest absolute Seebeck coefficient of $S_{BiSb} = -85\ \mu VK^{-1}$ was achieved for the films with the lowest antimony concentration.

The results from the characterization of the thin films have been transferred to the electrodeposition of nanowires in order to obtain BiSb wires with an antimony concentration below 20 at %. The nanowires were produced by electrochemical deposition into oxalic and phosphoric acid membranes (compare sec. 4.1) in order to achieve wires of different diameters. The wires have been released from the membranes, giving the opportunity to perform structural and electrical analysis on single wires. Transmission electron microscopy TEM of single bismuth and bismuth antimony wires have revealed that the pulsed electrodeposited wires are single crystalline over a large range and that the pure bismuth wires are highly

textured along the (110) direction.
A suitable contacting process for single wires has been developed during this work which allows to obtain absolute values of the resistivity of the wires. The magnetoresistance MR effect and the SEEBECK effect of bismuth single wires and bismuth antimony single wires have been measured between 50 – 300 K. Concerning the bismuth antimony nanowires the effect of annealing has been investigated.

The resistivity values of the single bismuth wires were only 1.6 – 2.94 higher than the value of bulk material ($\rho = 1.29 \cdot 10^{-6}\,\Omega$m), verifying the good quality of the electrodeposited wires. Magnetoresistance MR effects up to 60 % have been reached in fields of ±2 T. The galvanomagnetic coefficient *A* has been determined by a fit to the the quadratic part of the magnetoresistance and thus the temperature dependent electron and hole mobilities of the wires could be calculated. Room temperature electron mobilities even higher than of graphene on SiO_2 have been achieved [DBP10, ZBG+09, MAU+08].
Measurements of the bismuth antimony samples displayed a difference between as-prepared and annealed wires. The temperature dependent behavior of the as-prepared wires might differ from wire to wire whereas the annealed wires all showed predictable, uniform semiconductive behavior. Both, EDX and the electrical analysis sums the expected antimony content of ~ 10 at % in the wires proving that electrodepostion is a suitable method to fabricate BiSb nanowires. To my knowledge the SEEBECK coefficient of electrodeposited single BiSb nanowires has been measured for the first time. The comparison between as-prepared and annealed wires led to minor changes of *S* after the tempering process. Nevertheless the conclusion can be drawn that annealing is a worthwhile process step since it has been shown before that the transport properties of the wires become much more predictable. The maximum power factor of the single wires has been determined at room temperature with a value of ~ 300 $\mu WK^{-2}m^{-1}$ proving that bismuth antimony compounds are suitable candidates for thermoelectric research.

In summary it has been shown that electrodeposition is a suitable approach for the fabrication of thermoelectric material. High quality thin films as well as nanowires can be fabricated with this low cost method what makes it attractive for various material systems.
Within this work the thermoelectric characterization of electrodeposited $Bi_{1-x}Sb_x$ structures has shown that peak performances are reached for antimony contents below Sb < 10 at%. Measurements on $Bi_{0.92}Sb_{0.08}$ single wires exhibit optimum performances around 300 K, making it a optimum candidate for all kinds of thermoelectric applications operating at room temperature.

A Process Parameters

A.1 Overview of Electrolytes

- all used electrolytes are presented with a description of the composition and guide line of the preparation

A.1.1 Pure Bi Electrolyte

- 0.04 molL^{-1} bismuth(III) nitrat penthahydrate, $Bi(NO_3)_3$+$5H_2O$ (*Sigma Aldrich*, 99.999 %)
- 0.7 molL^{-1} nitric acid, HNO_3 (*Merck* 69 %)
- fill up with DI-water

A.1.2 BiSb Electrolytes on HNO_3 Basis

General Preparation steps

- all solutions have been prepared with a volume of 100 mL
- dissolving of the tartaric acid $C_4H_6O_6$ (*VWR*, L(+)-tartaric acid for analysis), in DI-water by stirring at 70 °C
- dissolving of the $Bi(NO_3)_3$+$5H_2O$ in nitric acid and DI-water by stirring
- add the antimony oxide, Sb_2O_3 (*Sigma Aldrich*, 99.999 %) to the tartaric acid/DI-water mixture and stir until the antimony oxide is dissolved
- mix both solutions together and fill up with DI-water

BiSb-a-sol

- 0.005 molL^{-1} $Bi(NO_3)_3 \cdot 5H_2O$
- 1 molL^{-1} HNO_3 69 %

- 0.84 molL^{-1} tartaric acid, $C_4H_6O_6$
- 0.0056 molL^{-1} antimony oxide, Sb_2O_3

BiSb-d-sol

- 0.0075 molL^{-1} $Bi(NO_3)_3$+5H_2O
- 1 molL^{-1} HNO_3 69 %
- 0.84 molL^{-1} tartaric acid, $C_4H_6O_6$
- 0.0056 molL^{-1} antimon oxide, Sb_2O_3

A.1.3 BiSb Electrolytes on HCl Basis

General Preparation Steps

- dissolving of the tartaric acid $C_4H_6O_6$ (*VWR*, L(+)-tartaric acid for analysis), in DI-water by stirring at 70 °C
- dissolving of the bismuth(III) chloride $BiCl_3$ (*Sigma Aldrich*, > 98 %) in hydrochloric acid and DI-water by stirring
- add the antimon oxide, Sb_2O_3 (*Sigma Aldrich*, 99.999 %) to the tartaric acid/DI-water mixture and stirr until the antimony oxide is dissolved
- mix both solutions together add glycerol (*VWR*, 99.9 %) and fill up with DI-water

HCl-a-BiSb sol

- 0.05 molL^{-1} $BiCl_3$
- 0.5 molL^{-1} HCl
- 50 gL^{-1} $C_4H_6O_6$
- 0.02 molL^{-1} Sb_2O_3
- 100 gL^{-1} glycerol

HCl-d-BiSb sol

- 0.075 molL^{-1} $BiCl_3$
- 0.5 molL^{-1} HCl
- 50 gL^{-1} $C_4H_6O_6$
- 0.02 molL^{-1} Sb_2O_3
- 100 gL^{-1} glycerol

A.2 Si Substrates for Electrodeposition

- all following steps are performed using a *Cressington 308R* sputtering machine

A.2.1 Sputtering of Chromium (Cr)

- wait until the pressure has reached $1 \cdot 10^{-6}$ mbar
- start sample rotation
- deposit with a current of I=20 mA for 1.5 min

A.2.2 Sputtering of Platinum (Pt)

- wait until the pressure has reached $1 \cdot 10^{-6}$ mbar
- start sample rotation
- deposit with a current of I=40 mA for 4 min

A.3 Anodic Aluminum Oxide

A.3.1 Electropolishing of Aluminium Chips

Preparation of the Electropolishing Solution

- take 60 – 65 % perchloric acid (*VWR*, $HClO_4$) and > 95 % Ethanol (*VWR*, EtOH V)
- mix cooled perchloric acid and ethanol in the volume ratio 1/3

Electropolishing

- 100 mL of electropolishing solution per cell
- polish for 3 min at a potential of 20 V with stirring
- change the stirring direction every 30 s
- cleaning of the cells with isopropanol and DI-water

A.3.2 Preparation of 0.3 molL^{-1} Oxalic Acid

- mix 3.78 g of $H_2C_2O_4$ (*Merck*, oxalic acid dihydrate, extra pure) in 100 mL DI-water
- stir until all of the powder is dissolved

A.3.3 Preparation of 1 wt % Phosphoric Acid

- take 85 % H_3PO_4
- mix 0.688 mL of H_3PO_4 in 100 mL DI-water

A.3.4 First Anodization

Anodization with Oxalic Acid

- 100 mL of oxalic acid per cell
- cooling the system down to 8 °C
- anodize at a potential of 40 V
- the anodization time is supposed to be >12 h
- the solution is stirred during the whole process

Anodization with Phosphoric Acid

- 100 mL of phosphoric acid (1 wt %) per cell
- cooling the system down to 2 °C
- anodize at a potential of 170 V for 3 h

- stepwise increase the potential to 195 V, with 0.1 mVs^{-1}
- the anodization time is supposed to be >12 h
- the solution is stirred during the whole process

A.3.5 Removing of the first Alumina Layer

Preparation of Phosphoric-chromic Acid

- take 85 % H_3PO_4 and pure CrO_3 (solid)
- mix 1.8 g CrO_3 with 7.1 g H_3PO_4
- fill up with DI-water to 100 mL

Etching of the Alumina

- cover the chips with the acid and leave them in a heat cabine at 45 °C for >12 h
- alternatively use a heat plate at 60 °C for 6 h
- cleaning of the cells with isopropanol and DI-water

A.3.6 Second Anodization

Anodization with Oxalic Acid

- 100 mL of oxalic acid per cell
- cooling the system down to 8 °C
- anodize at a potential of 40 V
- the growth rate is 3.5 μmh^{-1}
- the solution is stirred during the whole process

Anodization with Phosphoric Acid

- 100 mL of water per cell
- cooling the system down to 2 °C
- add 0.788 mL phosphoric acid (85 wt %) to the water
- anodize at 195 V
- the growth rate is 2 $\mu m h^{-1}$
- the solution is stirred during the whole process

A.3.7 Removing of the Aluminum Back-Layer

Preparation of the CuCl/HCl Solution

- take 37 % HCl (*Merck*, hydrochloric acid fume) and pure copper chloride $CuCl_2$ (*Sigma Aldrich*, copper(III) chloride dihydrate, reagent grade)
- mix 6.8 g of $CuCl_2$ with 100 mL HCl
- fill up with DI-water to 200 mL

Etching of the Aluminum

- cover the chips with the acid
- wait until no more copper falls out
- cleaning of the cells with isopropanol and DI-water

A.3.8 Removing of the Aluminum Oxide Barrier-Layer

- preparation of a 10 wt % phosphoric acid
- etch oxalic acid membranes 55 min at 45 °C
- etch phosphoric acid membranes 90 min at 45 °C
- cleaning of the cells with isopropanol and DI-water

A.4 Laser Lithography

A.4.1 LOR 3B Spin Off

- spin on the positive resist LOR 3B (*Micro Chem*) with 3500 rpm for 45 seconds (spin coater from *Süss MicroTec)*
- bake on a hot plate for 250 seconds at 180 °C

A.4.2 map 1205 Spin Off

- spin on the positive resist ma-P 1205 (*micro resist technology*)with 3500 rpm for 30 seconds
- bake on a hot plate for 30 seconds at 100 °C

A.4.3 Developing of the Photoresist

- develope for 20 s in the developer *mad-331* (*micro resist technology*)
- stop the reaction with DI-water
- check on an optical microscope and if necessary develop longer

A.5 Sputtering of Micro Contacts

- all following steps are done by using a *CRC-600* sputtering system from *TORR International, INC*

A.5.1 Sputtering-Cleaning for Micro Contacts

- set the power to 20 W
- start the plasma with an argon flow of 55 sccm
- set the argon flow down to 15 sccm
- the etch rate for SiO_2 is 1 nm min^{-1}

A.5.2 Sputtering of Titanium (Ti) for Micro Contacts

- set the power to 100 W
- start the plasma with an argon flow of 45 sccm
- set the argon flow down to 15 sccm
- run the process for 20 s

A.5.3 Sputtering of Platinum (Pt) for Micro Contacts

- set the power to 50 W
- start the plasma with an argon flow of 15 sccm
- run the process for 8 min

A.5.4 Lift-Off

- cover the sample with remover 1165 for 10 min at 80 °C
- renew the remover and keep the sample in it for another 10 min
- rinse of the metallic layer with DI-water and isopropanol

Bibliography

[Aon78] T. Aono, *Magneto-Seebeck Effect of Pb-Doped Bi–Sb*, Japanese Journal of Applied Physics **17** (1978), no. 5, 843–849.

[BBL00] F. Besse, C. Boulanger, and J. Lecuire, *Preparation of* $Bi_{1-y}Sb_y$ *films by electrodeposition*, Journal of Applied Electrochemistry **30** (2000), 385–392, 10.1023/A:1003990327662.

[BGG+08] A. Belwalkar, E. Grasing, W. V. Geertruyden, Z. Huang, and W. Misiolek, *Effect of processing parameters on pore structure and thickness of anodic aluminum oxide* (AAO) *tubular membranes*, Journal of Membrane Science **319** (2008), no. 1–2, 192 – 198.

[BH64] D. M. Brown, and F. K. Heumann, *Growth of Bismuth-Antimony Single-Crystal Alloys*, Journal of Applied Physics **35** (1964), no. 6, 1947–1951.

[BLJ+00] M. Boffoué, B. Lenoir, A. Jacquot, H. Scherrer, A. Dauscher, and M. Stölzer, *Structure and transport properties of polycrystalline* Bi *films*, Journal of Physics and Chemistry of Solids **61** (2000), no. 12, 1979 – 1983.

[BM01] S. E. Barati M., *Study of the ordinary size effect in the electrical conductivity of* Bi *nanowires*, Nanotech **12** (2001), 277.

[BS64] D. M. Brown, and S. J. Silverman, *Electrons in* Bi – Sb *Alloys*, Phys. Rev. **136** (1964), A290–A299.

[BXH06] A. Boukai, K. Xu, and J. Heath, *Size-Dependent Transport and Thermoelectric Properties of Individual Polycrystalline Bismuth Nanowires*, Advanced Materials **18** (2006), no. 7, 864–869.

[CAEL99] A. Cuna, R. Azevedo, S. Emmons, and A. Leroi, *Developmental biology: Variable cell number in nematodes*, NATURE **402** (1999), 253.

[CBC+05] T. W. Cornelius, J. Brötz, N. Chtanko, D. Dobrev, G. Miehe, R. Neumann, and M. E. T. Molares, *Controlled fabrication of poly- and single-crystalline bismuth nanowires*, Nanotechnology **16** (2005), no. 5, 246.

[CDHL00] Y. Cui, X. Duan, J. Hu, and C. M. Lieber, *Doping and Electrical Transport in Silicon Nanowires*, The Journal of Physical Chemistry B **104** (2000), no. 22, 5213–5216.

[CDVK+98] S. Cho, A. Di Venere, Y. Kim, G. K. Wong, J. B. Ketterson, J. Meyer, and C. Hoffman, *Structural and thermoelectric properties of MBE-grown doped and undoped BiSb alloy thin films*, Thermoelectrics, 1998. Proceedings ICT 98. XVII International Conference on, 1998, 284–287.

[CDW+99] S. Cho, A. DiVenere, G. K. Wong, J. B. Ketterson, and J. R. Meyer, *Transport properties of* $Bi_{1-x}Sb_x$ *alloy thin films grown on* CdTe(111)*B*, Phys. Rev. B **59** (1999), 10691–10696.

[Cha59] B. Chandrasekhar, *The Seebeck coefficient of bismuth single crystals*, Journal of Physics and Chemistry of Solids **11** (1959), no. 3–4, 268 – 273.

[CHH03] W. V. Carl H. Hamann, *Elektrochemie*, Wiley-VCH, 2003.

[Cho99] S. Cho (ed.), *Anisotropic Seebeck and magneto-Seebeck coefficients of Bi and BiSb alloy thin films*, 29s sept. 1999.

[CLR+02a] S. Cronin, Y. Lin, O. Rabin, M. Black, G. Dresselhaus, M. Dresselhaus, and P. Gai, *Bismuth nanowires for potential applications in nanoscale electronics technology.*, Microsc Microanal **8** (2002), no. 1, 58–63.

[CLR+02b] S. B. Cronin, Y.-M. Lin, O. Rabin, M. R. Black, J. Y. Ying, M. S. Dresselhaus, P. L. Gai, J.-P. Minet, and J.-P. Issi, *Making electrical contacts to nanowires with a thick oxide coating*, Nanotechnology **13** (2002), no. 5, 653.

[Cor06] T. W. Cornelius, *Fabrication and Characterisation of Bismuth Nanowires*, Ph.D. thesis, Ruperto-Carola University of Heidelberg, 2006.

[Cro01] S. Cronin (ed.), *Electronic Properties of Bismuth Nanowires*, vol. 679, 0 2001.

[Cro02] S. B. Cronin, *Electronic Properties of* Bi *Nanowires*, Ph.D. thesis, Massachusetts Institute of Technology, 2002.

[CTMNK06] T. W. Cornelius, M. E. Toimil-Molares, R. Neumann, and S. Karim, *Finite-size effects in the electrical transport properties of single bismuth nanowires*, Journal of Applied Physics **100** (2006), no. 11, 114307.

[CVW+97] S. Cho, A. D. Venere, G. Wong, J. Ketterson, J. Meyer, and C. Hoffman, *Thermoelectric power of* MBE *grown* Bi *thin films and* Bi/CdTe *superlattices on* CdTe *substrates*, Solid State Communications **102** (1997), no. 9, 673 – 676.

[CYL+00] C. L. Chien, F. Y. Yang, K. Liu, D. H. Reich, and P. C. Searson, *Very large magnetoresistance in electrodeposited single-crystal* Bi *thin films (invited)*, Journal of Applied Physics **87** (2000), no. 9, 4659–4664.

[DBP10] V. E. Dorgan, M.-H. Bae, and E. Pop, *Mobility and saturation velocity in graphene on* SiO_2, Applied Physics Letters **97** (2010), no. 8, 082112.

[DGCF04] T. Dürkop, S. A. Getty, E. Cobas, and M. S. Fuhrer, *Extraordinary Mobility in Semiconducting Carbon Nanotubes*, Nano Letters **4** (2004), no. 1, 35–39.

[dKB83] A. de Kuijper, and J. Bisschop, *Temperature dependence of concentrations and mobilities in thin bismuth films*, Thin Solid Films **110** (1983), no. 2, 99 – 106.

[DLL+09] X. Dou, G. Li, H. Lei, X. Huang, L. Li, and I. W. Boyd, *Template Epitaxial Growth of Thermoelectric* Bi/BiSb *Superlattice Nanowires by Charge-Controlled Pulse Electrodeposition*, Journal of The Electrochemical Society **156** (2009), no. 9, K149–K154.

[DS87] V. D. Das, and N. Soundararajan, *Size and temperature effects on the Seebeck coefficient of thin bismuth films*, Phys. Rev. B **35** (1987), 5990–5996.

[DSRD09] S. Dutta, V. Shubha, T. Ramesh, and F. D'Sa, *Thermal and electronic properties of* $Bi_{1-x}Sb_x$ *alloys*, Journal of Alloys and Compounds **467** (2009), no. 1–2, 305 – 309.

[Dug65] M. Dugué, *Propriétés électriques des solutions solides bismuth-antimoine*, physica status solidi (b) **11** (1965), no. 1, 149–158.

[DZH+06] Dou, Zhu, Huang, L. Li, and Li, *Effective Deposition Potential Induced Size-Dependent Orientation Growth of* Bi – Sb *Alloy Nanowire Arrays*, The Journal of Physical Chemistry B **110** (2006), no. 43, 21572–21575.

[FD08] K. Fukutani, and T. Den, *Fabrication of* Bi *Nanowire Array into Nanoporous Film Made from Phase-Separated* Al – Si *Film*, Japanese Journal of Applied Physics **47** (2008), no. 4, 2336–2338.

[GBA+99] A. Giani, A. Boulouz, B. Aboulfarah, F. Pascal-Delannoy, A. Foucaran, A. Boyer, and A. Mzerd, *Effect of antimony concentration on the electrical and thermoelectrical properties of* $(Bi_{1-x}Sb_x)_2Te_3$ *thin films grown by metal organic chemical vapour deposition (MOCVD) techniques*, Journal of Crystal Growth **204** (1999), no. 1-2, 91–96.

[GKS72] N. Garcia, Y. H. Kao, and M. Strongin, *Galvanomagnetic Studies of Bismuth Films in the Quantum-Size-Effect Region*, Phys. Rev. B **5** (1972), 2029–2039.

[Glu11] J. G. Gluschke, *Kontaktierung und Charakterisierung von Bi- und* Bi_2Te_3*-Nanostäbchen*, Bachelorthesis, Universität Hamburg, 2011.

[Gol70] H. J. Goldsmid, *Bismuth-Antimony Alloys*, physica status solidi (a) **1** (1970), no. 1, 7–28.

[Gur80] M. Gurvitch, *Resistivity anomaly in thin* Bi *wires: Possibility of a one-dimensional quantum size effect*, Journal of Low Temperature Physics **38** (1980), 777–791 (English).

[Har69] R. Hartman, *Temperature Dependence of the Low-Field Galvanomagnetic Coefficients of Bismuth*, Phys. Rev. **181** (1969), 1070–1086.

[Hei08] S. Heiderich, *Top-down- und Bottom-up-Prozessierung und elektrische Charakterisierung von III/V-Halbleiternanostrukturen*, Master's thesis, Rheinisch Westfälisch Technische Hochschule Aachen, 2008.

[HMB+93] C. A. Hoffman, J. R. Meyer, F. J. Bartoli, A. Di Venere, X. J. Yi, C. L. Hou, H. C. Wang, J. B. Ketterson, and G. K. Wong, *Semimetal-to-semiconductor transition in bismuth thin films*, Phys. Rev. B **48** (1993), 11431–11434.

[HMX+11] F. Han, et al., *Alumina-Sheathed Nanocables with Cores Consisting of Various Structures and Materials*, Angewandte Chemie International Edition **50** (2011), no. 9, 2036–2040.

[HOE02] T. E. Huber, O. Onakoya, and M. H. Ervin, *Constitutional supercooling and the growth of 200 nm Bi–Sb wire array composites*, Journal of Applied Physics **92** (2002), no. 3, 1337–1343.

[HT99] J. Heremans, and C. M. Thrush, *Thermoelectric power of bismuth nanowires*, Phys. Rev. B **59** (1999), no. 19, 12579–12583.

[HTL+00] J. Heremans, C. M. Thrush, Y.-M. Lin, S. Cronin, Z. Zhang, M. S. Dresselhaus, and J. F. Mansfield, *Bismuth nanowire arrays: Synthesis and galvanomagnetic properties*, Phys. Rev. B **61** (2000), no. 4, 2921–2930.

[HTL+01] J. Heremans, C. M. Thrush, Y.-M. Lin, S. B. Cronin, and M. S. Dresselhaus, *Transport properties of antimony nanowires*, Phys. Rev. B **63** (2001), 085406.

[HTWL02] T. C. Harman, P. J. Taylor, M. P. Walsh, and B. E. LaForge, *Quantum Dot Superlattice Thermoelectric Materials and Devices*, Science **297** (2002), no. 5590, 2229–2232.

[HTZ+98] J. Heremans, C. M. Thrush, Z. Zhang, X. Sun, M. S. Dresselhaus, J. Y. Ying, and D. T. Morelli, *Magnetoresistance of bismuth nanowire arrays: A possible transition from one-dimensional to three-dimensional localization*, Phys. Rev. B **58** (1998), no. 16, 10091–10095.

[HWJZ06] Q. Huang, W. Wang, F. Jia, and Z. Zhang, *Preparation of* $Bi_{2-x}Sb_xTe_3$ *thermoelectric films by electrodeposition*, Journal of University of Science and Technology Beijing, Mineral, Metallurgy, Material **13** (2006), no. 3, 277 – 280.

[HYL+99] K. Hong, F. Y. Yang, K. Liu, D. H. Reich, P. C. Searson, C. L. Chien, F. F. Balakirev, and G. S. Boebinger, *Giant positive magnetoresistance of* Bi *nanowire arrays in high magnetic fields*, Journal of Applied Physics **85** (1999), no. 8, 6184–6186.

[iMCA+08] A. F. i Morral, C. Colombo, G. Abstreiter, J. Arbiol, and J. R. Morante, *Nucleation mechanism of gallium-assisted molecular beam epitaxy growth of gallium arsenide nanowires*, Applied Physics Letters **92** (2008), no. 6, 063112.

[IT85] A. Ibrahim, and D. Thompson, *Thermoelectric properties of BiSb alloys*, Materials Chemistry and Physics **12** (1985), no. 1, 29 – 36.

[Jai59] A. L. Jain, *Temperature Dependence of the Electrical Properties of Bismuth-Antimony Alloys*, Phys. Rev. **114** (1959), 1518–1528.

[JJL+03] C. G. Jin, G. W. Jiang, W. F. Liu, W. L. Cai, L. Z. Yao, Z. Yao, and X. G. Li, *Fabrication of large-area single crystal bismuth nanowire arrays*, J. Mater. Chem. **13** (2003), 1743–1746.

[Kao63] Y.-H. Kao, *Cyclotron Resonance Studies of the Fermi Surfaces in Bismuth*, Phys. Rev. **129** (1963), 1122–1131.

[KBNA71] Y. F. Komnik, E. I. Bukhshtab, Y. V. Nikitin, and V. V. Andrievskiĭ, *Features of Temperature Dependence of the Resistance of Thin Bismuth Films*, Soviet Journal of Experimental and Theoretical Physics **33** (1971), 364.

[KNK+04] H. Kitagawa, H. Noguchi, T. Kiyabu, M. Itoh, and Y. Noda, *Thermoelectric properties of* Bi–Sb *semiconducting alloys prepared by quenching and annealing*, Journal of Physics and Chemistry of Solids **65** (2004), no. 7, 1223 – 1227.

[Kom99] Komvarov (ed.), *Influence of films and substrates thermal expansion discrepancy on bismuth film thermoelectric properties*, 1999.

[KOSH78] W. Kraak, G. Oelgart, G. Schneider, and R. Herrmann, *The Semiconductor-Semimetal Transition in* $Bi_{1-x}Sb_x$ *Alloys with* $x \leq 0.22$, physica status solidi (b) **88** (1978), no. 1, 105–110.

[KSVD04] R. Kanakala, P. V. Singaraju, R. Venkat, and B. Das, *Modeling of Porous Alumina Template Formation under Constant Current Conditions*, Journal of the Electrochemical Society **152** (2004), no. 1, 1–5.

[KWC+09] C. Kaiser, G. Weiss, T. W. Cornelius, M. E. Toimil-Molares, and R. Neumann, *Low temperature magnetoresistance measurements on bismuth nanowire arrays*, Journal of Physics: Condensed Matter **21** (2009), no. 20, 205301.

[LCM+96] B. Lenoir, M. Cassart, J.-P. Michenaud, H. Scherrer, and S. Scherrer, *Transport properties of Bi-rich Bi-Sb alloys*, Journal of Physics and Chemistry of Solids **57** (1996), no. 1, 89–99.

[LCS98] K. Liu, C. L. Chien, and P. C. Searson, *Finite-size effects in bismuth nanowires*, Phys. Rev. B **58** (1998), no. 22, 14681–14684.

[LCSYZ98a] K. Liu, C. L. Chien, P. C. Searson, and K. Yu-Zhang, *Structural and magneto-transport properties of electrodeposited bismuth nanowires*, Applied Physics Letters **73** (1998), no. 10, 1436–1438.

[LCSYZ98b] K. Liu, C. Chien, P. Searson, and K. Yu-Zhang, *Giant positive magnetoresistance in arrays of semi-metallic bismuth nanowires*, Magnetics, IEEE Transactions on **34** (1998), no. 4, 1093–1095.

[LCY+00] Y.-M. Lin, S. B. Cronin, J. Y. Ying, M. S. Dresselhaus, and J. P. Heremans, *Transport properties of* Bi *nanowire arrays*, Applied Physics Letters **76** (2000), no. 26, 3944–3946.

[LDC+98] B. Lenoir, A. Dauscher, M. Cassart, Y. Ravich, and H. Scherrer, *Effect of antimony content on the thermoelectric figure of merit of* $Bi_{1-x}Sb_x$ *alloys*, Journal of Physics and Chemistry of Solids **59** (1998), no. 1, 129 – 134.

[LDP+95] B. Lenoir, A. Demouge, D. Perrin, H. Scherrer, S. Scherrer, M. Cassart, and J. Michenaud, *Growth of* $Bi_{1-x}Sb_x$ *alloys by the traveling heater method*, Journal of Physics and Chemistry of Solids **56** (1995), no. 1, 99 – 105.

[LGH+13] B. Landschreiber, et al., *Structural and Thermoelectric Properties of* $Bi_{1-x}Sb_x$ *Nanoalloys Prepared by Mechanical Alloying*, Journal of Electronic Materials (2013), 1–6 (English).

[LJGN06] W. Lee, R. Ji, U. Gosele, and K. Nielsch, *Fast fabrication of long-range ordered porous alumina membranes by hard anodization*, Nat Mater **5** (2006), no. 9, 741–747.

[LLH+10] K. Lee, S. Lee, S. N. Holmes, J. Ham, W. Lee, and C. H. W. Barnes, *Electron and hole mobilities in semimetallic bismuth nanowires*, Phys. Rev. B **82** (2010), 245310.

[LLZ+04] L. Li, G. Li, Y. Zhang, Y. Yang, and L. Zhang, *Pulsed Electrodeposition of Large-Area, Ordered* $Bi_{1-x}Sb_x$ *Nanowire Arrays from Aqueous Solutions*, The Journal of Physical Chemistry B **108** (2004), no. 50, 19380–19383.

[LOT07] LOT, *Panco Potential Seebeck Microprobe*, http://www.lot-oriel.com/files/downloads/panco/en/psm.pdf, 07 2007.

[LRC+02a] Y.-M. Lin, O. Rabin, S. B. Cronin, J. Y. Ying, and M. S. Dresselhaus, *Semimetal–semiconductor transition in* $Bi_{1-x}Sb_x$ *alloy nanowires and their thermoelectric properties*, Applied Physics Letters **81** (2002), no. 13, 2403–2405.

[LRC+02b] Y.-M. Lin, O. Rabin, S. Cronin, J. Ying, and M. Dresselhaus, *Experimental investigation of thermoelectric properties of* $Bi_{1-x}Sb_x$ *nanowire arrays*, Thermoelectrics, 2002. Proceedings ICT '02. Twenty-First International Conference on, 2002, 253–256.

[LSD00] Y.-M. Lin, X. Sun, and M. S. Dresselhaus1, 2, *Theoretical investigation of thermoelectric transport properties of cylindrical Bi nanowires*, Phys. Rev. B **62** (2000), no. 7, 4610–4623.

[LSS+08] W. Lee, K. Schwirn, M. Steinhart, E. Pippel, R. Scholz, and U. Gosele, *Structural engineering of nanoporous anodic aluminium oxide by pulse anodization of aluminium*, Nat Nano **3** (2008), no. 4, 234–239.

[LW78] J. I. Langford, and A. J. C. Wilson, *Scherrer after sixty years: A survey and some new results in the determination of crystallite size*, Journal of Applied Crystallography **11** (1978), no. 2, 102–113.

[LW11] J.-H. Lim, and J. Wiley, *Electrochemical Growth of Nanostructured Materials*, Three-Dimensional Nanoarchitectures (W. Zhou, and Z. L. Wang, eds.), Springer New York, 2011, 89–115 (English).

[LYZK09] C.-H. Lee, G.-C. Yi, Y. M. Zuev, and P. Kim, *Thermoelectric power measurements of wide band gap semiconducting nanowires*, Applied Physics Letters **94** (2009), 022106.

[MAU+08] J. Martin, N. Akerman, G. Ulbricht, T. Lohmann, J. H. Smet, K. von Klitzing, and A. Yacoby, *Observation of electron-hole puddles in graphene using a scanning single-electron transistor*, Nature Physics **4** (2008), 144–148.

[MCC+04] M. E. T. Molares, N. Chtanko, T. W. Cornelius, D. Dobrev, I. Enculescu, R. H. Blick, and R. Neumann, *Fabrication and contacting of single* Bi *nanowires*, Nanotechnology **15** (2004), no. 4, 201.

[MD71] N. F. Mott, and E. A. Davis (eds.), *Electronic Processes In Non-Crystalline Materials*, second ed., Oxford University Press, 1971.

[MDM+12] K. Malik, D. Das, D. Mondal, D. Chattopadhyay, A. K. Deb, S. Bandyopadhyay, and A. Banerjee, *Sb concentration dependent structural and resistive properties of polycrystalline* Bi – Sb *alloys*, Journal of Applied Physics **112** (2012), no. 8, 083706.

[MF95] H. Masuda, and K. Fukuda, *Ordered Metal Nanohole Arrays Made by a Two-Step Replication of Honeycomb Structures of Anodic Alumina*, Science **268** (1995), no. 5216, 1466–1468.

[MGPG+03] M. Martin-González, A. Prieto, R. Gronsky, T. Sands, and A. Stacy, *High-Density 40 nm Diameter* Sb – Rich $Bi_{2-x}Sb_xTe_3$ *Nanowire Arrays*, Advanced Materials **15** (2003), no. 12, 1003–1006.

[MGPK+03] M. Martin-González, A. L. Prieto, M. S. Knox, R. Gronsky, T. Sands, and A. M. Stacy, *Electrodeposition of* $Bi_{1-x}Sb_x$ *Films and 200-nm Wire Arrays from a Non-aqueous Solvent*, Chemistry of Materials **15** (2003), no. 8, 1676–1681.

[MI72] J. P. Michenaud, and J. P. Issi, *Electron and hole transport in bismuth*, Journal of Physics C: Solid State Physics **5** (1972), no. 21, 3061.

[MJC+05] G. Meng, Y. J. Jung, A. Cao, R. Vajtai, and P. M. Ajayan, *Controlled fabrication of hierarchically branched nanopores, nanotubes, and nanowires*, Proceedings of the National Academy of Sciences of the United States of America **102** (2005), no. 20, 7074–7078.

[MNH+09] M. Murata, D. Nakamura, Y. Hasegawa, T. Komine, T. Taguchi, S. Nakamura, V. Jovovic, and J. P. Heremans, *Thermoelectric properties of bismuth nanowires in a quartz template*, Applied Physics Letters **94** (2009), no. 19, 192104.

[MNH+10] M. Murata, D. Nakamura, Y. Hasegawa, T. Komine, D. Uematsu, S. Nakamura, and T. Taguchi, *Electrical Nanocontact Between Bismuth Nanowire Edges and Electrodes*, Journal of Electronic Materials **39** (2010), 1536–1542 (English).

[MPH90] D. T. Morelli, D. L. Partin, and J. Heremans, *Galvanomagnetic properties of single-crystal bismuth-antimony thin films*, Semiconductor Science and Technology **5** (1990), no. 3S, S257.

[MS70] A. F. Mayadas, and M. Shatzkes, *Electrical-Resistivity Model for Polycrystalline Films: the Case of Arbitrary Reflection at External Surfaces*, Phys. Rev. B **1** (1970), 1382–1389.

[MSP+10] N. Marcano, et al., *Weak-antilocalization signatures in the magnetotransport properties of individual electrodeposited Bi Nanowires*, Applied Physics Letters **96** (2010), no. 8, 082110.

[Mue12] S. Mueller, *Morphological, Structural, and Compositional Characterization of Electrodeposited* $Bi_{1-x}Sb_x$ *Nanowires*, Ph.D. thesis, Ruprecht-Karls-Universität Heidelberg, 2012.

[MvML62] S. Mase, S. von Molnar, and A. W. Lawson, *Galvanomagnetic Tensor of Bismuth at 20.4°K*, Phys. Rev. **127** (1962), 1030–1045.

[MYT+12] M. Murata, H. Yamamoto, F. Tsunemi, Y. Hasegawa, and T. Komine, *Four-Wire Resistance Measurements of a Bismuth Nanowire Encased in a Quartz Template Utilizing Focused Ion Beam Processing*, Journal of Electronic Materials **41** (2012), 1442–1449 (English).

[NBKB11] K. Nielsch, J. Bachmann, J. Kimling, and H. Böttner, *Thermoelectric Nanostructures: From Physical Model Systems towards Nanograined Composites*, Advanced Energy Materials **1** (2011), no. 5, 713–731.

[NCS+02] K. Nielsch, J. Choi, K. Schwirn, R. B. Wehrspohn, and U. Gösele, *Self-ordering Regimes of Porous Alumina: The 10 Porosity Rule*, Nano Letters **2** (2002), no. 7, 677–680.

[NKH+12] A. Nikolaeva, L. Konopko, T. Huber, P. Bodiul, I. Popov, and E. Moloshnik, *Size-Quantization Semimetal-Semiconductor Transition in* $Bi_{0.98}Sb_{0.02}$ *Nanowires: Thermoelectric Properties*, Journal of Electronic Materials **41** (2012), 2313–2316 (English).

[NMH+10] D. Nakamura, M. Murata, Y. Hasegawa, T. Komine, D. Uematsu, S. Nakamura, and T. Taguchi, *Thermoelectric Properties of a 593-nm Individual Bismuth Nanowire Prepared Using a Quartz Template*, Journal of Electronic Materials **39** (2010), 1960–1965, 10.1007/s11664-009-1045-3.

[OBP+02] B. Ohlsson, M. Björk, A. Persson, C. Thelander, L. Wallenberg, M. Magnusson, K. Deppert, and L. Samuelson, *Growth and characterization of GaAs and InAs nano-whiskers and InAs/GaAs heterostructures*, Physica E: Low-dimensional Systems and Nanostructures **13** (2002), no. 2-4, 1126 – 1130.

[OZD+12] Y. Okada, W. Zhou, C. Dhital, D. Walkup, Y. Ran, Z. Wang, S. D. Wilson, and V. Madhavan, *Visualizing Landau Levels of Dirac Electrons in a One-Dimensional Potential*, Phys. Rev. Lett. **109** (2012), 166407.

[PBBMD08] L. Peraldo Bicelli, B. Bozzini, C. Mele, and L. D'Urzo, *A Review of Nanostructural Aspects of Metal Electrodeposition*, Int. J. Electrochem. Sci. **3** (2008), 356–408.

[Pen02] R. M. Penner, *Mesoscopic Metal Particles and Wires by Electrodeposition*, The Journal of Physical Chemistry B **106** (2002), no. 13, 3339–3353.

[PLT+12] N. Peranio, E. Leister, W. Töllner, O. Eibl, and K. Nielsch, *Stoichiometry Controlled, Single-Crystalline* Bi_2Te_3 *Nanowires for Transport in the Basal Plane*, Advanced Functional Materials **22** (2012), no. 1, 151–156.

[PM06] M. Paunovic, and S. Mordechay, *Fundamentals of Electrochemical Deposition*, second edition ed., Wiley & Sons, 2006.

[PMGK+03] A. L. Prieto, M. Martin-González, J. Keyani, R. Gronsky, T. Sands, and A. M. Stacy, *The Electrodeposition of High-Density, Ordered Arrays of* $Bi_{1-x}Sb_x$ *Nanowires*, Journal of the American Chemical Society **125** (2003), no. 9, 2388–2389.

[RHL+12] T. Rieger, S. Heiderich, S. Lenk, M. I. Lepsa, and D. Grützmacher, *Ga-assisted MBE growth of GaAs nanowires using thin HSQ layer*, Journal of Crystal Growth **353** (2012), no. 1, 39 – 46.

[RLD01] O. Rabina, Y.-M. Lin, and M. S. Dresselhaus, *Anomalously high thermoelectric figure of merit in* $Bi_{1-x}Sb_x$ *nanowires by carrier pocket alignment*, Applied Physics Letters **79** (2001), 81–84.

[Row94] D. M. Rowe, *CRC Handbook of Thermoelectrics*, CRC Press LLC, 1994.

[RSNCB11] K.-G. Reinsberg, C. Schumacher, K. Nielsch, and J. A. Clement Broekaert, *Precision improvements by the use of principal component regression and pooled regression applied to main component determinations with ICP-OES for thermoelectric films*, J. Anal. At. Spectrom. **26** (2011), 2477–2482.

[SBZJ10] G. D. Sulka, A. Brózka, L. Zaraska, and M. Jaskula, *Through-hole membranes of nanoporous alumina formed by anodizing in oxalic acid and their applications in fabrication of nanowire arrays*, Electrochimica Acta **55** (2010), no. 14, 4368 – 4376.

[Sch12] C. Schumacher, *Pulsed Electrodeposited p- and n-Doped Chalcogenide Semiconductors for Thermoelectric Applications: From Films to Nanowires*, Ph.D. thesis, University Hamburg, 2012.

[SF31] A. Sommerfeld, and N. H. Frank, *The Statistical theory of thermoelectric, galvano- and thermomagnetic phenomena in metals*, Rev. Mod. Phys. **3** (1931), 1–42.

[SHFM02] R. Solanki, J. Huo, J. Freeouf, and B. Miner, *Atomic layer deposition of ZnSe/CdSe superlattice nanowires*, Applied Physics Letters **81** (2002), no. 20, 3864–3866.

[SHKL09] W. Shim, J. Ham, J. Kim, and W. Lee, *Shubnikov–de* Haas *oscillations in an individual single-crystalline bismuth nanowire grown by on-film formation of nanowires*, Applied Physics Letters **95** (2009), no. 23, 232107.

[SHL+09] W. Shim, J. Ham, K.-i. Lee, W. Y. Jeung, M. Johnson, and W. Lee, *On-Film Formation of Bi Nanowires with Extraordinary Electron Mobility*, Nano Letters **9** (2009), no. 1, 18–22.

[SKiL+08] W. Shim, et al., *Magnetotransport properties of an individual single-crystalline Bi nanowire grown by a stress induced method*, Journal of Applied Physics **104** (2008), no. 7, 073715.

[Smi78] R. A. Smith, *Semiconductors*, Cambridge University Press, 1978.

[SRA+12] C. Schumacher, et al., *Optimization of Electrodeposited p-Doped* Sb_2Te_3 *Thermoelectric Films by Millisecond Potentiostatic Pulses*, Advanced Energy Materials **2** (2012), 345–352.

[SSM+02] G. D. Sulka, S. Stroobants, V. Moshchalkov, G. Borghs, and J.-P. Celis, *Synthesis of Well-Ordered Nanopores by Anodizing Aluminum Foils in Sulfuric Acid*, Journal of The Electrochemical Society **149** (2002), no. 7, 97–103.

[Sul08] G. D. Sulka, *Highly Ordered Anodic Porous Alumina Formation by Self-Organized Anodizing*, Wiley-VCH Verlag GmbH & Co. KGaA, 2008.

[SW62] G. E. Smith, and R. Wolfe, *Thermoelectric Properties of Bismuth-Antimony Alloys*, Journal of Applied Physics **33** (1962), no. 3, 841–846.

[SWB+07] E. Sandnes, M. Williams, U. Bertocci, M. Vaudin, and G. Stafford, *Electrodeposition of bismuth from nitric acid electrolyte*, Electrochimica Acta **52** (2007), no. 21, 6221 – 6228.

[SYMC+ 2] X. L. Sun, M. Yu-Ming, S. B. Cronin, M. S. Dresselhaus, J. Y. Ying, and G. Chen (eds.), *Theoretical modeling of thermoelectricity in Bi nanowires*, 29 1999-Sept. 2.

[TB06] R. A. Tolutis, and S. Balevicius, *Study of large magnetoresistance of thin polycrystalline Bi films annealed at critical temperatures*, physica status solidi (a) **203** (2006), no. 3, 600–607.

[TGG+12] Y. Tian, C. F. Guo, S. Guo, Y. Wang, J. Miao, Q. Wang, and Q. Liu, *Bismuth nanowire growth under low deposition rate and its ohmic contact free of interface damage*, AIP Advances **2** (2012), no. 1, 012112.

[TKCM08] M. Tian, N. Kumar, M. H. W. Chan, and T. E. Mallouk, *Evidence of local superconductivity in granular* Bi *nanowires fabricated by electrodeposition*, Phys. Rev. B **78** (2008), no. 4, 045417.

[TKY+08] T. Teramoto, T. Komine, S. Yamamoto, M. Kuraishi, R. Sugita, Y. Hasegawa, and H. Nakamura, *Influence of the band structure of* BiSb *alloy on the magneto-Seebeck coefficient*, Journal of Applied Physics **104** (2008), no. 5, 053714.

[TMB+04] Y. Tian, G. Meng, S. K. Biswas, P. M. Ajayan, S. Sun, and L. Zhang, *Y-branched* Bi *nanowires with metal–semiconductor junction behavior*, Applied Physics Letters **85** (2004), no. 6, 967–969.

[Tre81] J. U. Trefny, *Bi-Sb thin films for thermoelectric energy conversion*, Proc. Intersoc. Energy Convers. Eng. Conf., (United States), Journal Volume: 2, conference: IECEC conference, Atlanta, GA, USA, Colo Sch of Mnes, Golden, 1981, 2019–2012.

[TWK+06] M. Tian, J. Wang, N. Kumar, T. Han, Y. Kobayashi, Y. Liu, T. E. Mallouk, and M. H. W. Chan, *Observation of Superconductivity in Granular* Bi *Nanowires Fabricated by Electrodeposition*, Nano Letters **6** (2006), no. 12, 2773–2780, PMID: 17163704.

[VRSS03] P. M. Vereecken, S. Ren, L. Sun, and P. C. Searson, *Electrodeposition of* $Bi_{1-x}Sb_x$ *Thin Films*, Journal of The Electrochemical Society **150** (2003), no. 3, C131–C139.

[VSCO01] R. Venkatasubramanian, E. Siivola, T. Colpitts, and B. O'Quinn, *Thin-film thermoelectric devices with high room-temperature figures of merit*, Nature **413** (2001), no. 6856, 597–602.

[VSS+00] P. M. Vereecken, L. Sun, P. C. Searson, M. Tanase, D. H. Reich, and C. L. Chien, *Magnetotransport properties of bismuth films on p-GaAs*, Journal of Applied Physics **88** (2000), no. 11, 6529–6535.

[WKBL99] M. Wagener, R. Kroon, J. Botha, and A. Leitch, *Analysis of secondary phases in InSbBi thin films*, Physica B: Condensed Matter **273-274** (1999), no. 0, 919 – 922.

[WMF+02] E. C. Walter, B. J. Murray, F. Favier, G. Kaltenpoth, M. Grunze, and R. M. Penner, *Noble and Coinage Metal Nanowires by Electrochemical Step Edge Decoration*, The Journal of Physical Chemistry B **106** (2002), no. 44, 11407–11411.

[WZJZ+01] X. F. Wang, L. D. Zhang, H. Z. S. J Zhang, X. S. Peng, J. F. M J Zheng, J. L. Chen, and B. J. Gao, *Ordered single-crystalline* Bi *nanowire arrays embedded in nanochannels of anodic alumina membranes*, Journal of Physics D: Applied Physics **34** (2001), no. 3, 418 – 421.

[WZS+01] X. F. Wang, J. Zhang, H. Z. Shi, Y. W. Wang, G. W. Meng, X. S. Peng, L. D. Zhang, and J. Fang, *Fabrication and temperature dependence of the resistance of single-crystalline* Bi *nanowires*, Journal of Applied Physics **89** (2001), no. 7, 3847–3851.

[XFW+05] F. H. Xue, G. T. Fei, B. Wu, P. Cui, and L. D. Zhang, *Direct Electrodeposition of Highly Dense* Bi/Sb *Superlattice Nanowire Arrays*, Journal of the American Chemical Society **127** (2005), no. 44, 15348–15349.

[XHY+08] F. Xiao, C. Hangarter, B. Yoo, Y. Rheem, K.-H. Lee, and N. V. Myung, *Recent progress in electrodeposition of thermoelectric thin films and nanostructures*, Electrochimica Acta **53** (2008), no. 28, 8103 – 8117.

[YA72] W. Yim, and A. Amith, BiSb *alloys for magneto-thermoelectric and thermomagnetic cooling*, Solid-State Electronics **15** (1972), no. 10, 1141 – 1165.

[YHSX04] J. H. Yuan, F. Y. He, D. C. Sun, and X. H. Xia, *A Simple Method for Preparation of Through-Hole Porous Anodic Alumina Membrane*, Chemistry of Materials **16** (2004), no. 10, 1841–1844.

[YLCS99] F. Y. Yang, K. Liu, C. L. Chien, and P. C. Searson, *Large Magnetoresistance and Finite-Size Effects in Electrodeposited Single-Crystal Bi Thin Films*, Phys. Rev. Lett. **82** (1999), 3328–3331.

[YLH+99] F. Y. Yang, K. Liu, K. Hong, D. H. Reich, P. C. Searson, and C. L. Chien, *Large Magnetoresistance of Electrodeposited Single-Crystal Bismuth Thin Films*, Science **284** (1999), no. 5418, 1335–1337.

[YT02] O. Yamashita, and S. Tomiyoshi, *Effect of geometrical shape on magneto–Peltier and Ettingshausen cooling in* Bi *and* $Bi_{0.88}Sb_{0.12}$ *polycrystals*, Journal of Applied Physics **92** (2002), no. 7, 3794–3802.

[YXB+07] B. Yoo, F. Xiao, K. N. Bozhilov, J. Herman, M. A. Ryan, and N. V. Myung, *Electrodeposition of Thermoelectric Superlattice Nanowires*, Advanced Materials **19** (2007), no. 2, 296–299.

[YZL+08] Z. Ye, H. Zhang, H. Liu, W. Wu, and Z. Luo, *Observation of superconductivity in single crystalline* Bi *nanowires*, Nanotechnology **19** (2008), no. 8, 085709.

[Zas10] S. Zastrow, *Aufbau einer Hochtemperature-Messanlage zur Charakterisierung der elektronischen Transporteigenschaften von thermoelektrischem Material auf Basis von Indium-gefüllten Kobalt-Antimon-Skutteruditen*, Master's thesis, Universität Hamburg - Fachbereich Physik, 2010.

[ZBBK00] V. Zemskov, A. Belaya, U. Beluy, and G. Kozhemyakin, *Growth and investigation of thermoelectric properties of* Bi – Sb *alloy single crystals*, Journal of Crystal Growth **212** (2000), no. 1, 161–166.

[ZBG+09] Y. Zhang, W. V. Brar, C. Girit, A. Zettl, and M. F. Crommie, *Origin of spatial charge inhomogeneity in graphene*, Nature Physics **5** (2009), 722,726.

[ZGB+13] S. Zastrow, J. Gooth, T. Boehnert, S. Heiderich, W. Toellner, S. Heimann, S. Schulz, and K. Nielsch, *Thermoelectric transport and Hall measurements of low defect* Sb_2Te_e *thin films grown by atomic layer deposition*, Semiconductor Science and Technology **28** (2013), no. 3, 035010.

[ZLPZ07] F. Zhang, X. Liu, C. Pan, and J. Zhu, *Nano-porous anodic aluminium oxide membranes with* 6 – 19 *nm pore diameters formed by a low-potential anodizing process*, Nanotechnology **18** (2007), no. 34, 345302.

[Zos07] C. G. Zoski, *Handbook of Electrochemistry*, Elsevier Science, 2007.

Acknowledgments

Here I would like to thank all the people that have been direct or indirect involved to make this work happen. My thanks go to Prof. Dr. K. Nielsch for welcoming me in his work group and for giving me the opportunity to work on this wide field of reach. My thanks go also to Prof. Dr. A. Fontcuberta i Morralis for the review of this thesis. Additionally I thank Prof. Dr. U. Merkt for his constant interest on my work during the last years and of course the DFG for funding via the Graduate class 1286.
For support during measurements I would like to thank Sebastian Zastrow, Tim Böhnert and Johannes Gooth. Thanks go to Robert Zierold for ALD depositions and William Töllner for a good time at the TEM. Furthermore Boris Landgraf, Christian Schumacher and Sebastian Zastrow for XRD analysis and Jan Gluschke for many hours at the laser writer. I thank Reinhold Meissner and Lewis Akinsinde for technical support. Additional thanks go to Stephan Martens for the help with the sputter machine. Furthermore I thank all members from Group K and the Graduate Class 1286 for a good time in and out of the office and for fruitful discussions. And thanks to all other groups for a good atmosphere at the institute.
Personal thanks go to all people who took the time to proofread this thesis and for support during the last weeks.
I thank my parents for their constant faith and support and for encouraging me when I had doubts. The same holds true for my brother and my sister who are just the best brother and sister I could wish for.

Ehrenwörtliche Erklärung

Hiermit versichere ich ausdrücklich, dass ich die vorliegende schriftliche Ausarbeitung selbständig verfasst und – einschließlich beigefügter Abbildungen, Skizzen und Diagramme – keine anderen als die im Literaturverzeichnis angegebenen Quellen, Darstellungen und Hilfsmittel benutzt habe. Diese Arbeit lag noch keiner anderen Person oder Prüfungsbehörde im Rahmen eines Promotionsverfahrens vor.

Sonja Heiderich – Hamburg, 08. April, 2013